NAVAL POSTGRADUATE SCHOOL
Monterey, California

THESIS

THE EFFECT OF COLD WORK ON MARTENSITIC TRANSFORMATIONS IN CU-ZN-AL SHAPE MEMORY ALLOYS

by

Stephen Mark Sullivan

December 1983

Thesis Advisor: J. Perkins

SECURITY CLASSIFICATION OF THIS PAGE (When Data Entered)

REPORT DOCUMENTATION PAGE

READ INSTRUCTIONS BEFORE COMPLETING FORM

1. REPORT NUMBER	2. GOVT ACCESSION NO. / 3. RECIPIENT'S CATALOG NUMBER
4. TITLE (and Subtitle): The Effect of Cold Work on Martensitic Transformations in Cu-Zn-Al Shape Memory Alloys	5. TYPE OF REPORT & PERIOD COVERED: Master's Thesis, December 1983 / 6. PERFORMING ORG. REPORT NUMBER
7. AUTHOR(s): Stephen Mark Sullivan	8. CONTRACT OR GRANT NUMBER(s)
9. PERFORMING ORGANIZATION NAME AND ADDRESS: Naval Postgraduate School, Monterey, California 93943	10. PROGRAM ELEMENT, PROJECT, TASK AREA & WORK UNIT NUMBERS
11. CONTROLLING OFFICE NAME AND ADDRESS: Naval Postgraduate School, Monterey, California 93943	12. REPORT DATE: December 1983 / 13. NUMBER OF PAGES: 126
14. MONITORING AGENCY NAME & ADDRESS(if different from Controlling Office)	15. SECURITY CLASS. (of this report) / 15a. DECLASSIFICATION/DOWNGRADING SCHEDULE

16. DISTRIBUTION STATEMENT (of this Report)

Approved for public release, distribution unlimited

17. DISTRIBUTION STATEMENT (of the abstract entered in Block 20, if different from Report)

18. SUPPLEMENTARY NOTES

19. KEY WORDS (Continue on reverse side if necessary and identify by block number)

Shape Memory Effect
Martensitic Transformation
Copper Base Alloys
Cu-Zn-Al
Cold Work

20. ABSTRACT (Continue on reverse side if necessary and identify by block number)

Samples of martensitic Cu-Zn-Al shape memory alloy were deformed by cold rolling below M_f (martensite finish temperature). The effect of cold work upon the reaction kinetics of parent to product and product to parent transformations was studied utilizing differential scanning calorimetry methods. Characterization of the microstructure of selectively deformed shape memory alloy samples was

DD FORM 1 JAN 73 1473 EDITION OF 1 NOV 65 IS OBSOLETE

S/N 0102-LF-014-6601

SECURITY CLASSIFICATION OF THIS PAGE (When Data Entered)

Block 20 Cont'd:

accomplished by optical and transmission electron microscopy techniques. Correlation of microstructure and substructural conditions with associated transformation trends provided an understanding of the effect of cold work, as characterized by stress induced morphology, upon shape memory behavior.

Approved for public release, distribution unlimited

The effect of Cold Work on Martensitic Transformations in Cu-Zn-Al Shape Memory Alloys

by

Stephen Mark Sullivan
Lieutenant, United States Navy
B.A., Vanderbilt University, 1976

Submitted in partial fulfillment of the
requirements for the degree of

MASTER OF SCIENCE IN ENGINEERING SCIENCE

from the

NAVAL POSTGRADUATE SCHOOL
December 1983

ABSTRACT

Sampled of martensitic Cu-Zn-Al shape memory alloy were deformed by cold rolling below M_f (martensite finish temperature). The effect of cold work upon the reaction kinetics of parent to product and product to parent transformations was studied utilizing differential scanning calorimetry methods. Characterization of the microstructure of selectively deformed shape memory alloy samples was accomplished by optical and transmission electron microscopy techniques. Correlation of microstructure and substructural conditions with associated transformation trends provided an understanding of the effect of cold work, as characterized by stress induced morphology, upon shape memory behavior.

TABLE OF CONTENTS

LIST OF FIGURES

LIST OF TABLES

LIST OF MICROGRAPHS

ACKNOWLEDGEMENT

This research was sponsored by the National Science Foundation research program: "Martensitic Transformations in Shape Memory Alloys".

Thanks are due to Professor Jeff Perkins, who first introduced me to the field of Material Science and provided initial program formulation and continued guidance, and to Tom Kellogg, for his technical assistance. I would also like to thank Dr. Kenji Adachi for his generous assistance in optical microscopy, TEM, and interpretation of experimental data. Finally, I want to thank my wife, Judy and children, Christopher, Mark, Ashley, and Keith, without whose support and patience this research endeavor could never have reached fruition.

I. INTRODUCTION

The shape memory effect (SME), the curious metallurigical phenomenon associated with the ability of certain alloys to recover an undeformed shape after what would appear to be permanent deformation (due to the magnitude of strains involved), has become a topic of increasing interest and importance. These so called shape memory alloys have a variety of potential applications due to their unique thermo-mechanical properties. The utilization of shape memory alloys for marine applications requiring materials of high specific damping capacity for noise and vibration abatement has been investigated by Kelly [Ref. 1]. Another obvious engineering application of the shape memory effect is in the area of thermally activated controls. Electrically actuated springs manufactured from Ni-Ti shape memory alloys are currently marketed by the automobile industry. Orifice jets, thermally operated switches and relays, thermostatic valves and control valves exploiting shape memory properties are currently under development [Ref. 2]. The intense research directed toward understanding the shape memory effect and in particular the morphology and kinetics of displacive, diffusionless martensitic transformations as evidenced by the plethora of literature published in this area attests to the enormous economic and engineering

potential inherent in the proper understanding, development and utilization of these alloys.

In 1951, Chang and Read [Ref. 3], working with Au-Cd alloys, reported the general pattern of alloy behavior popularly identified as shape memory. Since 1951, shape memory behavior has been reported to occur in many binary and ternary systems including: Ni-Ti (Nitinol), Fe-Pt, Mn-Cu, In-Tl, Cu-Zn, Cu-Zn-Sn, Cu-Ni-Al and Cu-Zn-Al [Refs. 4-11]. The ternary Cu-Zn-Al system is the subject of this investigation.

Investigators have used the nomenclature shape memory effect to describe several different kinds of alloy behavior. To avoid confusion, a brief review of terminology follows [Refs. 12-14]. Shape memory (SM), also known as strain memory or "marmem" (martensite memory) is the descriptive terminology used when refering to various metallurgical phenomenea associated with several alloy systems in which there is a reversal of apparent plastic strain. When an alloy specimen is deformed in the martensite state (below M_f) and recovers its original undeformed shape upon heating, this behavior is ascribed the title, shape memory effect (SME). The pseudoelastic effect (PE) is the generic description associated with a specimens ability to recover induced strain upon unloading. The proportion of SME or PE contributing to the overall shape memory behavior of a particular alloy system is a function of both the

magnitude of the induced strain and the temperature regime in which the deformation was performed. Finally, the terminology stress induced martensite (SIM), refers to martensite which has been produced at temperatures above M_s by deformation of the parent phase.

Wayman, Shimizu et al. [Refs. 13;14:p.2719;15] have suggested the following prerequisites for shape memory behavior: 1.) thermoelastic martensitic transformation, 2.) ordering of parent (and consequently martensitic) phases, and 3.) internally twinned martensites. Notable exceptions to the above criteria occur in ternary Cu-Zn-X systems in which the martensites may be internally faulted rather than internally twinned and in the In-Tl systems which undergo thermoelastic martensitic transformation but whose solid solutions may be regarded as disordered in the conventional sense.

The SME is a consequence of thermoelastic martensitic transformations in which the elastic energy accompanying the development of martensites competes with the free energy of the transformation process. The transformation from parent to martensite (P$\rightarrow$M) can be accomplished by decreasing temperature or by application of stress (SIM). As temperature decreases or stress increases, martensites are nucleated at pre-existing defects in the parent phase and grow continuously. The reverse transformation from martensite to parent (M$\rightarrow$P) phase is accomodated by

increasing the temperature to above A_s or relaxing the induced stress for SIM. The parent phase reforms along the exact crystallographic routes by which the original martensites were produced. This transformation occurs by shrinkage of the existing martensites to reform the parent phase [Refs. 11:p.33;13:p.535].

Many ternary Cu-Zn-Al alloys (so called beta phase alloys) exhibit shape memory behavior. These beta phase alloys transform martensitically into a close packed layered structure having a long-period stacking order based on prior close packed {110} planes of the parent phase. The product phase stacking sequence depends upon the specific alloy system, the degree and type of ordering inherited from the parent phase, and the stress conditions existing in the original parent phase. The reaction of importance being:

$$BCC(B2,\ DO_3) \longrightarrow 3R,\ 9R,\ 18R$$

where the product (beta prime) phase is a 3R, 9R or 18R variant with ABC, ABCBCACAB or ABCBCACABABCBCACAB stacking sequence [Ref. 16].

Wayman et al. [Refs. 17-19] have shown that deformation below M_f of beta prime phase ternary Cu-Zn-Al alloys results in preferential growth of certain martensite variants at the expense of others. Surface relief photomicrographs of deformed beta prime alloys exhibit parallel bands (plates)

of pink appearence corresponding to the product of stress induced martensite to martensite transformations.

The purpose of this investigation is to study the effects of cold work upon the martensite to parent and parent to martensite transformation kinetics of polycrystalline Cu-Zn-Al alloy specimens. Emphasis was placed upon documenting structural and substructural characteristics of cold worked martensitic specimens which might account for differences in the reaction kinetics between alloy specimens with varying degrees of cold work.

II. EXPERIMENTAL PROCEDURES

A. SAMPLE PREPARATION

The Cu-Zn-Al alloy selected for study was provided by Delta Research Limited, Ipswitch, Suffolk, England. Alloy designator B was used exclusively in this research. Selection was based upon the alloys' reputed martensite start temperature (333 K). Therefore, alloy B was expected to exist as martensite at room temperature. The nominal composition of the alloy is (76.0 wt.% Cu, 16.5 wt.% Zn, and 7.5 wt.% Al). The as received alloy, originally in the form of a 1 cm diameter hot rolled bar was cut into bars 8.0 mm X 8.0 mm X 30.0 mm. These bulk samples were cleaned in dilute nitric acid so as to minimize the amount of grease present. Five bulk samples of the as received alloy B were placed in an evacuated dessicator until required for subsequent use. The remaining bars were then sealed in evacuated quartz tubes and annealed at 1123 K for twenty minutes. The annealing was performed to homogenize and eliminate second phase. The solution temperature was determined from phase diagrams in [Ref. 20]. Quenching was accomplished by shattering the quartz tubes in iced brine. The samples were quenched immediately upon removal from the furnace. The annealed and quenched bulk samples were again cleaned and placed in an evacuated dessicator until required for subsequent use.

B. COLD WORKING

Cold worked specimens of the martensitic alloy were preapared to study the effects of stress induced micro-structural changes upon the kinetic properties of the martensite to parent and parent to martensite phase transformations. The as received and as homogenized bulk samples (8.0 mm X 8.0 mm X 30.0 mm bars) were cold rolled at NPS with the Fenn laboratory rolling mill (5 HP and 10.5 cm diameter rollers). Each bulk sample was repeatedly flop-rolled at room temperature in the mill decreasing the roller bite increment approximently 0.03 mm after each flop-roll. The average percent of cold work $\overline{H}$ was defined as:

$$\overline{H} = \frac{H_o - H_f}{H_o} \times 100\%$$

where H_o was the original height of the bar before rolling and H_f is the final height of the bar after repeated flop-rolling [Ref. 21]. The maximum deformation attempted was 13.0%. This deformation limit was imposed because experiments conducted by Kelly [Ref. 1] and Wayman [Ref. 17] demonstrated that cold working martensitic Cu-Zn-Al alloys beyond approximately 13.0% resulted in excessive cracking of the sample material.

C. OPTICAL MICROSCOPY

All bulk cross section metallographic specimens for optical microscopy were prepared identically. Sections were cut transverse to the longitudinal axis of the bulk samples. For cold worked specimens, the sections were cut transverse to the rolling direction and away from the ends of the bars to avoid anomalies due to end effects. Each specimen was cold mounted, polished, and etched. The procedure follows:

1. Sand on 180 grit emery paper
2. Sand on 240 grit emery paper
3. Sand on 320 grit emery paper
4. Sand on 400 grit emery paper
5. Sand on 600 grit emery paper
6. Polish on 600 grit alumina wheel
7. Polish on 1.0 micron gamma alumina wheel
8. Polish on 0.05 micron alpha alumina wheel
9. Etch for eight seconds with (5g.$FeCl_3$, 2 ml HCl, and 100 ml ethanol) solution.

All DSC specimens for optical microscopy were polished identically. Each disc was jet polished using Struers Tenupol 2 apparatus (1:1 ortho-phosphoric acid/H_2O solution, pump spped 6.5, rectifier voltage < 20.0 V, rectifier amperage < 0.35 A, and 240 K).

Photomicrographs were taken with Polaroid type 55 film and Kodak technical pan film 2415 using a Zeiss Photomicroscope.

The mean linear intercept method was used to assess specimen grain size [Ref. 22]. The mean linear intercept $\bar{L}$ is a measure of average grain chord length and is given by:

$$\bar{L} = \frac{\sum_{i=1}^{n} L_i}{n \sum_{i=1}^{n} (N_i - 1)}$$

where L_i is a random test line segment length and N_i is the number of grain boundry intercepts of the test line segment. Grain size was determined for all metallographic specimens prepared for optical microscopy.

D. DIFFERENTIAL SCANNING CALORIMETRY

Characterization of the thermal properties of the martensite to parent and parent to martensite transformations of alloy B was accomplished by differential scanning calorimetry. The Perkin-Elmer (DSC-2) Differential Scanning Calorimeter (DSC) was utilized for this purpose. The DSC measures the change in power required to maintain a sample and holder at the same temperature as a reference holder. The transformation from parent to martensite is exothermic while the transformation from martensite to parent is endothermic. Thus a transition in phase produces a departure from baseline on a strip chart recorder. The chart presentation of thermal data is consistent with conventional practice. Endothermic transitions are represented by downscale departures from the ordinate baseline and exothermic

transitions are represented by upscale departures from the ordinate baseline. The ordinate is calibrated in millicalories per second and the abscissa is degrees Kelvin [Ref. 23].

All the specimens for DSC analysis were prepared identically. Sections were cut transverse to the longitudinal axis of the bulk samples. For cold worked specimens, the sections were cut transverse to the rolling direction and away from the ends of the bars. Three small discs of the alloy 3.0 mm in diameter and approximately 0.13 mm thick were cut from each initial section. Each disc was electropolished in 10% KCN solution (18 VAC) at room temperature and weighed on a Sartorius Balance. The discs were stored in an evacuated dessicator until thermal cycling was accomplished.

For alloy B, the DSC was programed to cycle between 280 K and 430 K, assuring that start and finish temperatures would be unaffected by transients experienced at the limits of the DSC programed temperature range. A slow heating/cooling rate of 10 K per minute was chosen to insure complete transformation during thermal cycling. Each disc was given three complete thermal cycles. A complete thermal cycle is defined as a temperature excursion from below A_s to above A_f and then in the reverse direction from above M_s to below M_f.

The kinetic parameters measured for alloy B were:

Martensite Start Temperature	M_s
Martensite Finish Temperature	M_f
Martensite Peak Temperature	M_{max}
Parent to Martensite Peak Width	M_{width}
Parent to Martensite Peak Height	M_{height}
Parent to Martensite Peak Area	M_{area}
Parent Start Temperature	A_s
Parent Finish Temperature	A_f
Parent Peak Temperature	A_{max}
Martensite to Parent Peak Width	A_{width}
Martensite to Parent Peak Height	A_{height}
Martensite to Parent Peak Area	A_{area}.

M_{max} and A_{max} are defined as the peak temperatures, determined as the temperatures where the maximum transformation rate occured (maximum displacement on the ordinate from the alloy's pretransformation baseline). M_{height} and A_{height} are defined as the peak heights and correspond to the ordinate displacement of the generated curves at M_{max} and A_{max} respectively. M_{width} and A_{width} are defined as the peak widths of the transofmrations, determined as the width of the generated transformation curves measured at one half peak height. M_s, M_f, A_s, and A_f are defined as the start and finish temperatures for the parent to martensite ($P \rightarrow M$) and martensite to parent ($M \rightarrow P$) phase transformations. These values were determined by constructing a near tangent

line to points on the pretransformation and posttransformation baselines of the generated curves. The temperatures at which the generated curves departed from the constructed tangent lines by five percent of the maximum peak heights were recorded as the start and finish temperatures of the transformations. M_{area} and A_{area} are defined as the area under the generated curves for the P→M and M→P phase transformations. These areas correspond to the energy of transformation for the processes and were determined using Simpson's Rule approximation technique. Figure 1 is a schematic illustration of DSC profiles for the transformation process.

E. TRANSMISSION ELECTRON MICROSCOPY

Identification of microstructural features in cold worked samples of alloy B which may contribute to differences in the kinetic properties of the M→P and P→M phase transformations was accomplished by examination of transmission electron photomicrographs taken of alloy samples prior to and after thermal cycling. Using the South Bay Technology, Inc. low speed diamond wheel saw and Buehler Ltd. high concentration diamond wheel, thin foils were cut transverse to the longitudinal axis of the bulk samples. For cold worked specimens, foils were cut transverse to the rolling direction and away from the ends of the bars. Small discs of the alloy 3.0 mm in diameter and approximently 0.13 mm

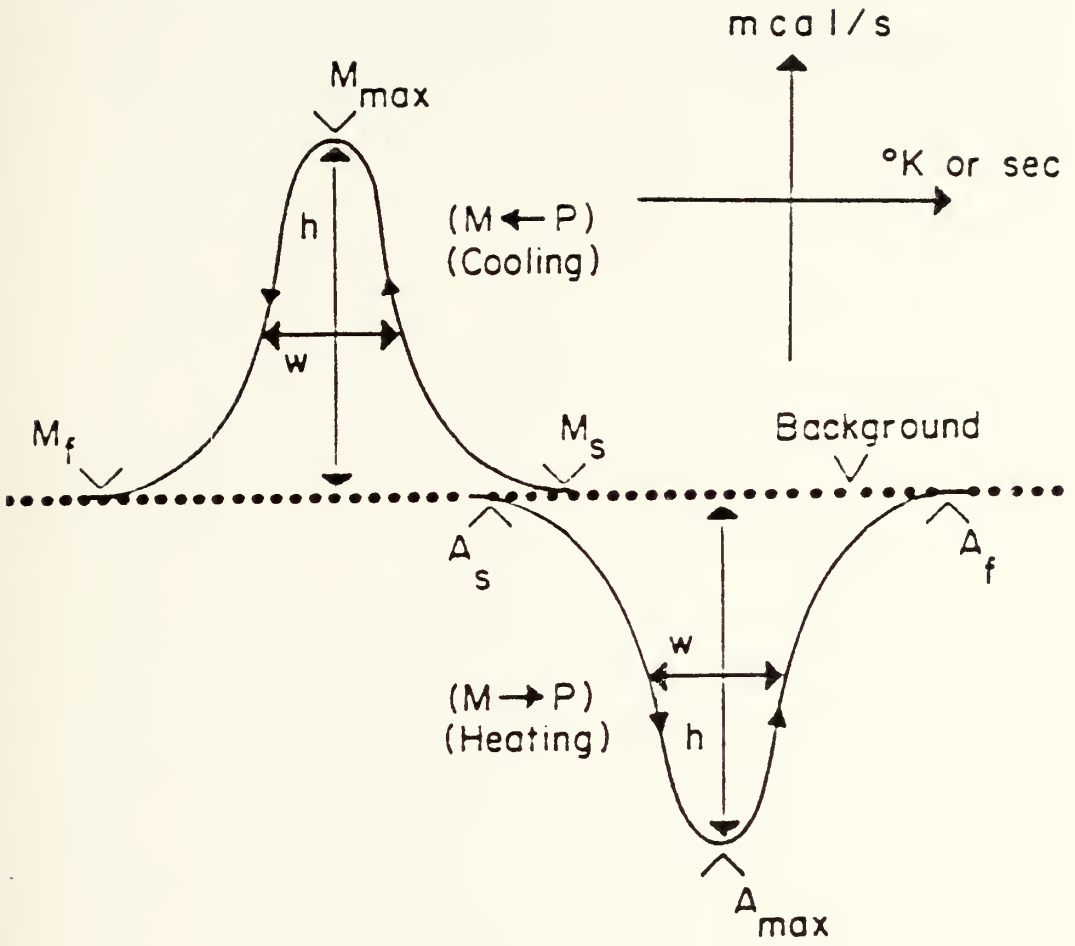

Figure 1. Schematic drawing of DSC M → P and P → M transformation profiles illustrating the transformation temperatures (M_s, M_f, M_{max}, A_s, A_f and A_{max}) and the peak height and peak width.

thick were cut from the foils. Each disc was jet polished using Struers Tenupol 2 apparatus (1:1 orthophosphoric acid/H_2O solution, pump speed 6.5, rectifier voltage < 20.0 V, rectifier amperage < 0.35 A, and 240 K). Transmission photomicrographs were taken with the Japan Electronics Lab Co., Ltd. Transmission Electron Microscope, Model JEM-100 CX, equipped with a side entry Goniometer and operated at an accelerating voltage of 120 kV using Kodak electron microscope film 4489.

III. RESULTS

A. COLD WORKING

Cold working the as received and annealed and quenched bulk samples (8.0 mm X 8.0 mm X 30.0 mm bars) to achieve a specific amount of deformation proved to be a difficult task. Initially, as the roller bite increment was decreased from original bar section thickness, the martensitic bulk samples apparently deformed elastically, returning to the original unrolled bar dimensions as measured by micrometer after rolling. As the bite increment was further decreased and the samples were repeatedly flop-rolled, the bars continued to respond elastically until the roller bite was approximately 1% less than original bar thickness. At this point, the samples suddenly deformed to the dimension of the roller bite and further reduction in bite increment produced corresponding sample deformation. The controls for adjusting the bite increment on the Fenn rolling mill were appreciably inaccurate, so that measurement of the roller bite by caliper was necessary to achieve desired results. Also, mechanically polishing the sample surfaces prior to rolling facilitated uniform deformation along the length of the bars. As expected, cold work in excess of approximately 12.5% resulted in unacceptable cracking of the sample.

Table I summarizes the heat treatment, percent cold work and corresponding average grain size of bulk samples

TABLE I

Sample identification and grain size.

Sample Number	Sample Preparation: Heat Treatment	Sample Preparation: Cold Work (%)	Grain Size (μm)
1	As Received	0.00	400
2	As Received	1.09	402
3	As Received	2.57	401
4	As Received	4.20	400
5	As Received	12.30	401
6	Annealed & Quenched	0.00	938
7	Annealed & Quenched	4.20	940
8	Annealed & Quenched	7.15	936
9	Annealed & Quenched	10.36	939

prepared for subsequent calorimetry and microscopy. The average grain size of the homogenized bulk samples was significantly larger than the grain size of the as received bulk samples. Also, observation of bulk sample cross-sections revealed that individual grains varied in size by as much as an order of magnitude. Micrographs 1a-1i are typical transverse cross-sections (mechanically polished, $FeCl_3$ etch), corresponding to bulk samples 1-9, and illustrate the wide variation in grain size within individual specimens and the difference in average grain size between as received and as homogenized bulk samples. Micrographs 1a-1e correspond to samples 1-5 and are 100X, whereas, Micrographs 1f-1i correspond to samples 6-9 and are 64X.

B. OPTICAL MICROSCOPY

Selected alloy B specimens were examined using optical microscopy techniques for the purpose of identifying structural features characterizing both the as received and as homogenized alloy B. What follows is a brief description of optical micrographs. Later, the results of optical microscopy will be correlated with TEM micrographs to support interpretation of observed changes in the kinetics of M$\longrightarrow$P and P$\longrightarrow$M phase transformations corresponding to selectively deformed and thermally cycled alloy B.

For clarity, the otical micrographs are organized into three groups. 1.) Micrographs 1a-1i correspond to transverse cross-sections (mechanically polished, $FeCl_3$ etched)

typical of bulk alloy B samples and illustrates: a.) the variation in size of individual grains present in representative cross-sections, b.) the disparity between as received and as homogenized average grain size, and c.) the effect of deformation upon structure. Micrograph 1a clearly illustrates the contrast in size among individual grains existing in undeformed martensitic as received alloy B. Micrographs 1a and 1f accentuate the disparity in average grain size between as received and as homogenized alloy B. Micrograph 1g corresponds to as homogenized alloy B (4.20% cold work); the herringbone pattern of martensite plates located within the large central grain is a characteristic structural feature associated with stress induced martensite to martensite transformations.

2.) Micrographs 2a-2i correspond to samples 1, 2, 4 and 5 (as received alloy B; 0.00%, 1.09%, 4.20% and 12.30% cold work). Each specimen was jet polished and photographed under polarized light to enhance structural contrast. Viewed in series, these micrographs illustrate a general structural trend. Micrographs 2a-2c show the regular, sharply defined alternating plate structure of undeformed, as received alloy B. With increased deformation, structures become less regular, once planar plate surfaces appear undulating, and intervariant boundaries are no longer sharp and straight (Micrographs 2d-2g). At deformation corresponding to 12.30% cold work (Micrographs 2h-2i), wavy

morphology dominates and resolution of structure by optical techniques is limited.

3.) Micrographs 3a-3d illustrate the dramatic change in structure accompanying thermal cycling of undeformed, as homogenized alloy B. The micrographs depict the same region of the specimen (jet polished and photographed under polarized light) after successive thermal cycles. Micrograph 3a shows the general plate morphology of as homogenized, uncycled alloy B. After the first complete thermal cycle (Micrograph 3b), the martensites appear splintered. The orientation of plates is less regular and intervariant boundaries are controted. With successive cycling (Micrographs 3c-3d), the martensites continued to change orientation with less favorably oriented variants disappearing. However, the splintered morphology was generally retained. Micrographs 4a-4b correspond to the as homogenized alloy after five and forty cycles. A new variant has apparently grown in the alloy due to repeated thermal cycling.

C. DIFFERENTIAL SCANNING CALORIMETRY

Differential scanning calorimetry data was collected on alloy specimens prepared from bulk samples 1-9 (Table I). The Perkin-Elmer (DSC-2) Differiential Scanning Calorimeter was calibrated in accordance with procedures outlined in [Ref. 23]. The actual operational settings for the

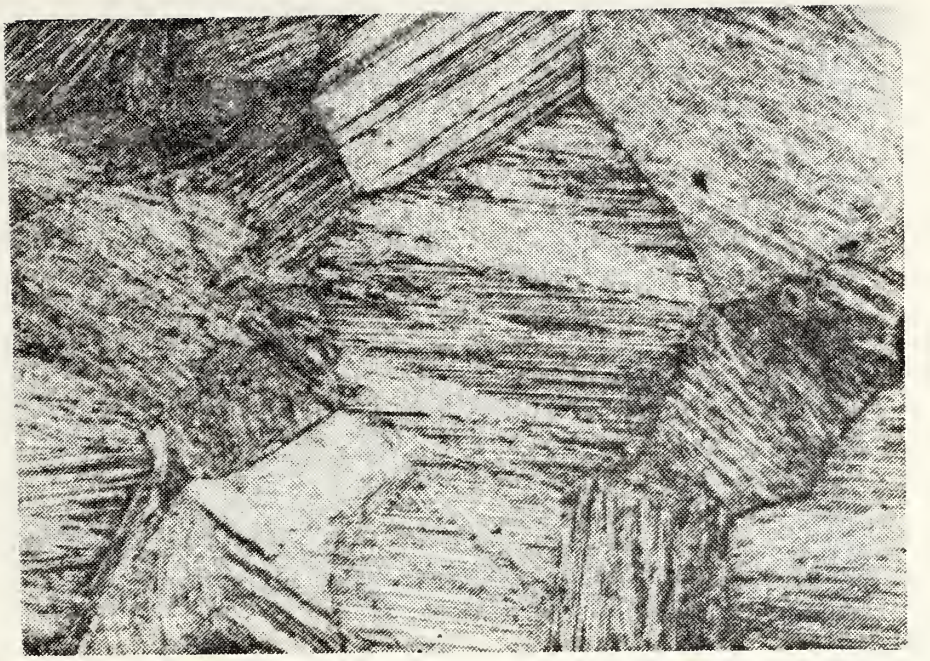

Micrograph 1a. Sample 1, alloy B as received, 0.00% cold work, martensitic structure. (optical, $FeCl_3$ etch, 100X

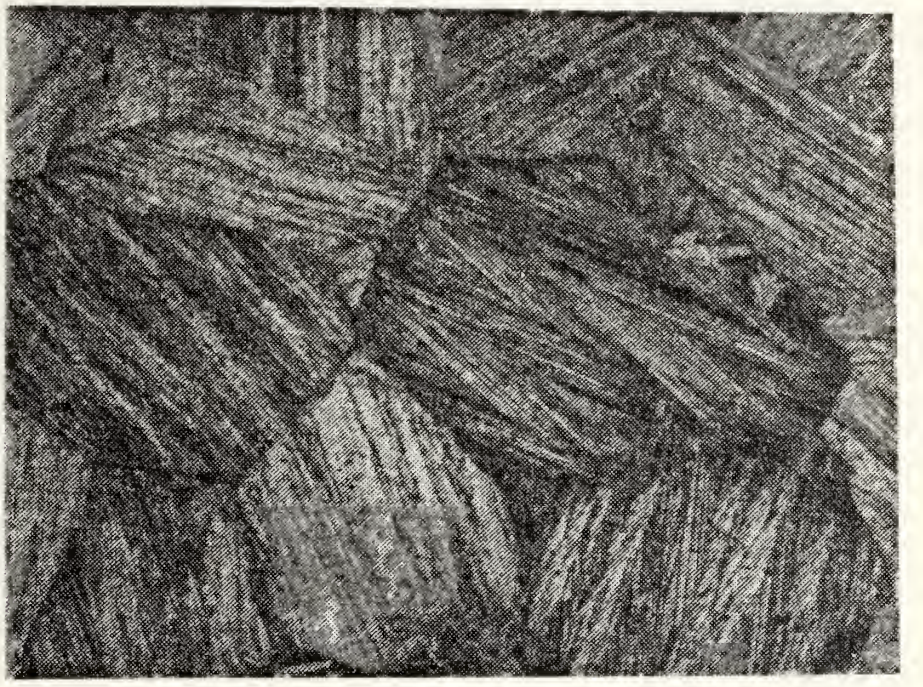

Micrograph 1b. Sample 2, alloy B as received, 1.09% cold work, martensitic structure. (optical, $FeCl_3$ etch, 100X)

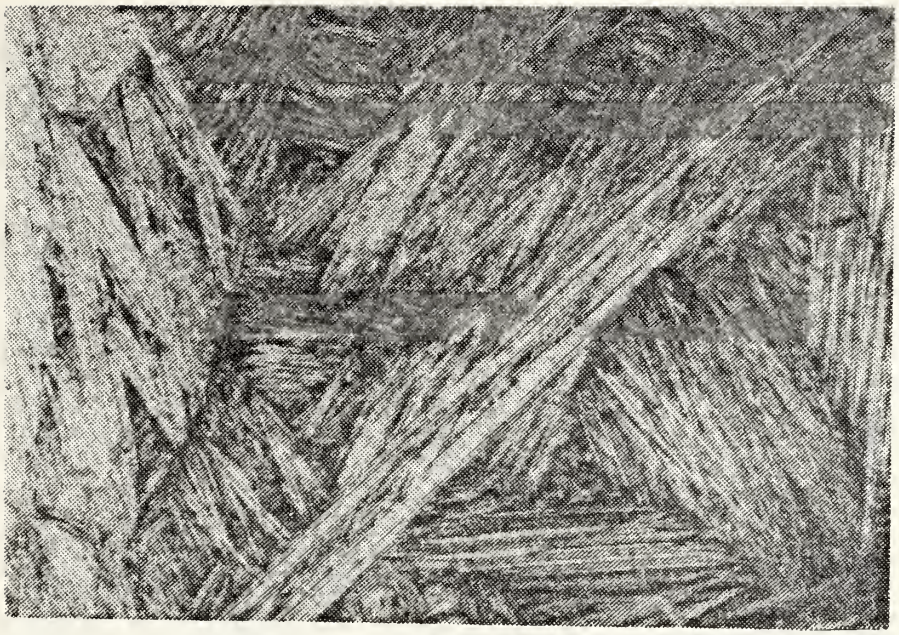

Micrograph 1c. Sample 3, alloy B as received, 2.57% cold work, martensitic structure. (optical, $FeCl_3$ etch, 100X)

Micrograph 1d. Sample 4, alloy B as received, 4.20% cold work, martensitic structure. (optical, $FeCl_3$ etch, 100X)

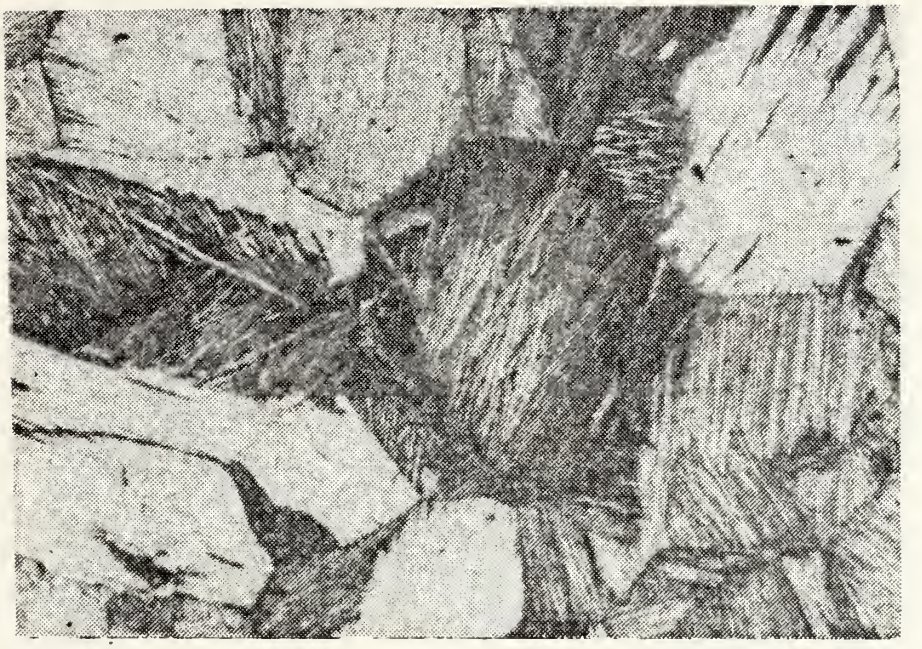

Micrograph 1e. Sample 5, alloy B as received, 12.30% cold work, martensitic structure. (optical, $FeCl_3$ etch, 100X)

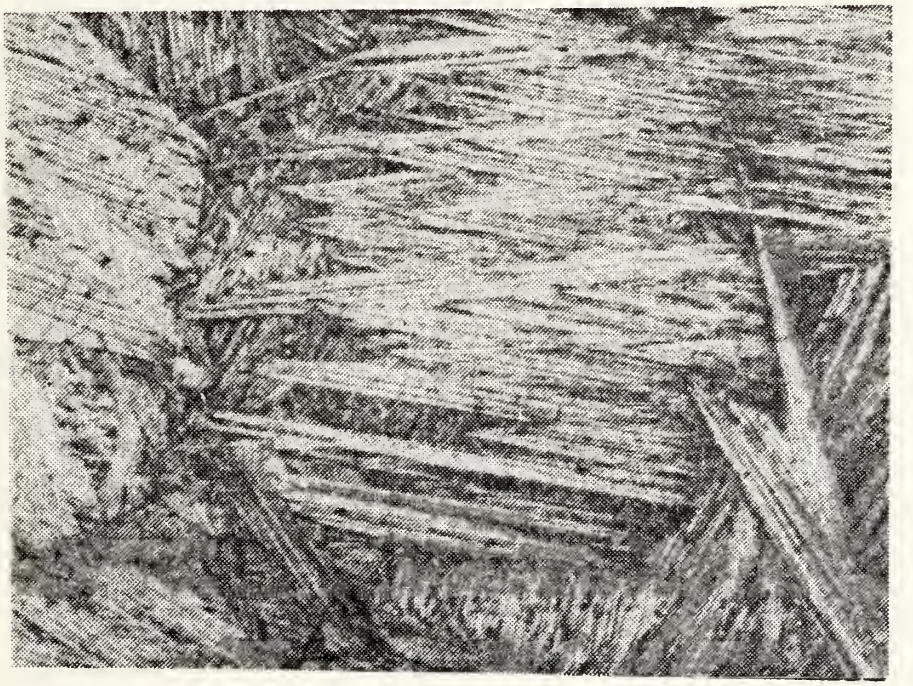

Micrograph 1f. Sample 6, alloy B annealed and quenched, 0.00% cold work, martensitic structure. (optical $FeCl_3$ etch, 64X)

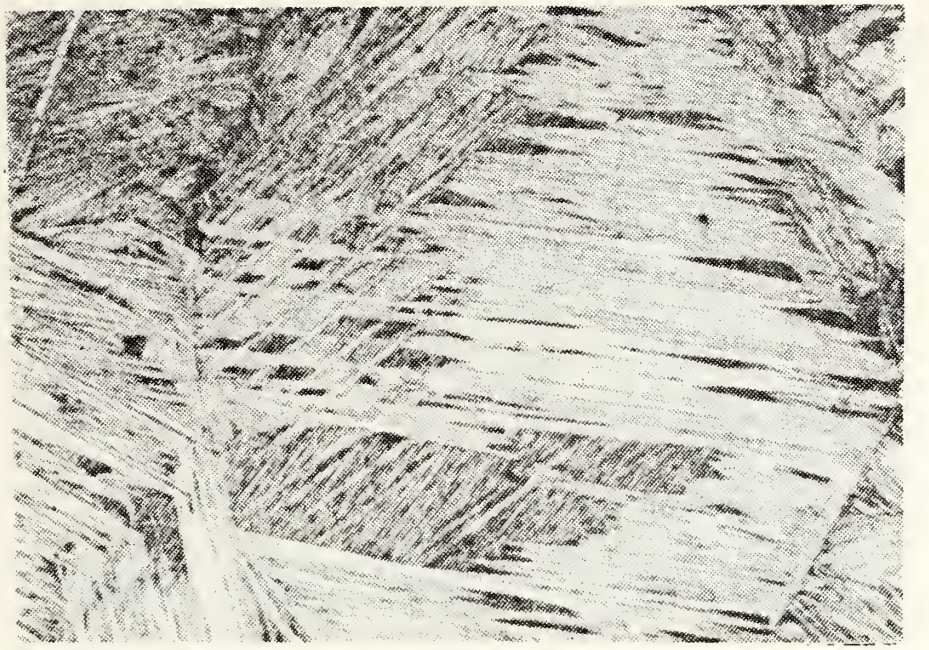

Micrograph 1g. Sample 7, alloy B annealed and quenched, 4.20% cold work, martensitic structure. (optical $FeCl_3$ etch, 64X)

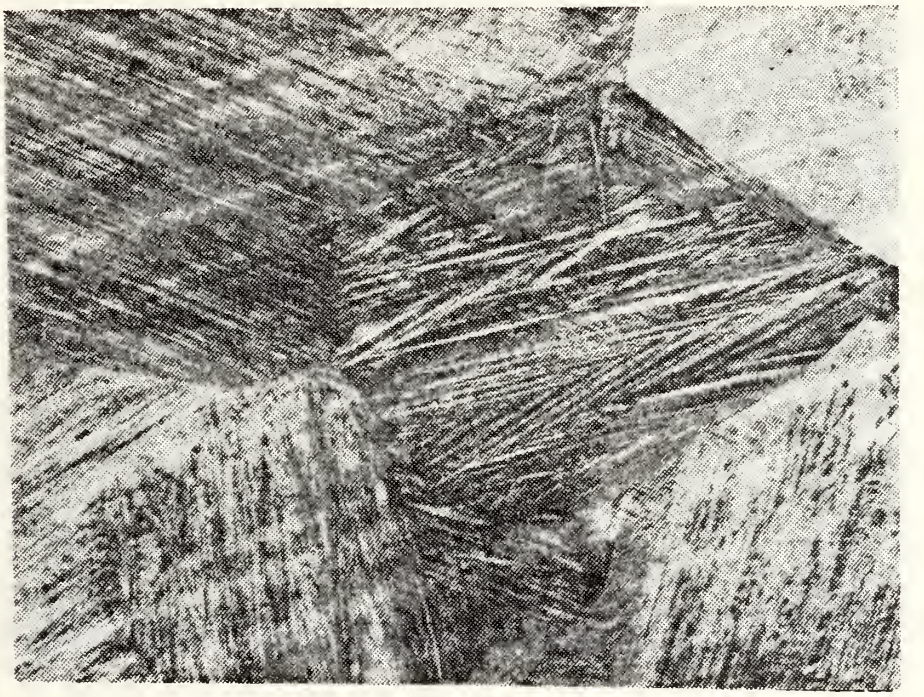

Micrograph 1h. Sample 8, alloy B annealed and quenched, 7.15% cold work, martensitic structure. (optical $FeCl_3$ etch, 64X)

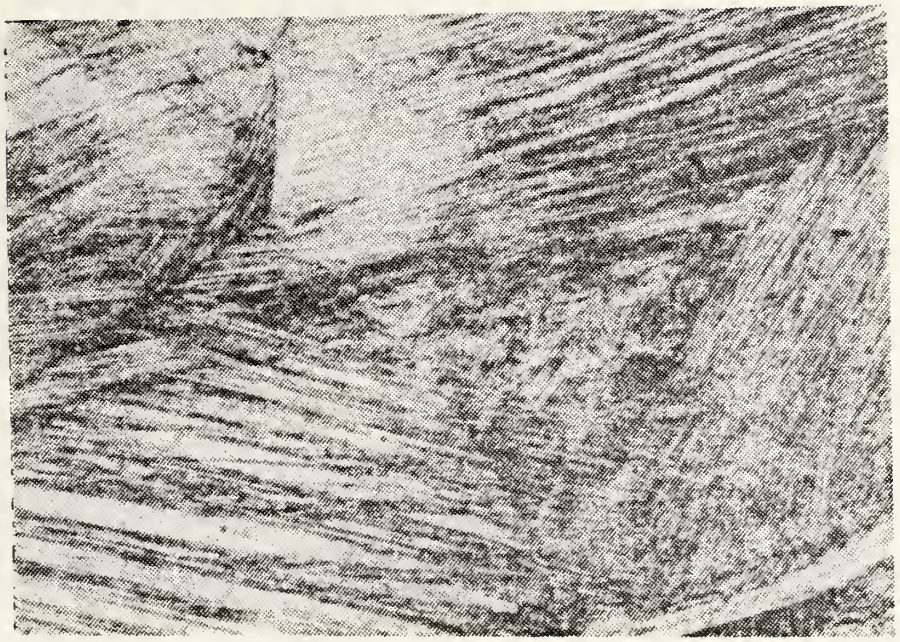

Micrograph 1i. Sample 9, alloy B annealed and quenched, 10.36% cold work, martensitic structure. (optical $FeCl_3$ etch, 64X)

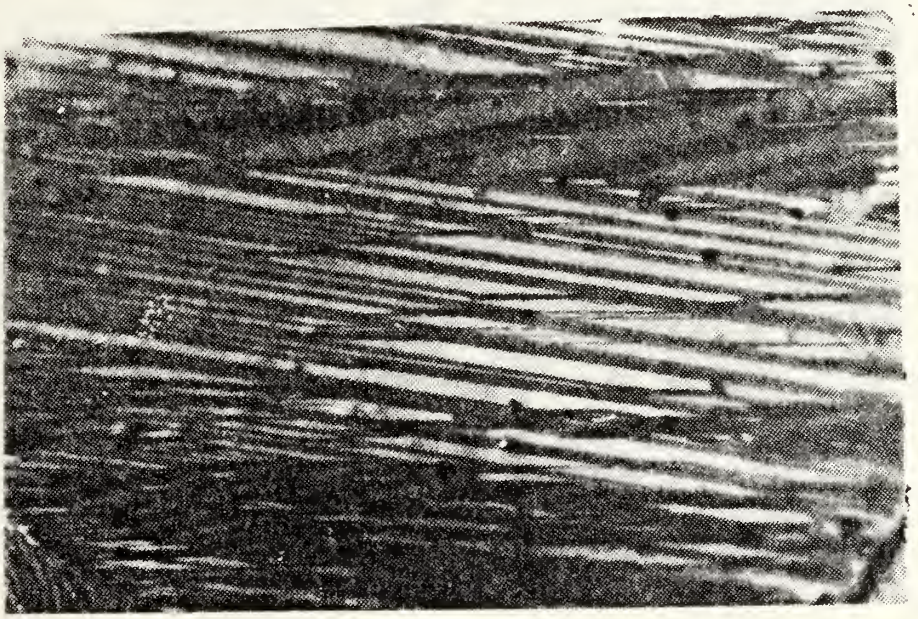

Micrograph 2a. As received alloy B. Regular, sharply defined, plate-like structures are evident. (jet polished, polarized light, 189X)

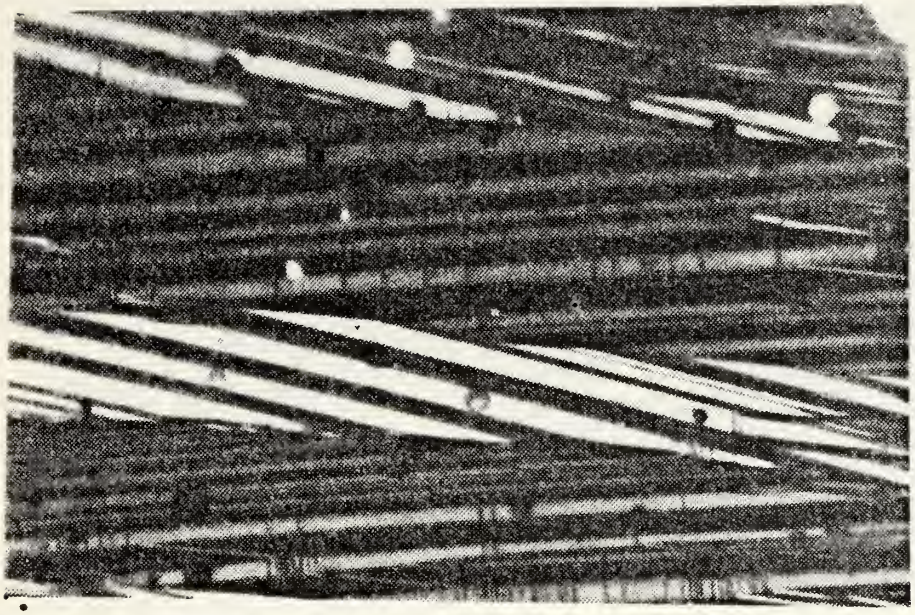

Micrograph 2b. As received alloy B. The martensitic alloy exhibits regular, planar, alternating plate-like morphology. (jet polished, polarized light, 189X)

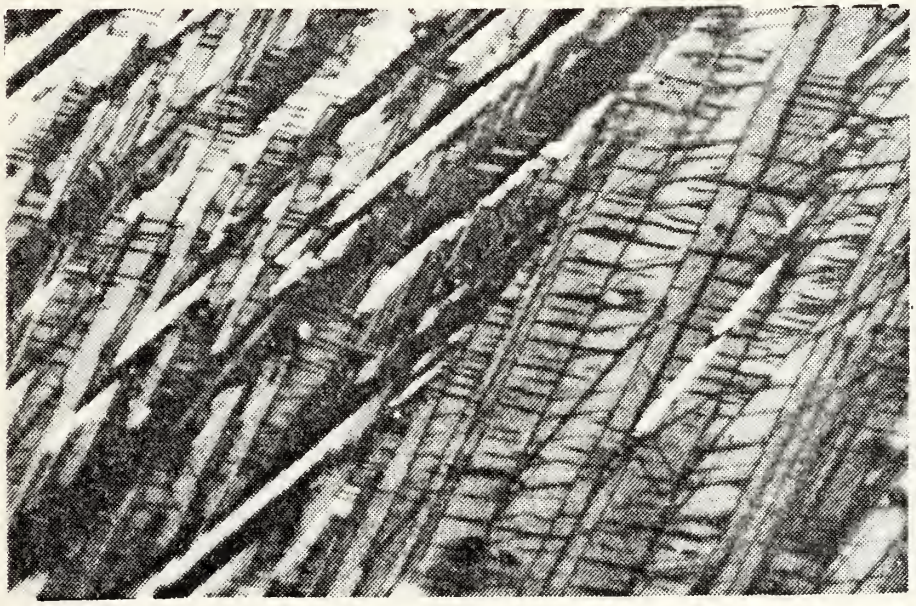

Micrograph 2c. As received alloy B. (jet polished, polarized light, 375X)

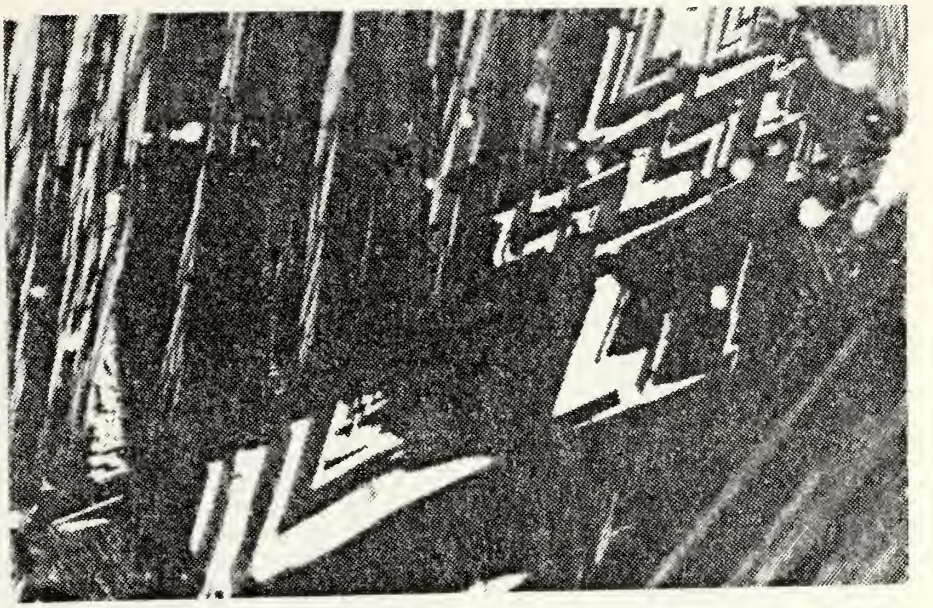

Micrograph 2d. As received alloy B (1.09% cold work). Variant/plate curvature is evident in the slightly deformed alloy. (jet polished, polarized light, 189X)

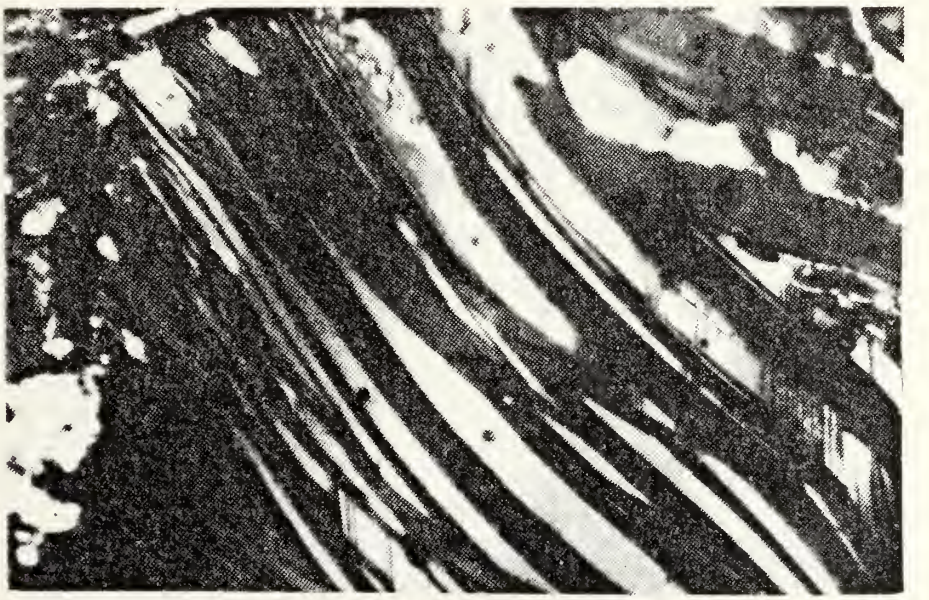

Micrograph 2e. As received alloy B (1.09% cold work). (jet polished, polarized light, 375X)

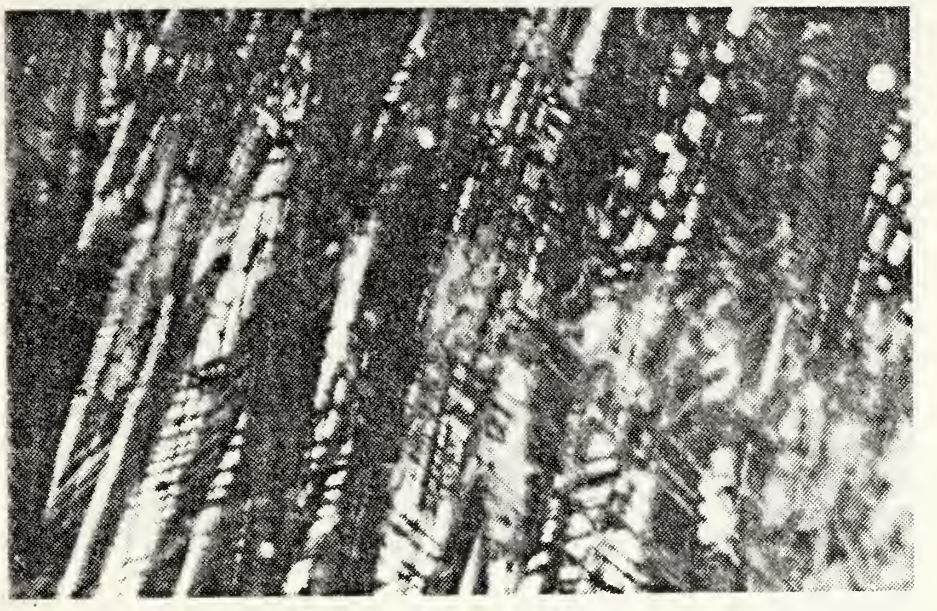

Micrograph 2f. As received alloy B (4.20% cold work). The martensite plates appear distorted giving the overall structure a wavy appearance. (jet polished, polarized light, 375X)

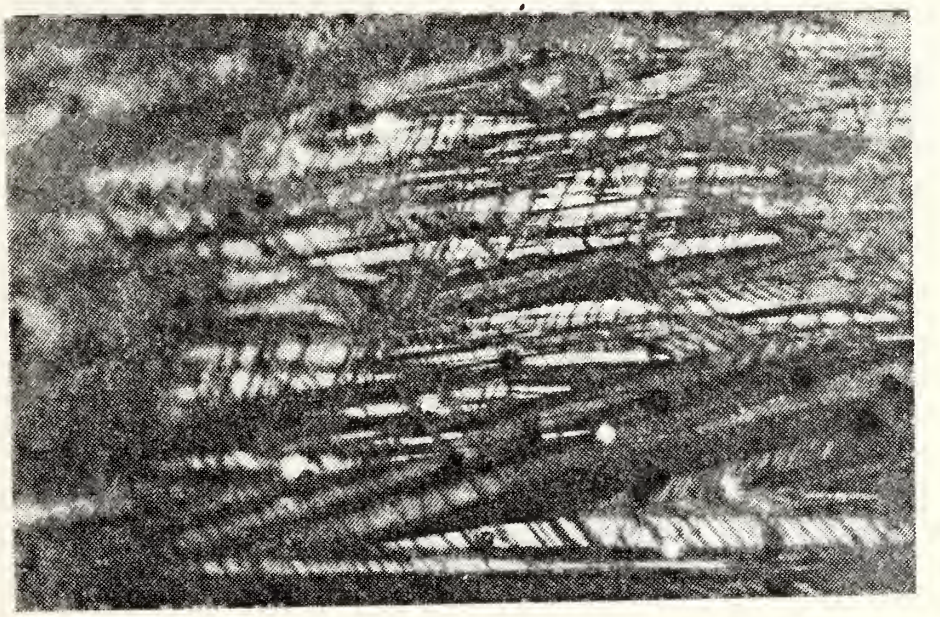

Micrograph 2g. As received alloy B (4.20% cold work). Curvature of plate surfaces and boundaries is evident. (jet polished, polarized light, 375X)

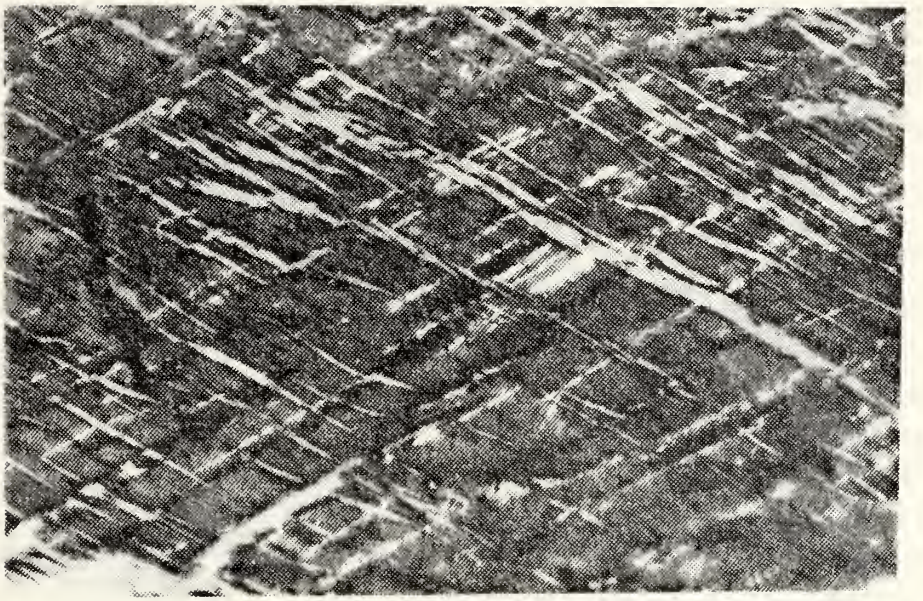

Micrograph 2h. As received alloy B (12.30% cold work). Wavy morphology characterizes advanced deformation. (jet polished, polarized light, 375X)

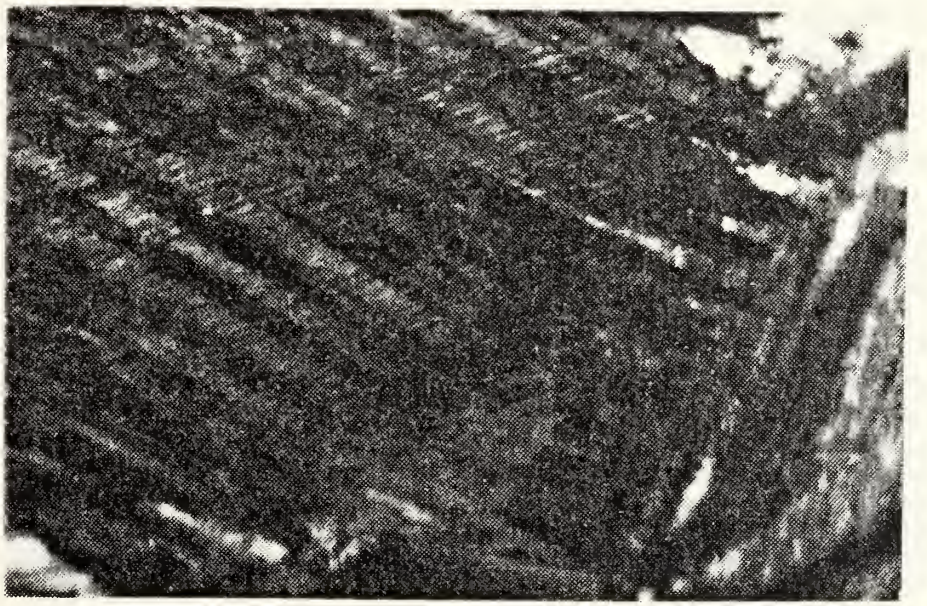

Micrograph 2i. As received alloy B (12.30% cold work). Optical resolution of structure is limited, wavy morphology. (jet polished, polarized light, 375X)

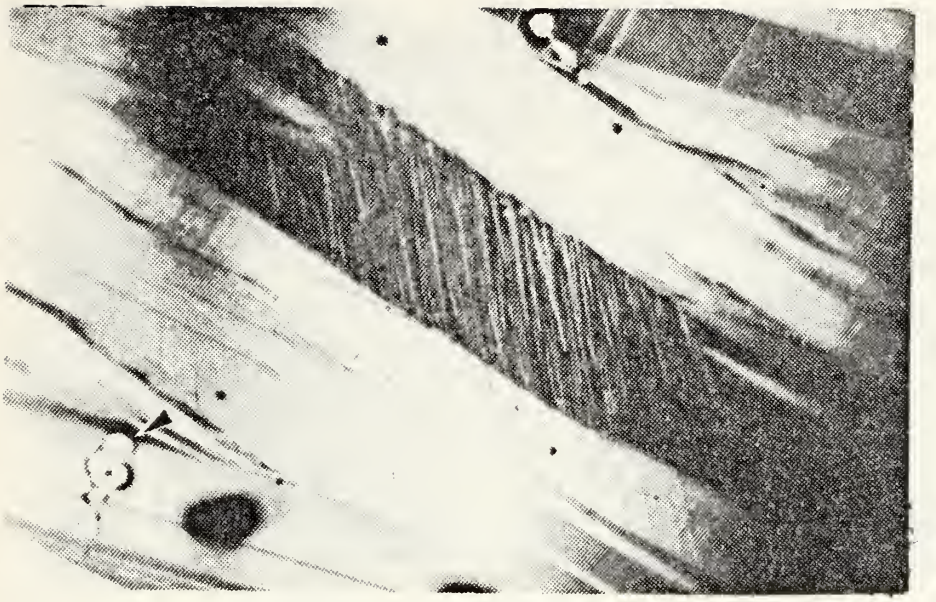

Micrograph 3a. As homogenized alloy B (uncycled). General view, showing sharply defined, regular, plate morphology. (jet polished, polarized light, 375X)

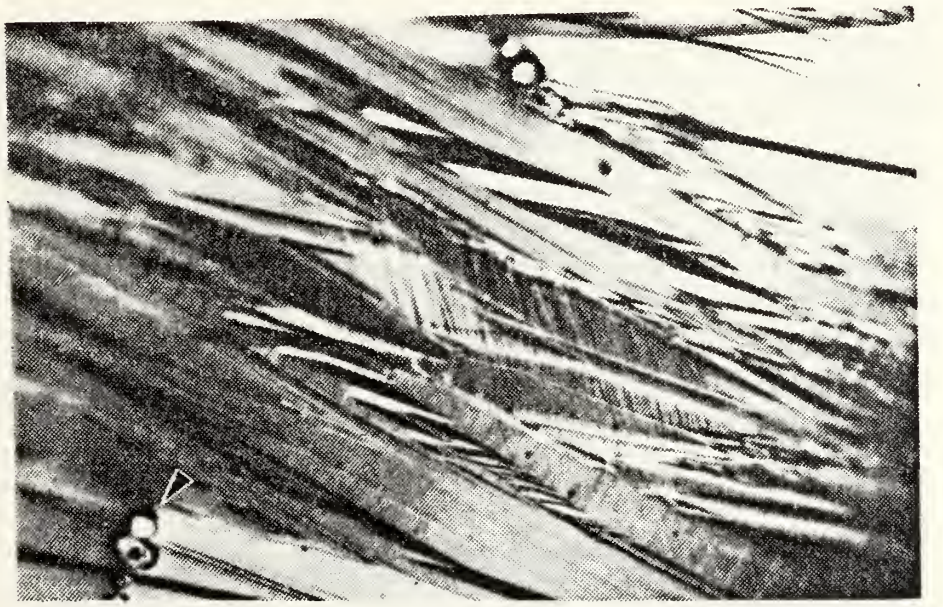

Micrograph 3b. As homogenized alloy B (1 thermal cycle). Preferential growth and shrinkage of martensite variants is evident. Splintered morphology. (jet polished, polarized light, 375X)

Micrograph 3c. As homogenized alloy B (2 thermal cycles). Growth, shrinkage and splintering of variants are evident. (jet polished, polarized light, 375X)

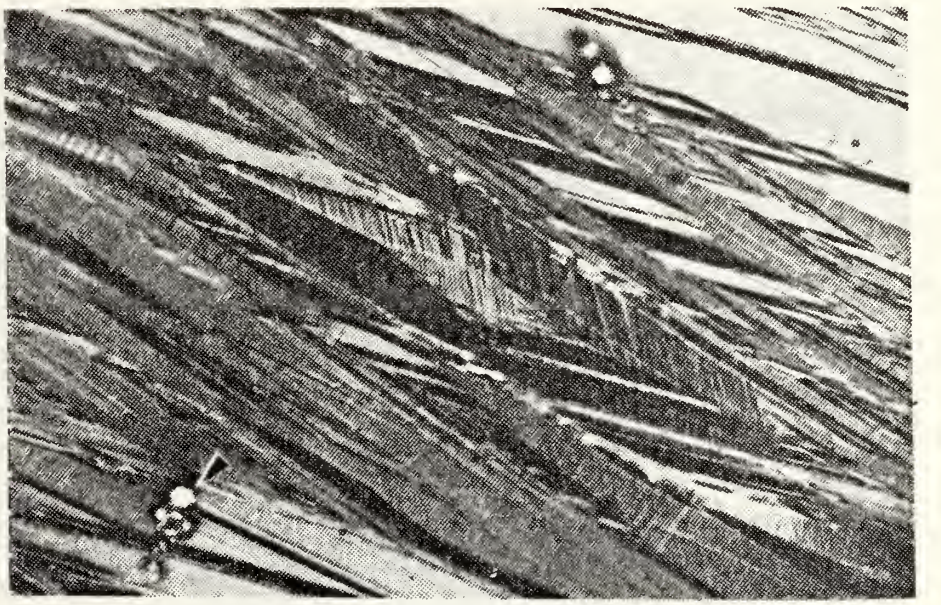

Micrograph 3d. As homogenized alloy B (3 thermal cycles). (jet polished, polarized light, 375X)

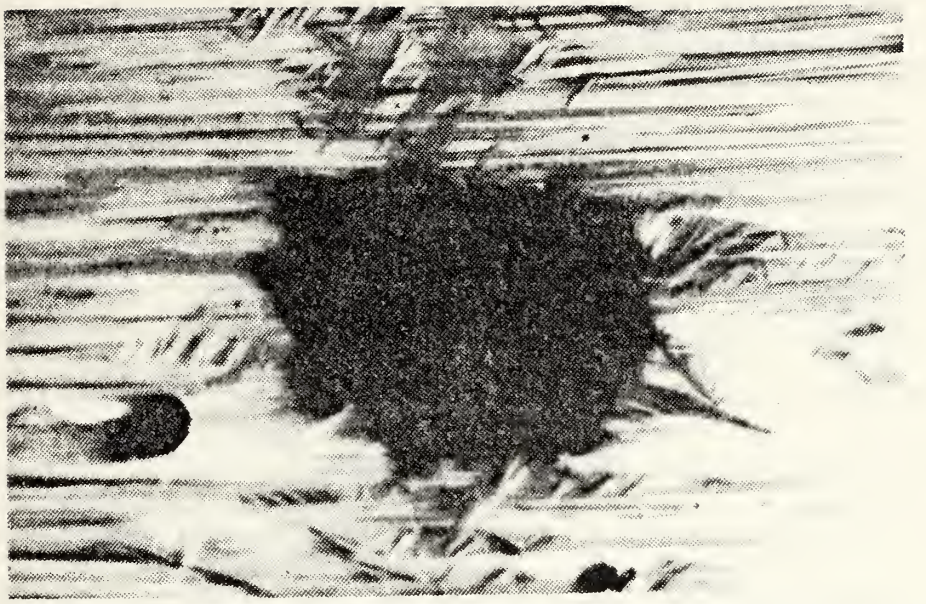

Micrograph 4a. As homogenized alloy B (5 thermal cycles). Star shaped variant was produced in plate-like martensitic matrix due to cycling. (jet polished, polarized light, 375X)

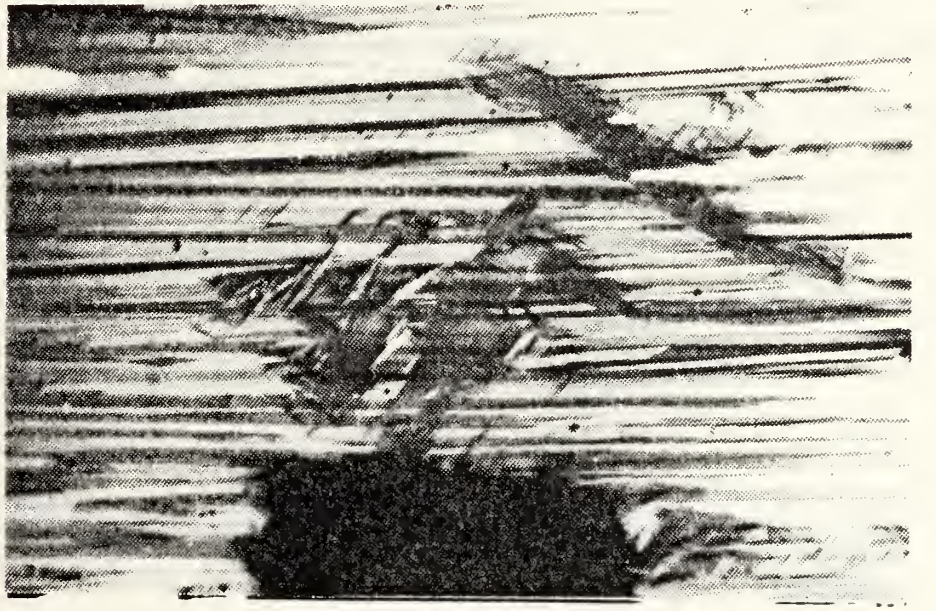

Micrograph 4b. As homogenized alloy B (40 thermal cycles). Star shaped variant in plate-like martensitic matrix. (jet polished, polarized light, 375X)

Perkin-Elmer (DSC-2) are listed in the Appendix. These machine parameters were held constant for all calorimetry experiments. Repeated calibration trials using control samples demonstrated that the Perkin-Elmer (DSC-2) Differential Scanning Calorimeter was extremely sensitive to refrigeration unit warm-up time and nitrogen purge gas pressure. To achive reproducible calorimetry data, the refrigeration unit required a minimum 24 hour warm-up to assure approximate steady state conditions at the sample holder coolant block, and optimum purge gas pressure was determined to be 25 psi at the outlet of the tank regulator.

The original DSC strip chart data was reduced and transformation curves replotted using the DISSPLA graphics program with parametric curve fitting and smoothing routines (Figures 2-17). The kinetic parameters recorded for M$\longrightarrow$P and P$\longrightarrow$M phase transformations for alloy B samples 1-9 were determined from original DSC strip chart data according to guidelines established previously, and documented in the Experimental Procedures section of this report (Tables II-IX).

To address the calorimetry results (Figures 2-17, Tables II-IX) lucidly, a terse summary describing what the figures and tables represent and in what sequence the DSC data will be analyzed is appropriate.

Figures 2-9 depict the transformation endotherms and exotherms for three complete thermal cycles of as received alloy B samples 1-4 (0.00%, 1.09%, 2.57% and 4.20% cold work).

Tables II-V list the kinetic parameters associated with M→P and P→M transformations for thermally cycled as received samples 1-4 and correspond to Figures 2-9. Figures 10-11 and Table VI compositely depict the transformation endotherms and exotherms and list the kinetic parameters for the third complete cycle of as received alloy B samples 1-4.

Figures 12-15 and Tables VI-VIII display the transformation data for annealed and quenched alloy B DSC specimens. Figures 12-15 depict the transformation endotherms and exotherms for three complete thermal cycles of as homogenized samples 6 and 7 (0.00% and 4.20% cold work). Tables VII-VIII list the kinetic parameters for the transformation processes associated with thermally cycled samples 6 and 7, and correspond to Figures 12-15. Figures 16-17 and Table IX compositely depict the transformation endotherms and exotherms, and list the kinetic parameters for the third complete thermal cycle of alloy B samples 1, 6 and 7 (as received 0.00% cold work; as homogenized, 0.00% and 4.20% cold work respectively).

The format for presentation and analysis of DSC data follows: 1.) comparison of M→P transformation endotherms corresponding to heating half cycles 1, 2 and 3 for individual as received and as homogenized samples; 2.) comparison of P→M transformation exotherms corresponding to cooling half cycles 1, 2 and 3 for individual as received and as homogenized samples; 3.) comparison of heating half

cycle 3 M⟶P transformation endotherms as a function of cold work corresponding to as received samples 1-5; 4.) comparison of cooling half cycle 3 P⟶M transformation exotherms as a function of cold work corresponding to as received samples 1-5; 5.) comparison of heating half cycle 3 M⟶P transformation endotherms as a function of cold work corresponding to as homogenized samples 6-7; 6.) comparison of cooling half cycle 3 P⟶M transformation exotherms as a function of cold work corresponding to as homogenized samples 6-7; and 7.) comparison of M⟶P and P⟶M cycle 3 transformation endotherms and exotherms for as received and as homogenized alloy samples 1 and 6 (0.00% cold work).

1.) Focusing upon the first three heating half cycles of as received alloy B, 0.00% cold work (Figure 2, Table II), the most prominent changes among endotherms occured between heating half cycle 1 and 2. Endotherms 2 and 3, and correspondingly A_s, A_f and A_{max} for half cycles 2 and 3 are shifted significantly to the left (Figure 2) toward lower temperatures relative to endotherm 1. Comparison of sample 1, endotherms 1 and 2, with respect to kinetic parameters A_{height} and A_{width} demonstrate that the M⟶P transition was occuring more rapidly and was confined to a narrower temperature band after the first heating half cycle. Consequently, endotherm 1 appears flatter and broader and displaced toward higher temperatures than subsequent endotherms corresponding to further cycling of the

same material. This trend (disparity between endotherms 1 and 2) was realized generally for all samples tested (Figures 2, 4, 6, 8, 12, 14; Tables II, III, IV, V, VII, VIII) with notable exceptions occuring for samples cold worked beyond approximately 7% where no M⟶P nor P⟶M transitions were observed to occur, that is any transition that may have been occuring was hidden in the baseline noise of the chart recorder.

2.) In contrast to the M⟶P transformations and focusing upon the first three cooling half cycles of as received alloy B, 0.00% cold work (Figure 3, Table II), only subtle differences were observed between exotherms 1, 2 and 3. M_{max}, the temperature at which the greatest quantity of material was undergoing transformation remained constant at 322.5 K, and only small changes among the other measured parameters (M_s, M_f, M_{height}, M_{width} and M_{area}) occured. This is consistent with findings by Perkins and Muesing [Ref. 11]. Working with Cu-Zn-Al shape memory alloys, Perkins and Muesing observed that: a.) M_{max} remained essentially stationary for the first few thermal cycles, eventually shifting toward higher temperatures as the number of cycles increased and preferred nucleation sites were established; b.) M_s and A_f temperatures increased as thermal cycling progressed due to stablization of martensite; and c.) A_{max} - M_{max} hysteresis diminished as thermal cycling continued. This uniformity between exotherms 1, 2 and 3 for samples of

identical heat treatment and initial deformation was realized generally for all samples tested where the transformation process could be discerned above recorder baseline clutter (Figures 3, 5, 7, 9, 13, 15; Tables II, III, IV, V, VII, VIII).

Analysis of the M→P and P→M phase transformations as a function of initial deformation below M_f, for both as received and as homogenized samples was restricted to comparison of third cycle endotherms and exotherms and corresponding kinetic parameters. Adoption of this procedure assures that any variation in kinetic parameters are due to differences in initial sample deformation and not a consequence of thermal history. Secondly, limiting analysis to third cycle transitions avoids comparison of the anomalous behavior, previously addressed, which was observed to occur between the first and subsequent M→P transformations of all DSC specimens tested.

3.) DSC third cycle transformation endotherms for as received alloy B samples 1-4 corresponding to 0.00%, 1.09%, 2.57% and 4.20% cold work are compositely depicted in Figure 10. The associated kinetic parameters are listed in Table VI. There were no large disparities noted between the transformation endotherms for samples 1-3. A_s, A_f and A_{max} remained relatively stable at about 301 K, 349 K and 331 K respectively. A_{height} decreased modestly from 12.9 mcal/gm-sec to 11.6 mcal/gm-sec as initial cold work increased from

0.00% to 2.57%, and correspondingly M_{width} increased modestly from 6.0 K to 6.2 K. The energy of the M⟶P transformation process differed by only 10% between samples 1-3. However, the sample 4 M⟶P cycle 3 transformation endotherm differed markedly from those of samples 1-3. Although, A_s and A_{max} values for sample 4 differed only slightly from those of samples 1-3; A_{height} and A_{area} were significantly depressed, A_{width} was markedly broader and A_f was extended to 367.5 K.

4.) The DSC P⟶M transformation exotherms, cycle 3, for as received alloy B samples 1-4 (Figure 11, Table VI) showed a similar tendency to remain reasonably stable for initial deformations below M_f corresponding to cold work less than 4.20%, and to change dramatically for sample 4, as had respective M⟶P transformation endotherms (Figure 10, Table VI). Comparing sample 4 exotherms with those of samples 1-3, it was found that M_s, M_f and M_{max} were shifted toward lower temperatures, M_{height} and M_{area} significantly decreased, and M_{width} markedly expanded.

The DSC data available for precise analysis of as homogenized alloy B was limited, in that DSC transformation endotherms and exotherms and associated kinetic parameters were obtained only for samples subjected to 0.00% and 4.20% cold work. In addition, the curves generated during thermal cycling for as homogenized samples deviated only slightly from the baseline clutter of the chart recorder.

Consequently, reconstruction of transformation profiles and measurement of kinetic parameters from reduced strip chart data suffered from inherent inaccuracies.

5.) DSC transformation endotherms, cycle 3, for as homogenized alloy B samples 6-7 corresponding to 0.00% and 4.20% cold work are depicted in Figure 16. The associated kinetic parameters are listed in Table IX. The cycle 3, as homogenized alloy B sample 7 endotherms was significantly different than the corresponding sample 6 endotherm. Although A_f and A_{max} remained constant, increased initial deformation resulted in lower A_s, depression of A_{height} and A_{area}, and increased A_{width}.

6.) The DSC P$\rightarrow$M, cycle 3 transformation exotherms for as homogenized samples 6-7 and associated kinetic parameters (Figure 17, Table IX) illustrate the same tendency toward dramatic change in the transformation process for as homogenized alloy B specimens subjected to initial deformation corresponding to 4.20% cold work, as had associated endothermic M$\rightarrow$P transition data (Figure 16, Table IX). Although M_s, M_f and M_{max} remained essentially stable for higher initial deformation, M_{height} and M_{area} were significantly depressed, and M_{width} decreased by approximately 45%.

7.) Finally, comparison of third cycle DSC profiles and associated kinetic parameters for undeformed as received and as homogenized alloy B samples 1 and 6 (Figure 16 - 17,

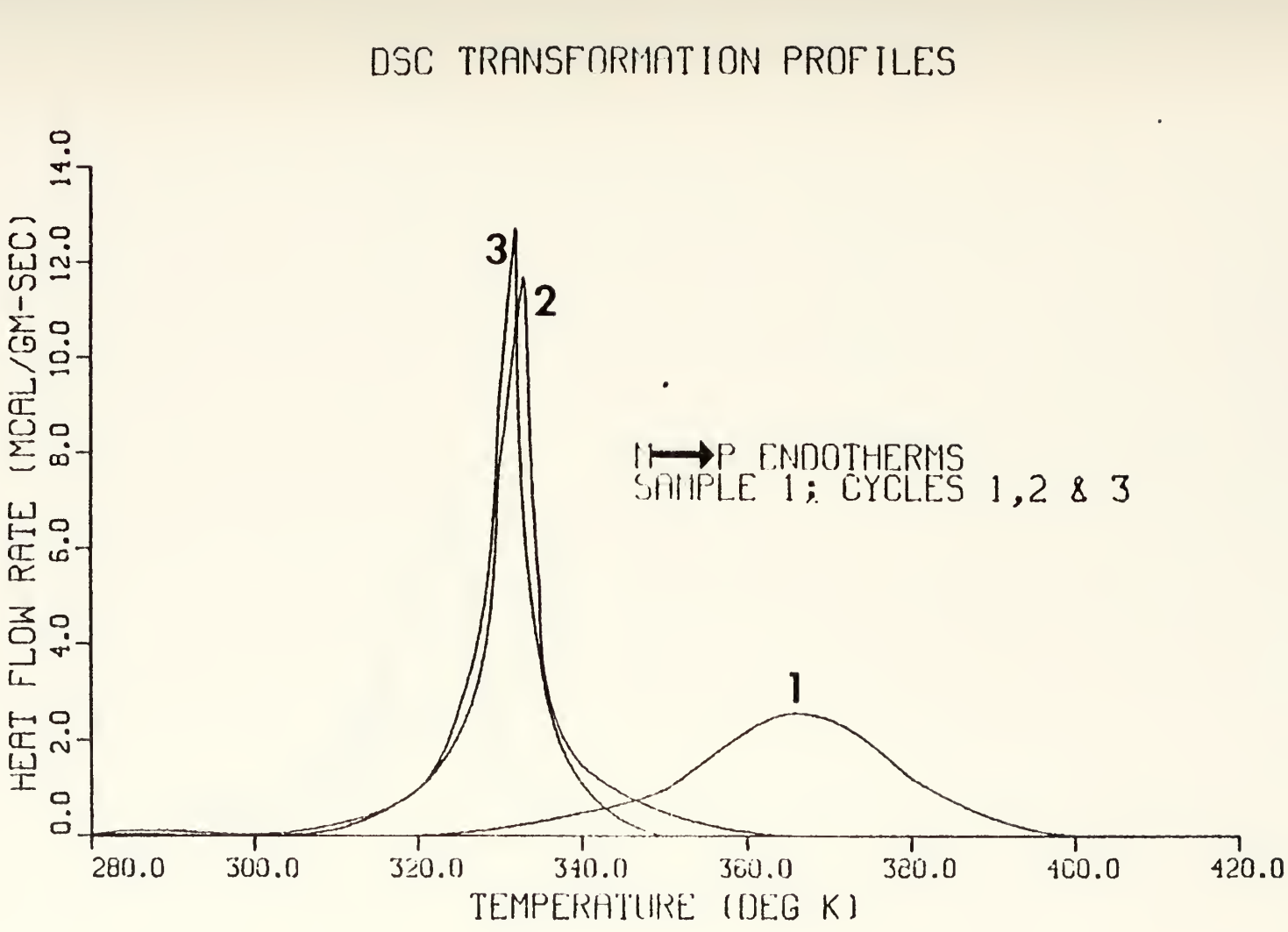

Figure 2. Sample 1, alloy B as received, 0.00% cold work, DSC M⟶P transformation endotherms, cycles 1, 2 and 3.

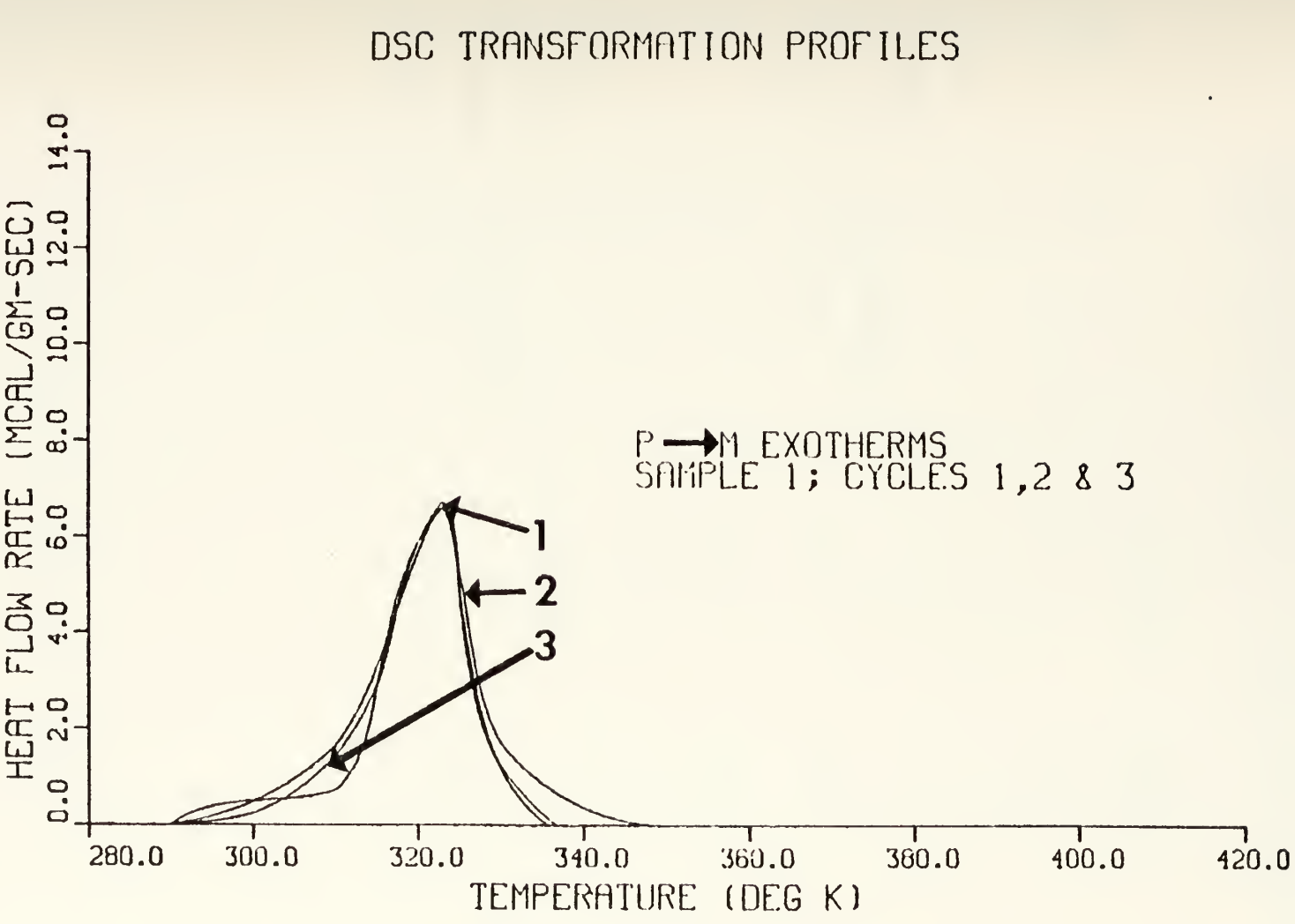

Figure 3. Sample 1, alloy B as received, 0.00% cold work, DSC P→M transformation exotherms, cycles 1, 2 and 3.

TABLE II

Kinetic parameters for M → P and P → M transformations: sample 1, alloy B as received, 0.00% cold work, cycles 1, 2 and 3.

		Cycle 1	Cycle 2	Cycle 3
M_s	(K)	347.0	337.0	338.0
M_f	(K)	290.0	291.0	292.0
M_{max}	(K)	322.5	322.5	322.5
M_{width}	(K)	12.5	12.0	12.0
M_{height}	(mcal/gm-sec)	6.5	6.6	6.7
M_{area}	(mcal/gm)	612.2	480.5	492.3
A_s	(K)	321.5	305.5	303.0
A_f	(K)	400.0	363.5	349.5
A_{max}	(K)	366.0	333.0	331.0
A_{width}	(K)	28.0	6.4	6.0
A_{height}	(mcal/gm-sec)	2.6	11.6	12.9
A_{area}	(mcal/gm)	472.1	880.4	1132.3

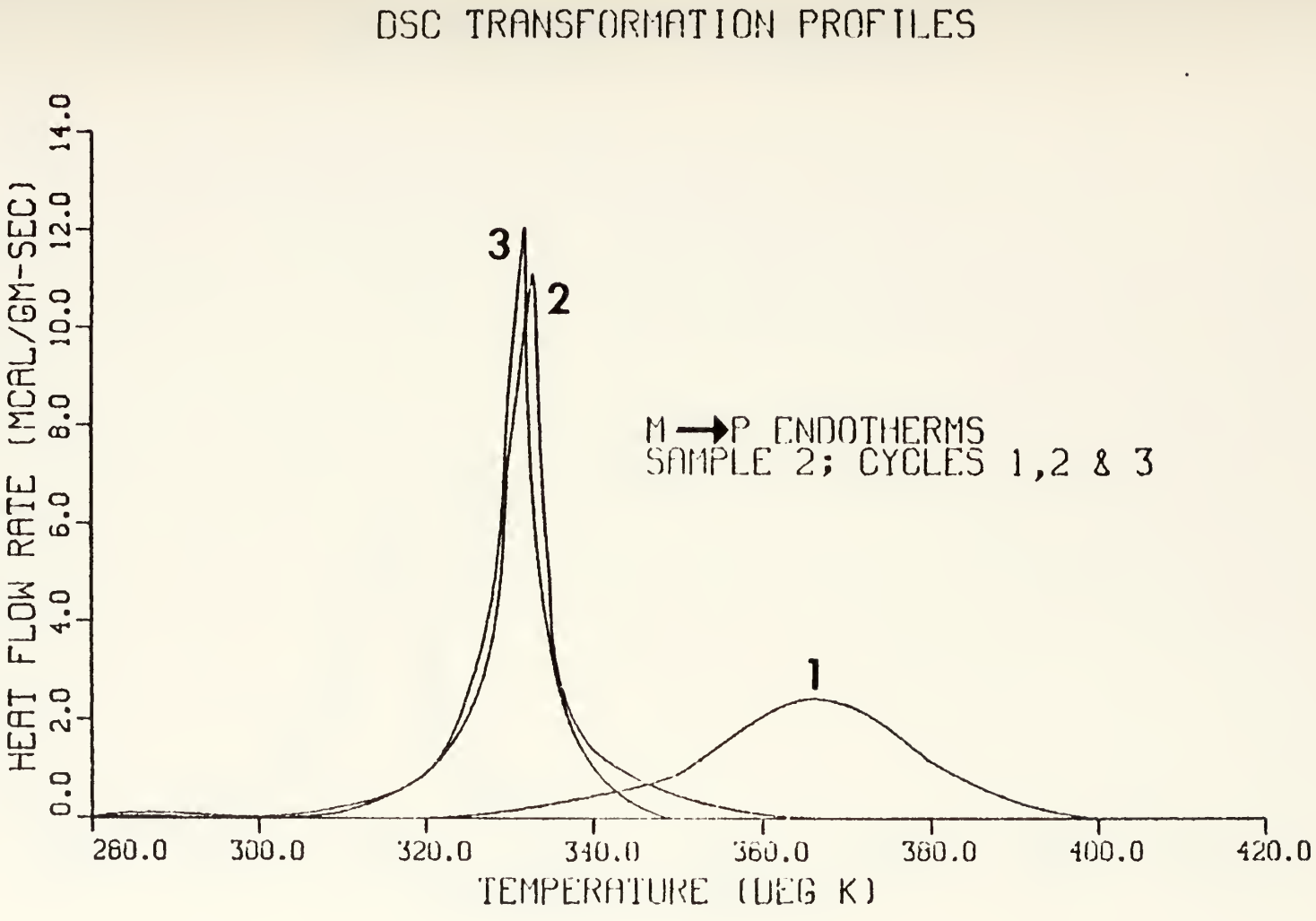

Figure 4. Sample 2, alloy B as received, 1.09% cold work, DSC M → P transformation endotherms, cycles 1, 2 and 3.

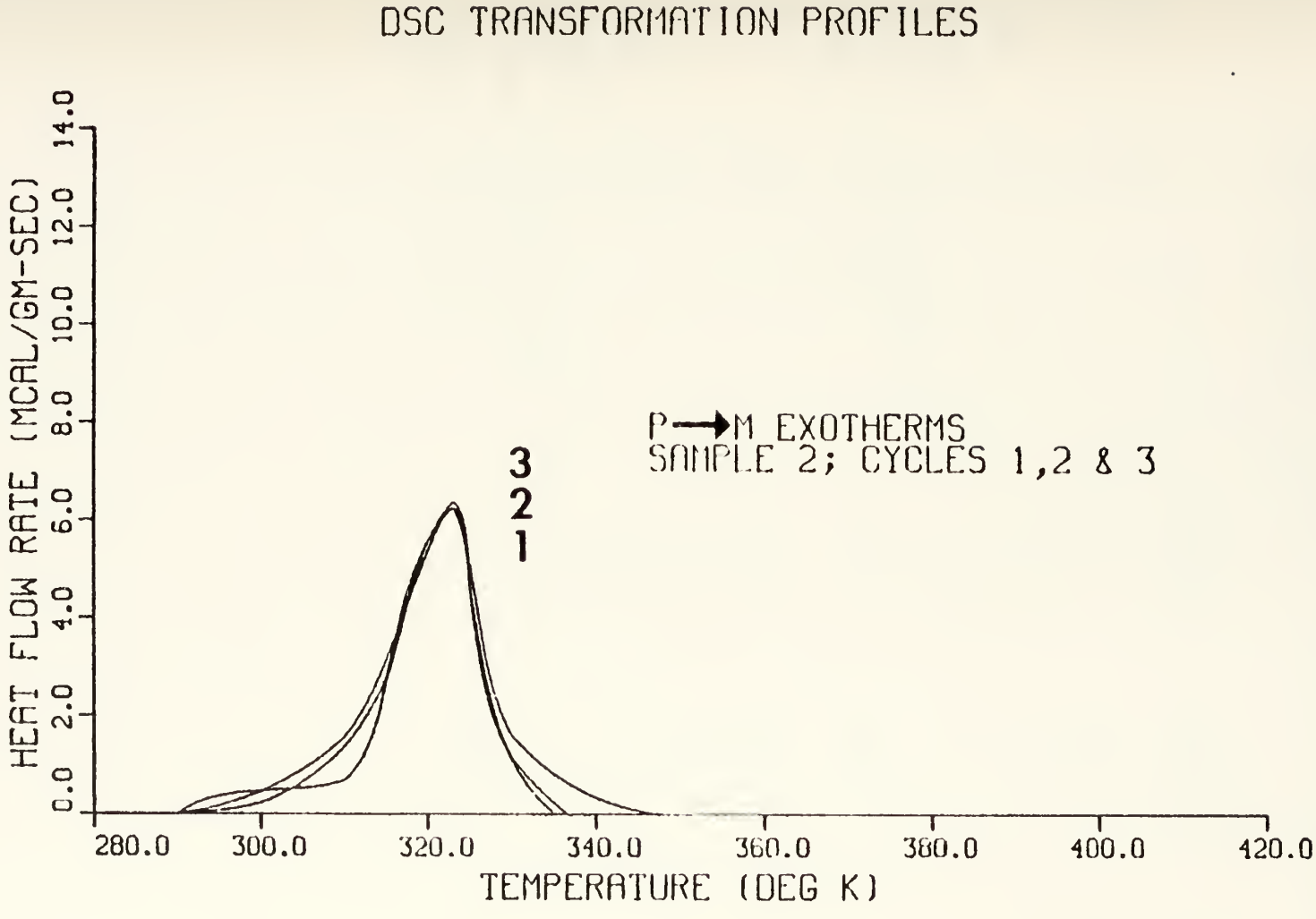

Figure 5. Sample 2, alloy B as received, 1.09% cold work, DSC P⟶M transformation exotherms, cycles 1, 2 and 3.

TABLE III

Kinetic parameters for M → P and P → M transformations: sample 2, alloy B as received, 1.09% cold work, cycles 1, 2 and 3.

		Cycle 1	Cycle 2	Cycle 3
M_s	(K)	347.0	337.0	338.0
M_f	(K)	290.0	291.4	292.5
M_{max}	(K)	322.5	322.5	322.5
M_{width}	(K)	12.6	12.3	12.0
M_{height}	(mcal/gm-sec)	6.1	6.2	6.3
M_{area}	(mcal/gm)	581.3	456.7	470.5
A_s	(K)	320.0	305.5	300.0
A_f	(K)	399.5	366.0	348.5
A_{max}	(K)	366.0	333.2	331.0
A_{width}	(K)	28.1	6.6	6.2
A_{height}	(mcal/gm-sec)	2.5	11.0	12.3
A_{area}	(mcal/gm)	448.3	836.7	1075.9

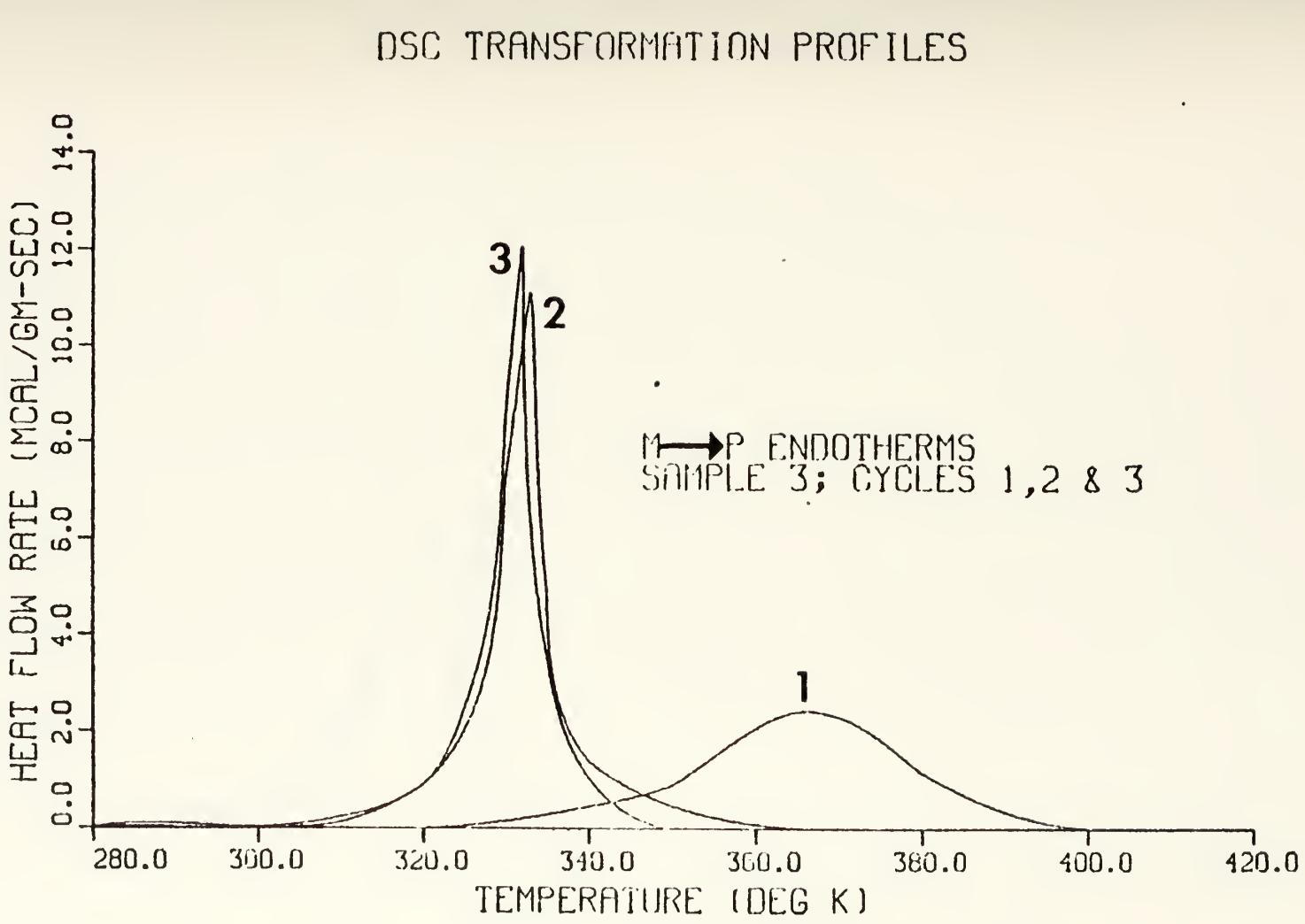

Figure 6. Sample 3, alloy B as received, 2.57% cold work, DSC M⟶P transformation endotherms, cycles 1, 2 and 3.

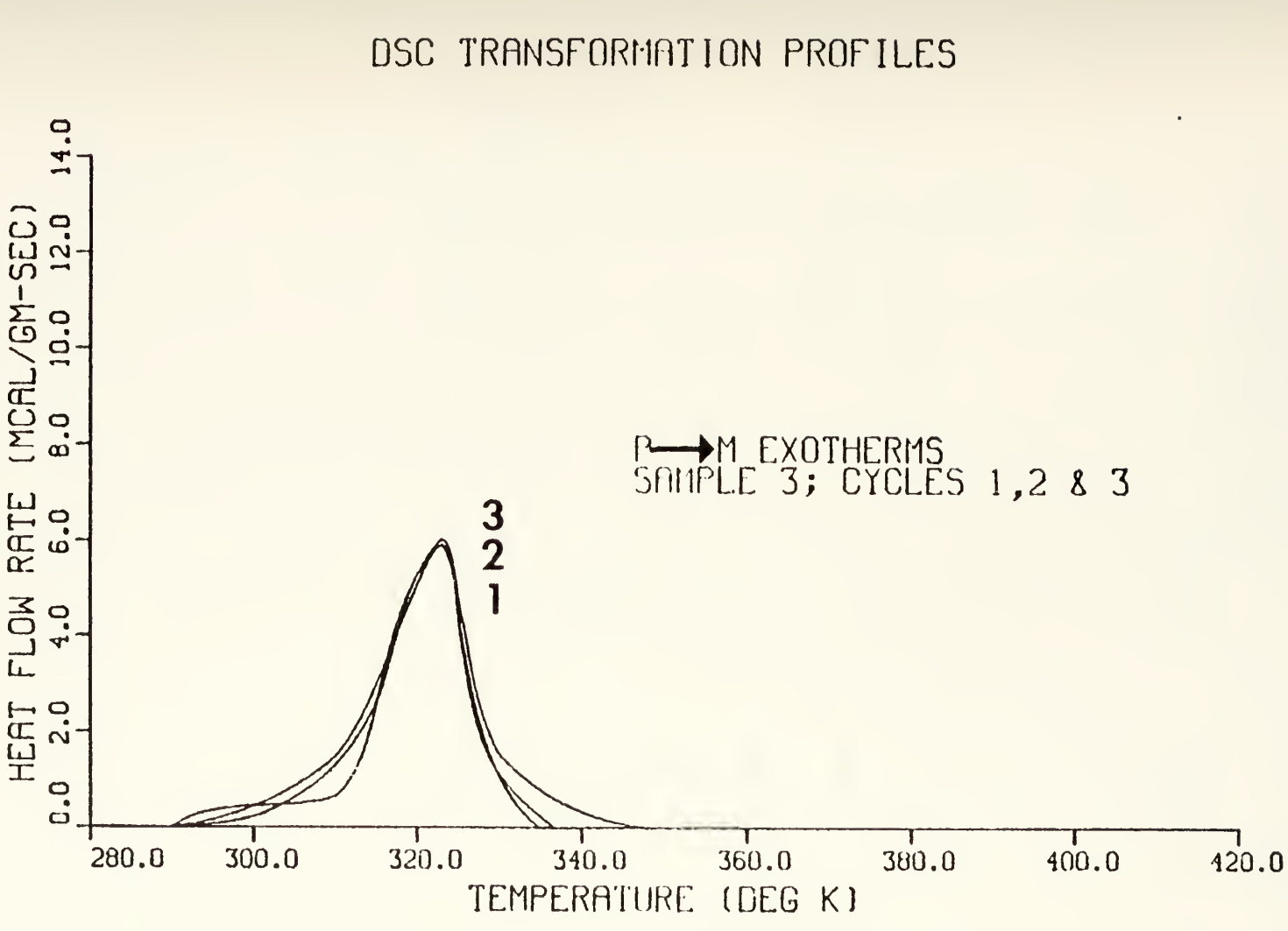

Figure 7. Sample 3, alloy B as received, 2.57% cold work, DSC P⟶M transformation exotherms, cycles 1, 2 and 3.

TABLE IV

Kinetic paramerters for M → P and P → M transformations: sample 3, alloy B as received, 2.57% cold work, cycles 1, 2 and 3.

		Cycle 1	Cycle 2	Cycle 3
M_s	(K)	348.0	335.0	336.9
M_f	(K)	290.2	291.5	292.2
M_{max}	(K)	322.5	322.5	322.5
M_{width}	(K)	12.6	12.3	12.0
M_{height}	(mcal/gm-sec)	5.9	5.9	6.0
M_{area}	(mcal/gm)	551.5	432.7	443.3
A_s	(K)	321.0	305.7	302.0
A_f	(K)	400.2	363.2	349.2
A_{max}	(K)	366.1	333.2	331.9
A_{width}	(K)	28.2	6.6	6.2
A_{height}	(mcal/gm-sec)	2.3	10.4	11.6
A_{area}	(mcal/gm)	424.1	792.6	1018.4

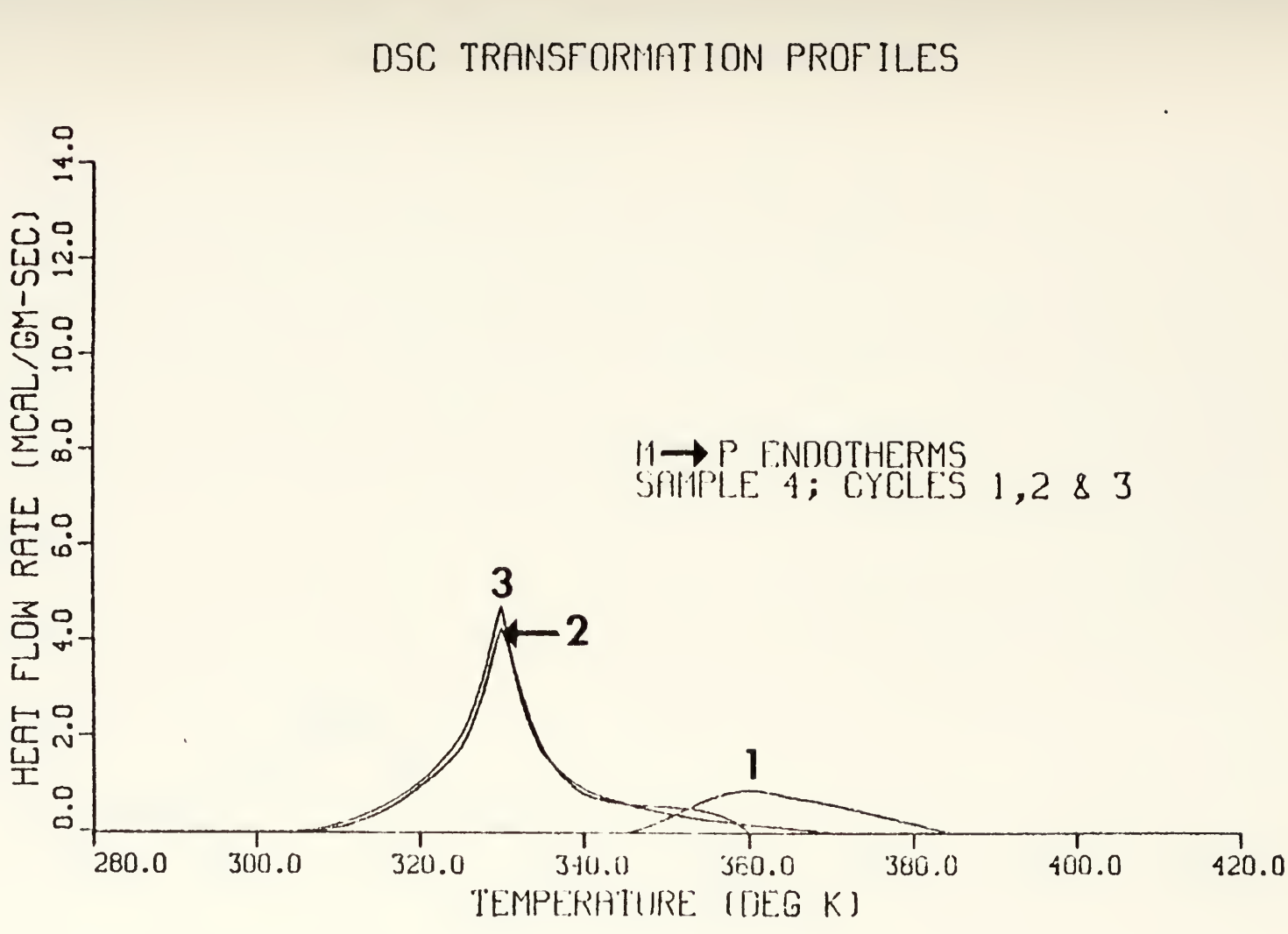

Figure 8. Sample 4, alloy B as received, 4.20% cold work, DSC M→P transformation endotherms, cycles 1, 2 and 3.

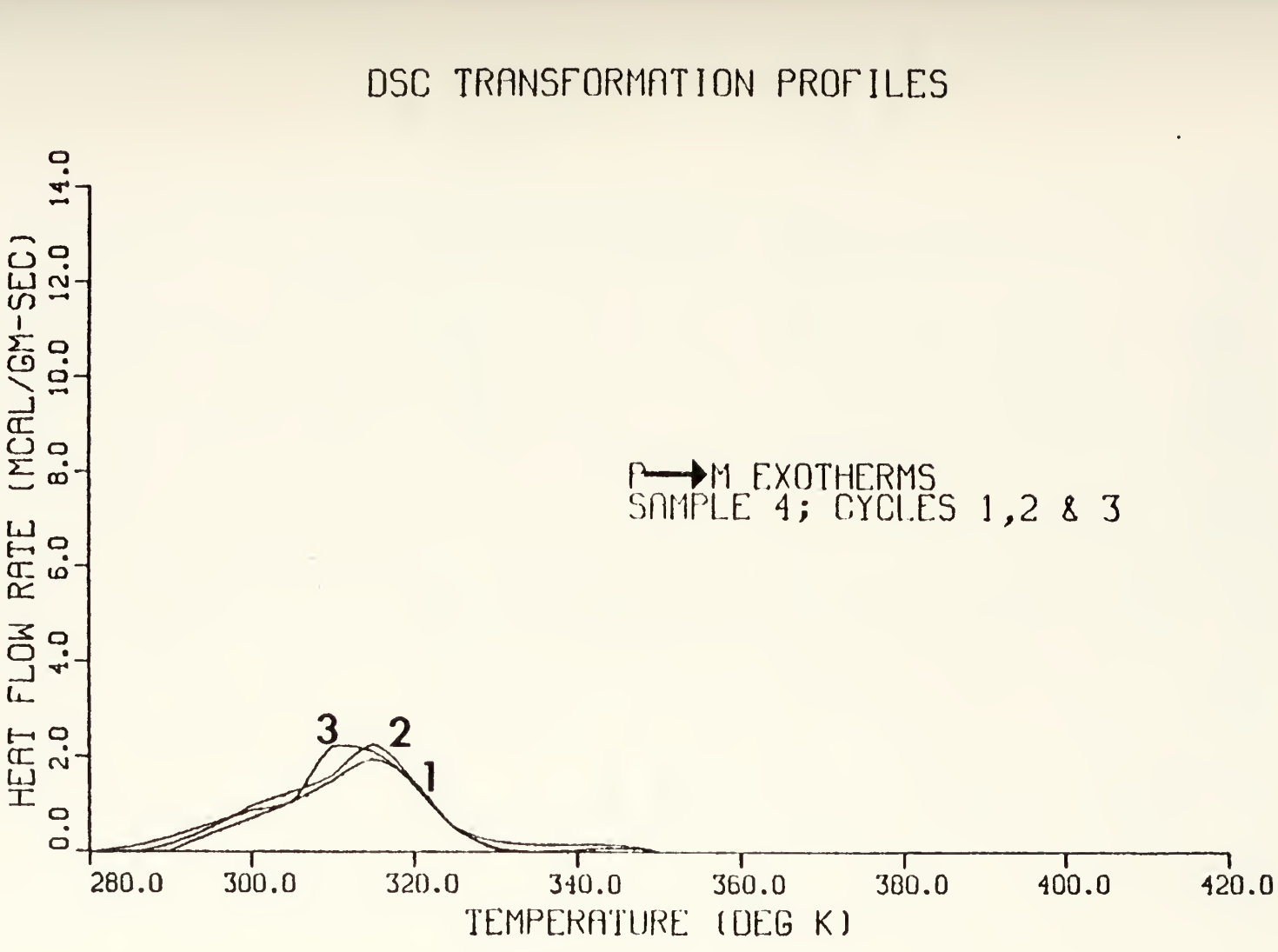

Figure 9. Sample 4, alloy B as received, 4.20% cold work, DSC P ⟶ M transformation exotherms, cycles 1, 2 and 3.

TABLE V

Kinetic parameters for M⟶P and P⟶M transformations: sample 4, alloy B as received, 4.20% cold work, cycles 1, 2 and 3.

		Cycle 1	Cycle 2	Cycle 3
M_s	(K)	330.0	330.0	330.0
M_f	(K)	290.0	287.5	282.0
M_{max}	(K)	314.5	314.5	310.0
M_{width}	(K)	22.4	24.8	25.6
M_{height}	(mcal/gm-sec)	2.0	2.4	2.4
M_{area}	(mcal/gm)	248.7	292.8	304.7
A_s	(K)	345.0	305.0	305.0
A_f	(K)	383.5	360.0	367.5
A_{max}	(K)	360.1	329.6	329.6
A_{width}	(K)	24.0	8.8	9.4
A_{height}	(mcal/gm-sec)	0.9	4.2	4.8
A_{area}	(mcal/gm)	140.6	528.3	576.9

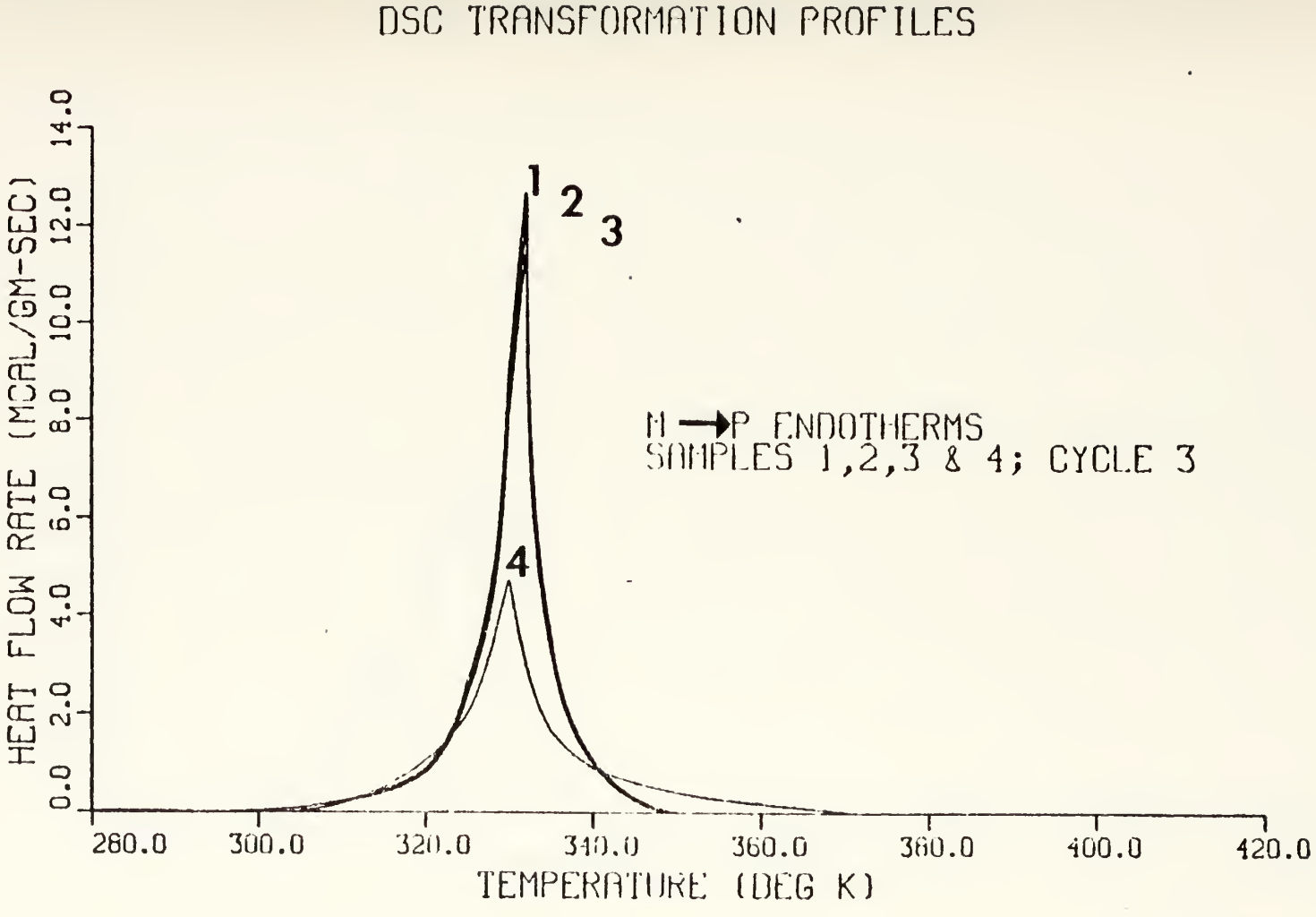

Figure 10. Samples 1, 2, 3 and 4; alloy B as received; 0.00%, 1.09%, 2.57% and 4.20% cold work; DSC M → P transformation endotherms, cycle 3.

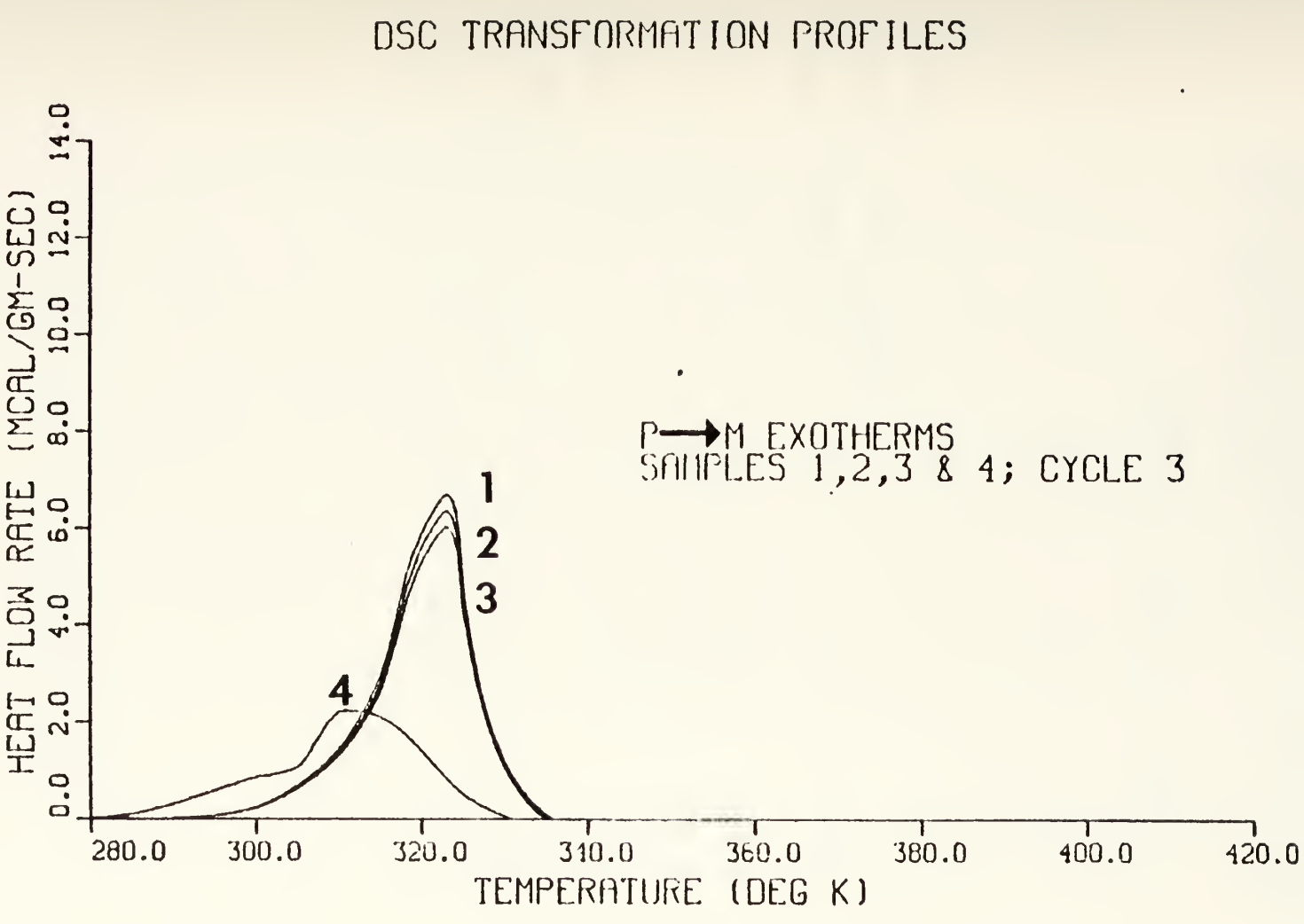

Figure 11. Samples 1, 2, 3 and 4; alloy B as received; 0.00%, 1.09%, 2.57% and 4.20% cold work; DSC P → M transformation exotherms, cycle 3.

TABLE VI

Kinetic parameters for M → P and P → M transformations: samples 1, 2, 3 and 4; alloy B as received; 0.00%, 1.09%, 2.57% and 4.20% cold work; cycle 3.

		Sample 1	Sample 2	Sample 3	Sample 4
M_s	(K)	338.0	338.0	336.9	330.0
M_f	(K)	292.0	292.0	292.0	282.0
M_{max}	(K)	322.5	322.5	322.5	310.0
M_{width}	(K)	12.0	12.0	12.0	25.6
M_{height}	(mcal/gm-sec)	6.7	6.3	6.0	2.4
M_{area}	(mcal/gm)	492.3	470.5	443.3	304.7
A_s	(K)	303.0	300.0	302.9	305.0
A_f	(K)	349.5	348.5	349.2	367.5
A_{max}	(K)	331.0	331.0	331.9	329.6
A_{width}	(K)	6.0	6.2	6.2	9.4
A_{height}	(mcal/gm-sec)	12.9	12.3	11.6	4.8
A_{area}	(mcal/gm)	1132.3	1075.9	1018.4	576.9

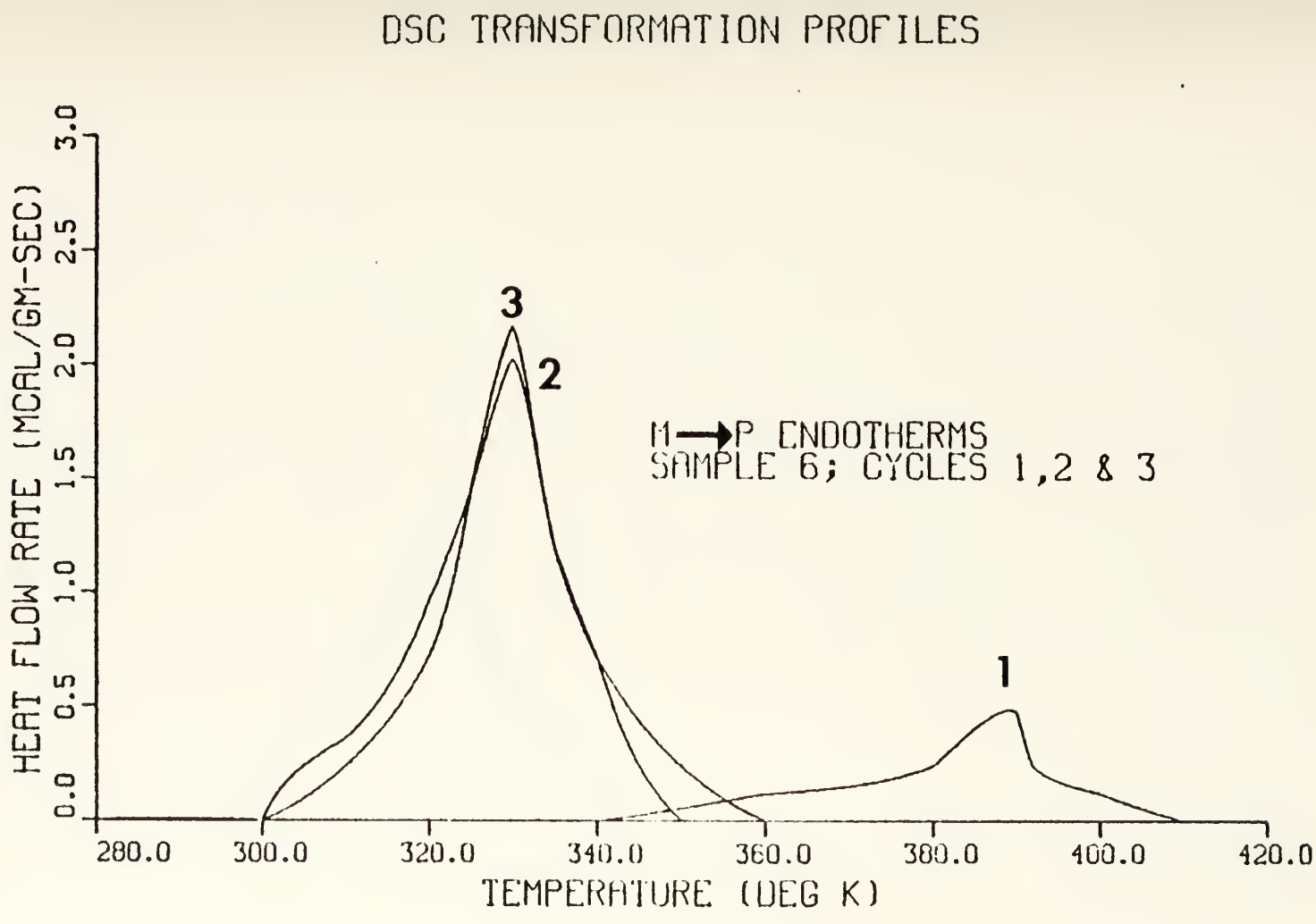

Figure 12. Sample 6, alloy B annealed and quenched, 0.00% cold work, DSC M→P transformation endotherms, cycles 1, 2 and 3.

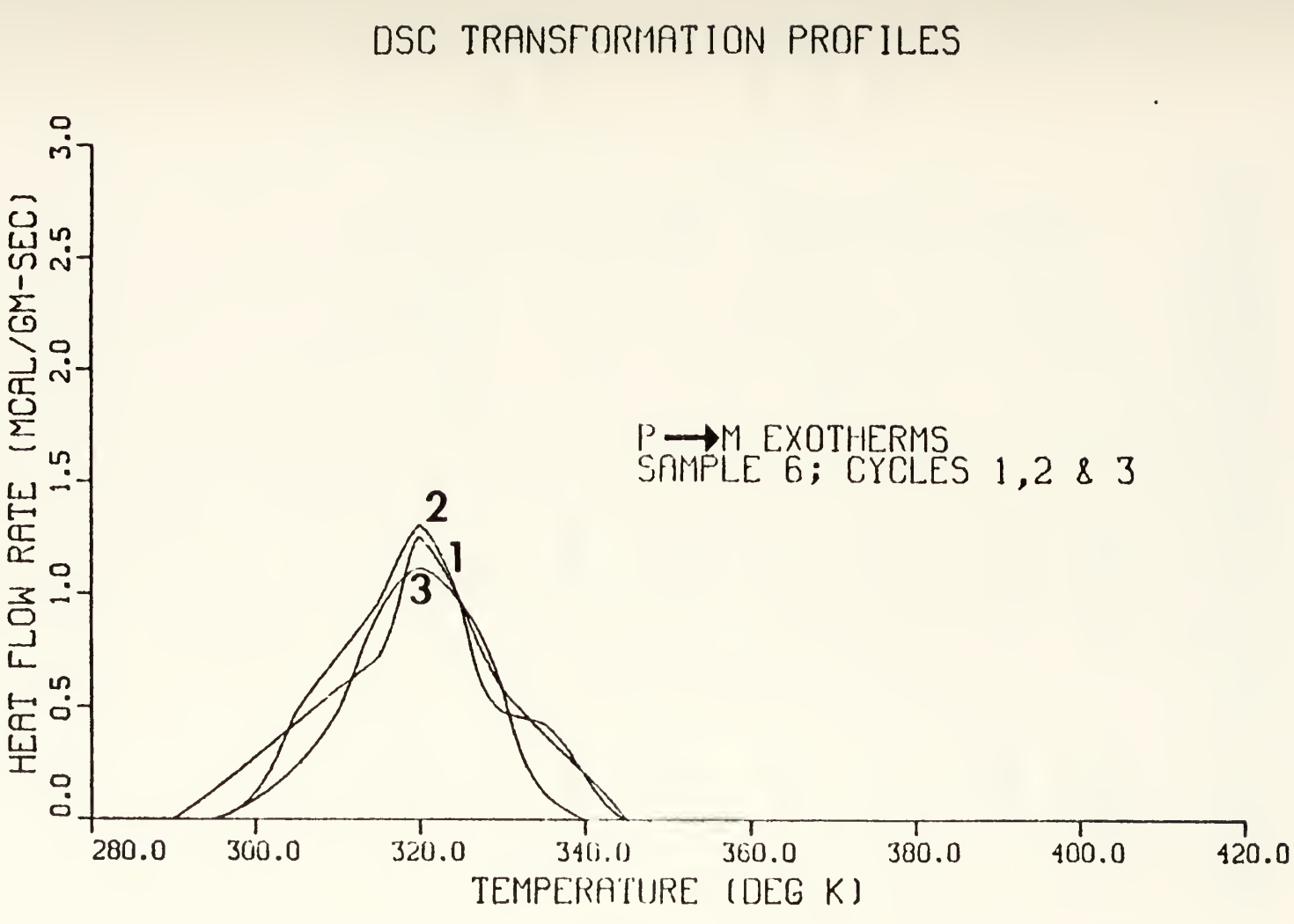

Figure 13. Sample 6, alloy B annealed and quenched, 0.00% cold work, DSC P→M transformation exotherms, cycles 1, 2 and 3.

TABLE VII

Kinetic parameters for M → P and P → M transformations: sample 6, alloy B annealed and quenched, 0.00% cold work, cycles 1, 2 and 3.

		Cycle 1	Cycle 2	Cycle 3
M_s	(K)	340.0	344.5	340.0
M_f	(K)	296.2	290.0	296.2
M_{max}	(K)	320.0	320.0	320.0
M_{width}	(K)	24.0	19.0	17.6
M_{height}	(mcal/gm-sec)	1.1	1.2	1.3
M_{area}	(mcal/gm)	152.7	160.2	172.0
A_s	(K)	341.5	300.0	300.0
A_f	(K)	410.0	360.0	350.0
A_{max}	(K)	389.0	328.5	328.5
A_{width}	(K)	16.8	14.4	13.6
A_{height}	(mcal/gm-sec)	0.5	2.0	2.2
A_{area}	(mcal/gm)	92.9	300.0	284.3

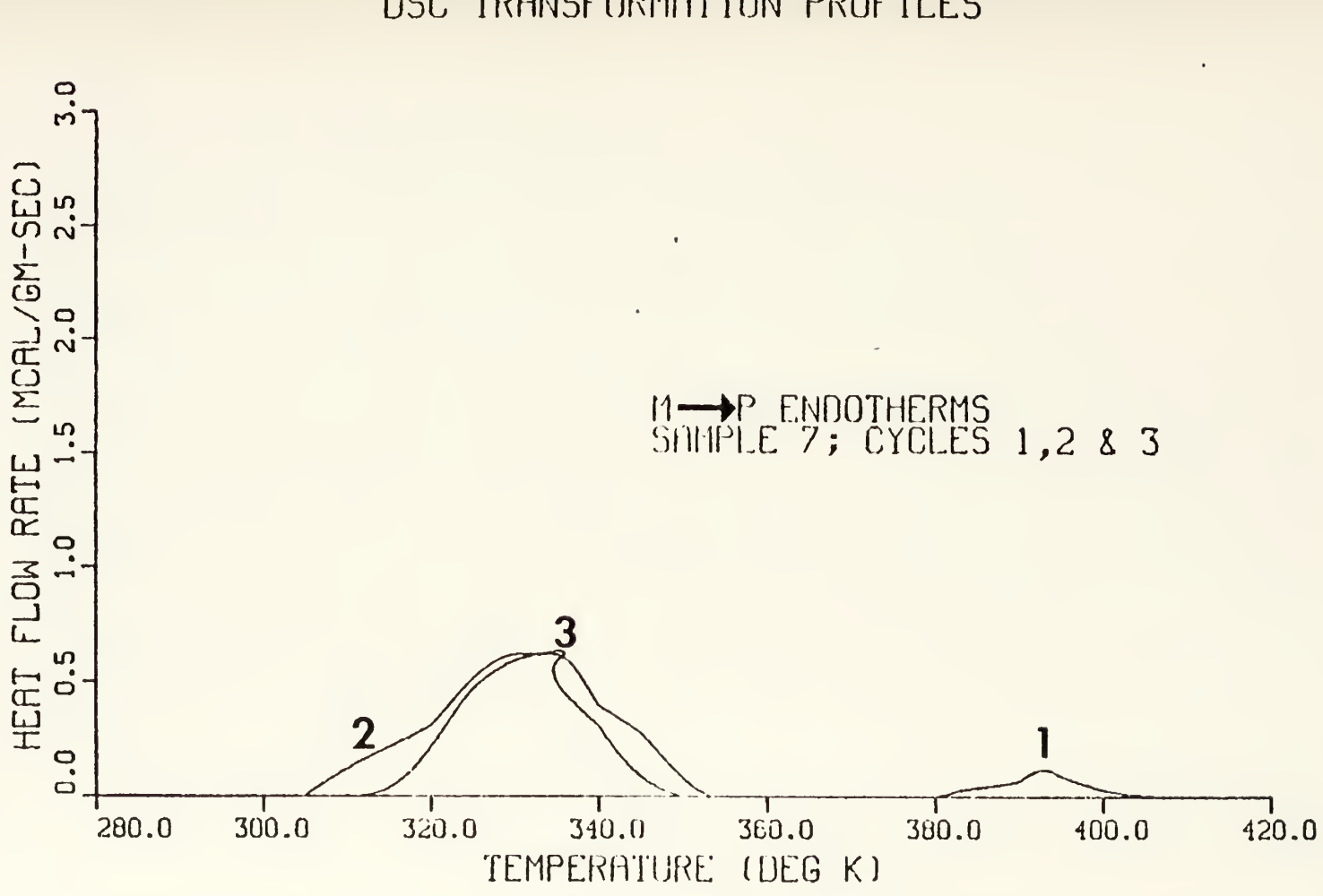

Figure 14. Sample 7, alloy B annealed and quenched, 4.20% cold work, DSC M⟶P transformation endotherms, cycles 1, 2 and 3.

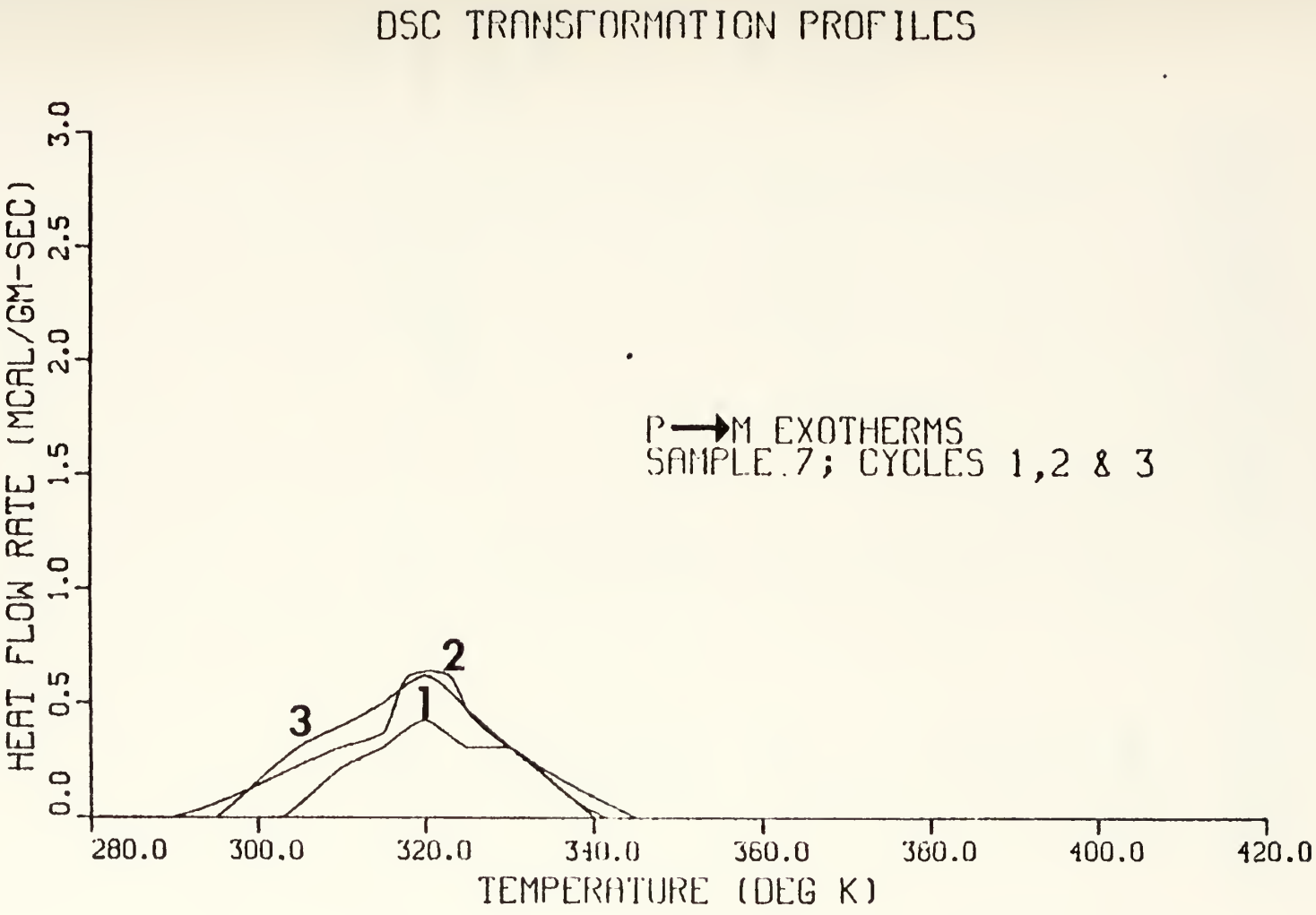

Figure 15. Sample 7, alloy B annealed and quenched, 4.20% cold work, DSC P⟶M transformation exotherms, cycles 1, 2 and 3.

TABLE VIII

Kinetic parameters for M → P and P → M transformations: sample 7, alloy B annealed and quenched, 4.20% cold work, cycles 1, 2 and 3.

		Cycle 1	Cycle 2	Cycle 3
M_s	(K)	340.0	344.5	340.0
M_f	(K)	302.5	290.0	295.0
M_{max}	(K)	320.0	320.0	320.0
M_{width}	(K)	27.2	27.0	25.6
M_{height}	(mcal/gm-sec)	0.4	0.6	0.6
M_{area}	(mcal/gm)	107.8	123.7	131.2
A_s	(K)	380.0	304.5	310.5
A_f	(K)	405.0	353.5	350.0
A_{max}	(K)	392.0	331.0	332.0
A_{width}	(K)	12.0	24.0	18.4
A_{height}	(mcal/gm-sec)	0.1	0.7	0.7
A_{area}	(mcal/gm)	11.7	121.6	103.4

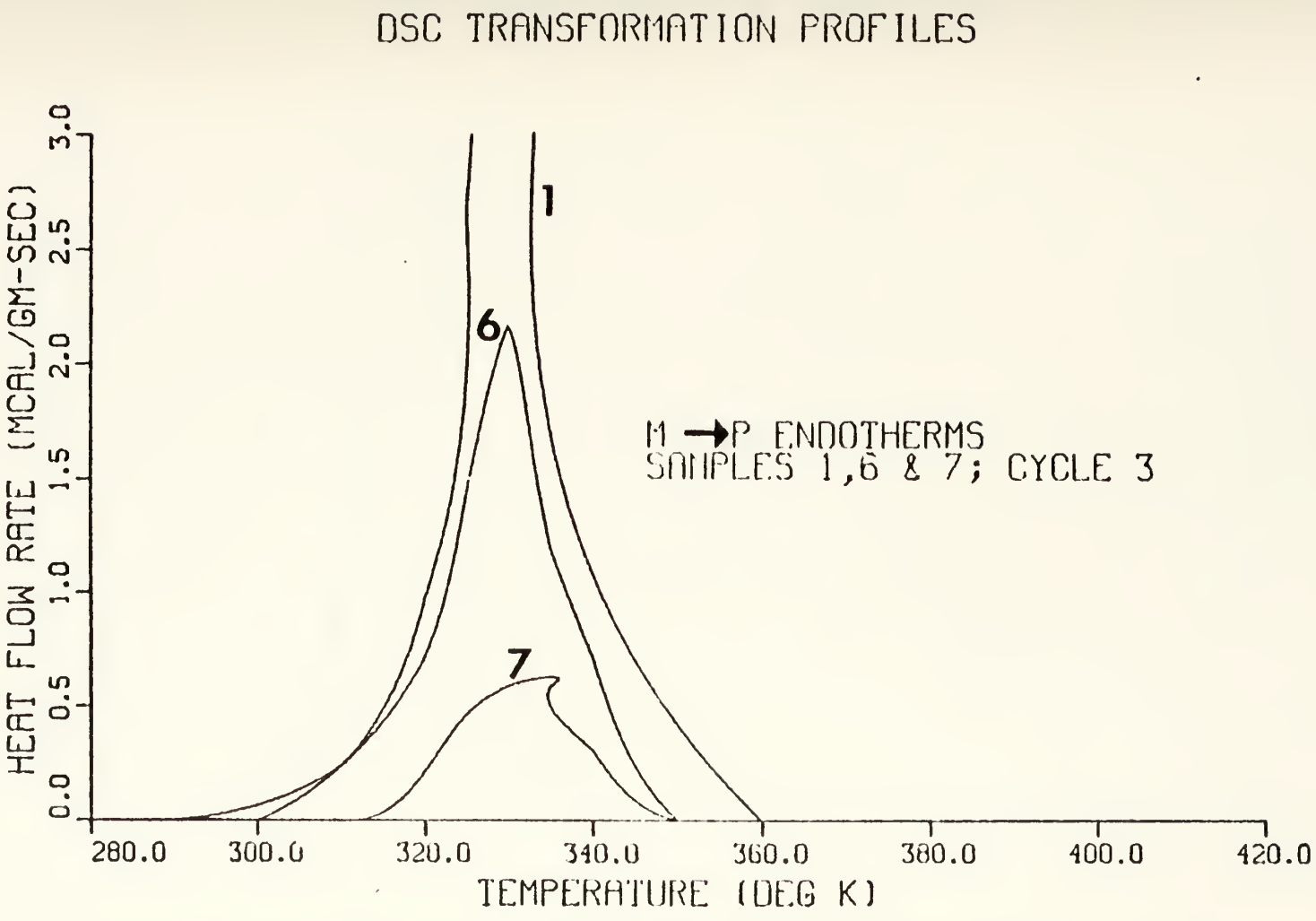

Figure 16. Samples 1, 6 and 7; alloy B as received 0.00%, cold work, alloy B annealed and quenched 0.00% cold work, alloy B annealed and quenched 4.20% cold work; DSC M⟶P transformation endotherms, cycle 3.

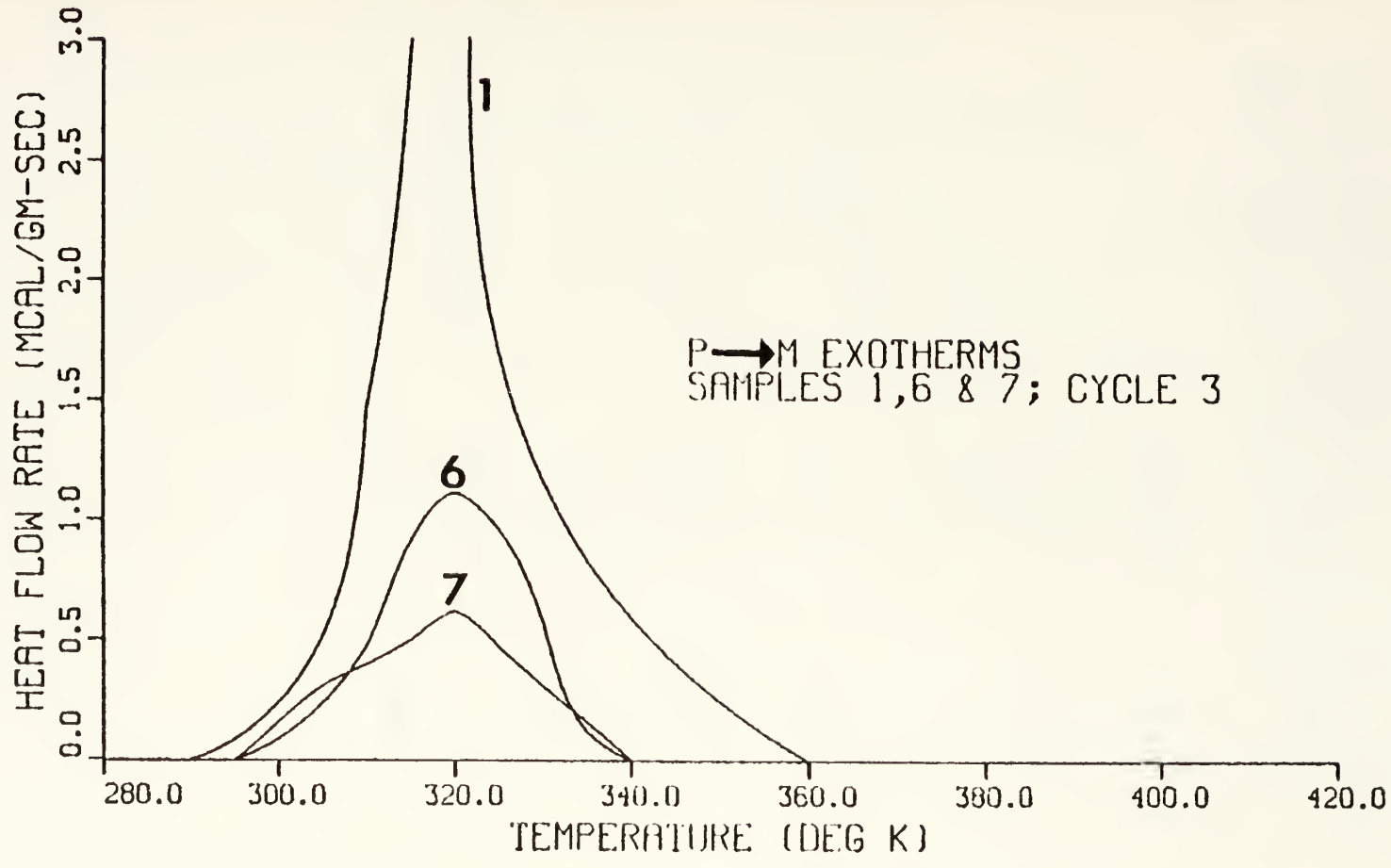

Figure 17. Samples 1, 6 and 7; alloy B as received 0.00% cold work, alloy B annealed and quenched 0.00% cold work, alloy B annealed and quenched 4.20% cold work; DSC P⟶M transformation exotherms, cycle 3.

TABLE IX

Kinetic parameters for M $\rightarrow$ P and P $\rightarrow$ M transformations: samples 1, 6 and 7; alloy B as received 0.00% cold work, alloy B annealed and quenched 0.00% cold work, alloy B annealed and quenched 4.20% cold work; cycle 3.

		Sample 1	Sample 2	Sample 3
M_s	(K)	338.0	340.0	340.0
M_f	(K)	292.0	296.2	295.0
M_{max}	(K)	322.5	320.0	320.0
M_{width}	(K)	12.0	17.6	25.6
M_{height}	(mcal/gm-sec)	6.7	1.3	0.6
M_{area}	(mcal/gm)	492.3	172.0	131.2
A_s	(K)	303.0	300.0	310.5
A_f	(K)	349.5	350.0	350.0
A_{max}	(K)	331.0	328.5	332.0
A_{width}	(K)	6.0	13.6	18.4
A_{height}	(mcal/gm-sec)	12.9	2.2	0.7
A_{area}	(mcal/gm)	1132.3	284.3	103.4

Table IX), demonstrate that the annealing and quenching process had an enormous impact on the M$\rightarrow$P and P$\rightarrow$M transformation process. Every kinetic parameter measured differed between the two samples. Most notable was the significant depression of A_{max}, M_{max}, A_{area} and M_{area} for the annealed and quenched alloy.

D. TRANSMISSION ELECTRON MICROSCOPY

The order of presentation of TEM images and SAD patterns follows: 1.) Micrographs 5-11 are representative of the structures prevailing in the as received and as homogenized alloys, 2.) Micrographs 12-21 characterize the stress induced morphology of heavily deformed (4.20% and 12.30% cold work) as received alloy B, and 3.) Micrographs 22-24 illustrate structural conditions associated with thermally cycled, as homogenized alloy B.

1.) Micrographs 5-11 illustrate the overall structural conditions prevailing in as received and as homogenized alloy B. Micrograph 5 depicts the alternating plate morphology typically observed in as homogenized alloy B TEM specimens. Each plate corresponds to a unique martensite variant. The parallel striations within individual plates correspond to stacking faults. Also, the impingement junctions between adjacent plates are distinctively straight and regular. Focusing upon the internally striated region within a single plate of the as homogenized alloy, and tilting the specimen, stacking fault fringes with associated

partial dislocations appear as a matrix of shingle-like structures (Micrograph 6). These shingle-like structures are a manifestation of stacking shifts produced during the structural transition from parent to product phase. Micrographs 7a-7d are selected area diffraction (SAD) patterns taken from representative areas of various undeformed, as homogenized and as received foils prepared for TEM examination. The SAD zone patterns are [010] 18R, $[2\bar{1}0]$ 18R, [831] 18R and $[2\bar{3}1]$ 18R respectively. Diffraction conditions producing the SAD patterns with [010] 18R and $[2\bar{1}0]$ 18R zone axis are common to both 18R and 9R martensites. However, the appearance of superlattice spots in the [831] 18R and $[2\bar{3}1]$ 18R zone patterns can reasonably be explained by assuming an 18R structure.

Micrograph 8 is a bright field image of as homogenized alloy B. The wormwood-like structures appearing within the large crystal plate correspond to homogeneously ordered, isotropic regions separated by antiphase boundaries (APBs). Bright field imaging of APBs is a consequence of either the "manybeam dynamical effect" or the so called "ε - fringe contrast" resulting from small additional displacement of the lattice across the fault. Located centrally in Micrograph 8 is an array of aligned partial dislocations. Stacking fault fringes and associated partial dislocations are also observed adjacent to an intervariant boundry. Micrograph 9 corresponds to undeformed, as received alloy B.

The APBs were imaged using a superlattice spot. These antiphase boundries are observed crossing variant interfaces without interruption. The character of APBs observed in the martensitic alloy (Micrograph 9) is inherited from the DO_3 ordered parent and confirms the diffusionless nature of martensitic transformation. The APBs appearing in the as received alloy are identical to those observed in the as homogenized alloy (Micrograph 8) with respect to size and distribution.

The planar structures of Micrograph 10 correspond to the twin-like bands in martensite plates as observed in the optical microscope for the undeformed, as received alloy. Each plate has internal striations and corresponds to a unique martensite variant. Judging from the angles formed between striations at plate junctions these internally banded plates are presumed to form A/D variant/variant pairs. Micrograph 11a shows a 2H martensite structure found in the as received alloy. A SAD pattern was taken from the region indicated on the lower plate. The SAD (Micrograph 11b) with [010] 2H zone axis, clearly identifies the structure as 2H martensite. In general, the configuration of variants and crystallographic structure of both the as received and as homogenized alloy were the same, except for the existance of 2H martensite in the as received alloy. The origin is not clear, but is probably related to the hot working applied during forming of the as received alloy.

2.) Micrographs 12-21 illustrate the morphology of deformed, as received alloy B. Micrographs 12-17c are associated with the 4.20% cold worked alloy and Micrographs 18-21 correspond to the 12.30% cold worked alloy.

The morphology of the deformed (4.20% cold work) as received alloy is complicated. Micrograph 12 corresponds to the region where deformation of martensites has extensively taken place. The intervariant boundaries are noticeably deformed giving a wavy and contorted appearance to the overall structure. The contrast and thickened appearance of variant boundaries, suggests that structural irregularities may be concentrated in the locality of plate boundaries. The large deformed plates exhibit a banded substructure. Also, dislocation contrast can be distinguished within the internally striated deformed plates.

Narrow spear-like structures are observed penetrating the large plates. These spear-like structures also exhibit deformed boundaries, internal striations and internally banded substructure. The spear-like plate containing the herringbone pattern of crossing martensites has a 2H structure as will be shown later. Such morphology is a consequence of the higher symmetry of 2H structures relative to 18R structures.

Micrograph 13 shows a high magnification of a typical banded region in Micrograph 12, in which dislocation contrast was enhanced by tilting the specimen in the

electron microscope. These dislocations are obviously different from the partial dislocations found in the undeformed alloy (Micrograph 8). The orientation of dislocations appearing in Micrograph 12 is random, with high concentrations of tangled dislocations appearing near the contorted intervariant boundary. Micrograph 14 shows another view of randomly distributed dislocations existing within the banded regions (Micrograph 12) of deformed plates.

In Micrograph 15, the sheared appearance of martensite plates (dark/light bands) is an obvious indication of slip. The orientation of internal striations (parallel for corresponding plates across the slip line) suggests that slip occured on basal planes due to concentrated stress fields. Micrograph 16a, with associated SAD (Micrograph 16b) is a high magnification of a region of crossing martensites (herringbone structures) observed in Micrograph 12. The variant boundaries are clearly distorted, and the twin-like products with crossing orientations observed within the central plate produce collectively the herringbone morphology. The SAD (Micrograph 16b) from an area encompassing a few internal bands, and taken after tilting the specimen, shows two superimposed [010] 2H zone patterns; thus associating the herringbone morphology (Micrograph 16a, selected regions of Micrograph 12) with 2H martensite.

Micrographs 17a-17c correspond to the same specimen (as received alloy B, 4.20% cold work) at different tilt angles.

Although the overall alloy morphology shown in this series of micrographs reflects the structural features already identified with the deformed alloy, the appearance of possible single crystal regions existing within the large central plate is unique. Upon tilting the specimen, no internal striations were observed within these unique structures. The absence of internal striations supports the assumption that these structures correspond to single crystals.

Micrograph 18 is a low magnification bright field image of the general wavy morphology found in heavily deformed (12.30% cold work) as received alloy B. The white forked structures appear to have grown into the surrounding darker matrix. Micrograph 19 is another view of the wavy morphology characteristic of the heavily deformed alloy. These structures are rife with dislocations and twin-like products. Micrograph 20a is a SAD from a region with structure similar to the dark matrix area of the heavily deformed alloy, and Micrograph 20b is a SAD from a region corresponding to the white wavy forked structures (Micrographs 18-19). The SAD patterns could be indexed $[40\bar{1}]$ 18R and $[10\bar{1}]$ 6R respectively; suggesting that the white forked structures (Micrographs 18-19) could have been produced by 18R to 6R martensitic transformation induced by the external stress. Micrograph 21 shows Moire fringes

which are considered to result from large internal stress fields present in the heavily deformed as received alloy.

Briefly summarizing, Micrographs 12-21 illustrated the general structure and highlighted unique features characterizing stress induced morphology of heavily deformed (4.20% and 12.30% cold work) as received alloy B.

3.) Micrographs 22-24 illustrate structural conditions prevailing in undeformed as homogenized alloy B after repeated thermal cycling. After five thermal cycles, some of the variants are ovserved in crossing patterns (Micrograph 22). The generally observed internally striated, plate morphology of as homogenized alloy B is retained in the cycled alloy; however, the mixing and crossing of variants due to cycling has apparently introduced dislocations, especially along intervariant interfaces (Micrograph 23). In summary, no prominent microstructural differences were encountered between as homogenized and cycled specimens. Micrograph 24 corresponds to the undeformed, as homogenized alloy after two hundred and four thermal cycles. The prominent wormwood-like structures are antiphase boundaries. The distribution and size of APBs in the undeformed, as homogenized alloy (Micrograph 8) remains unaltered after two hundred and four thermal cycles (Micrograph 24).

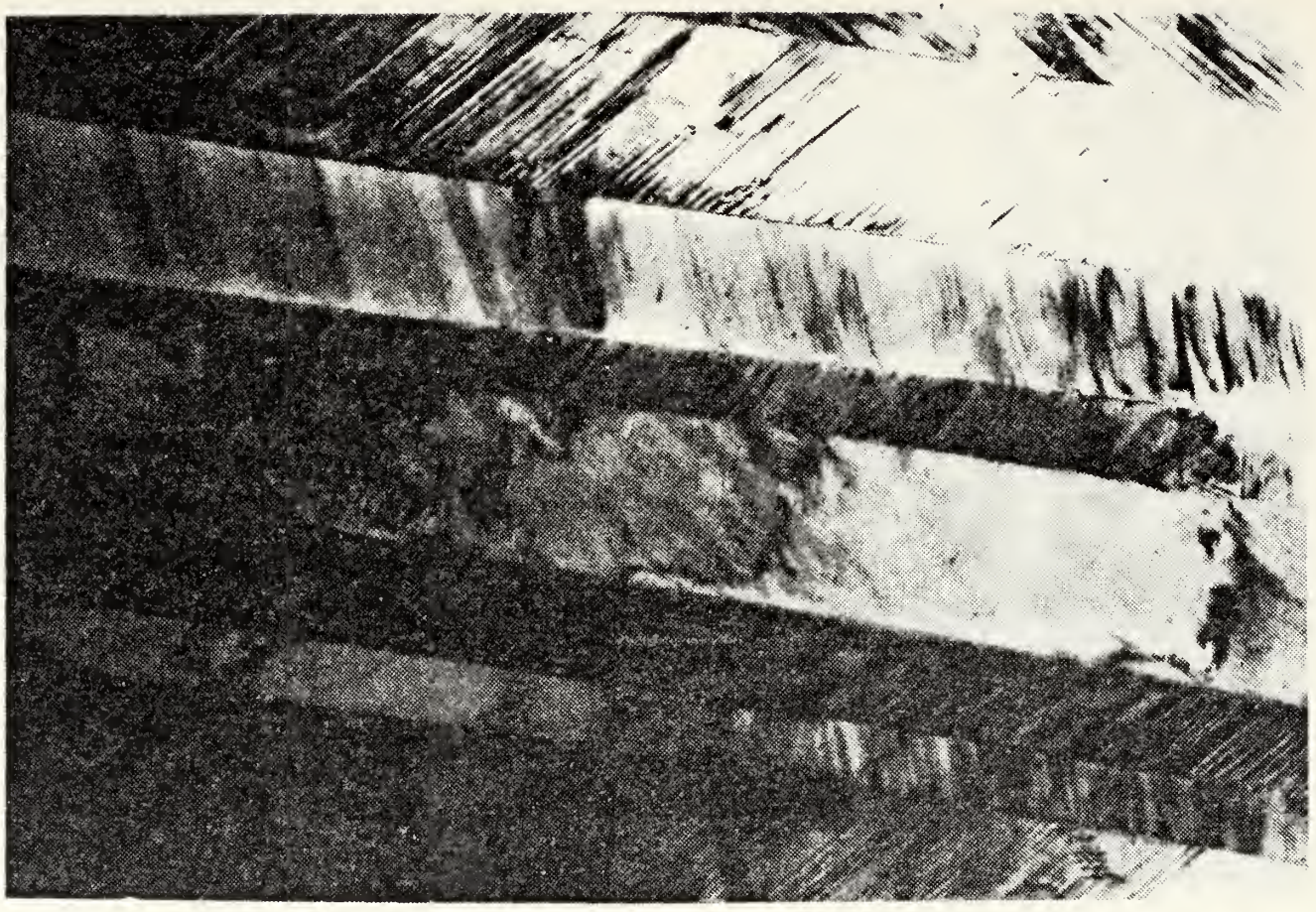

Micrograph 5. Internally striated, alternating plate morphology characteristic of the undeformed, as homogenized alloy. (TEM, 52,000X)

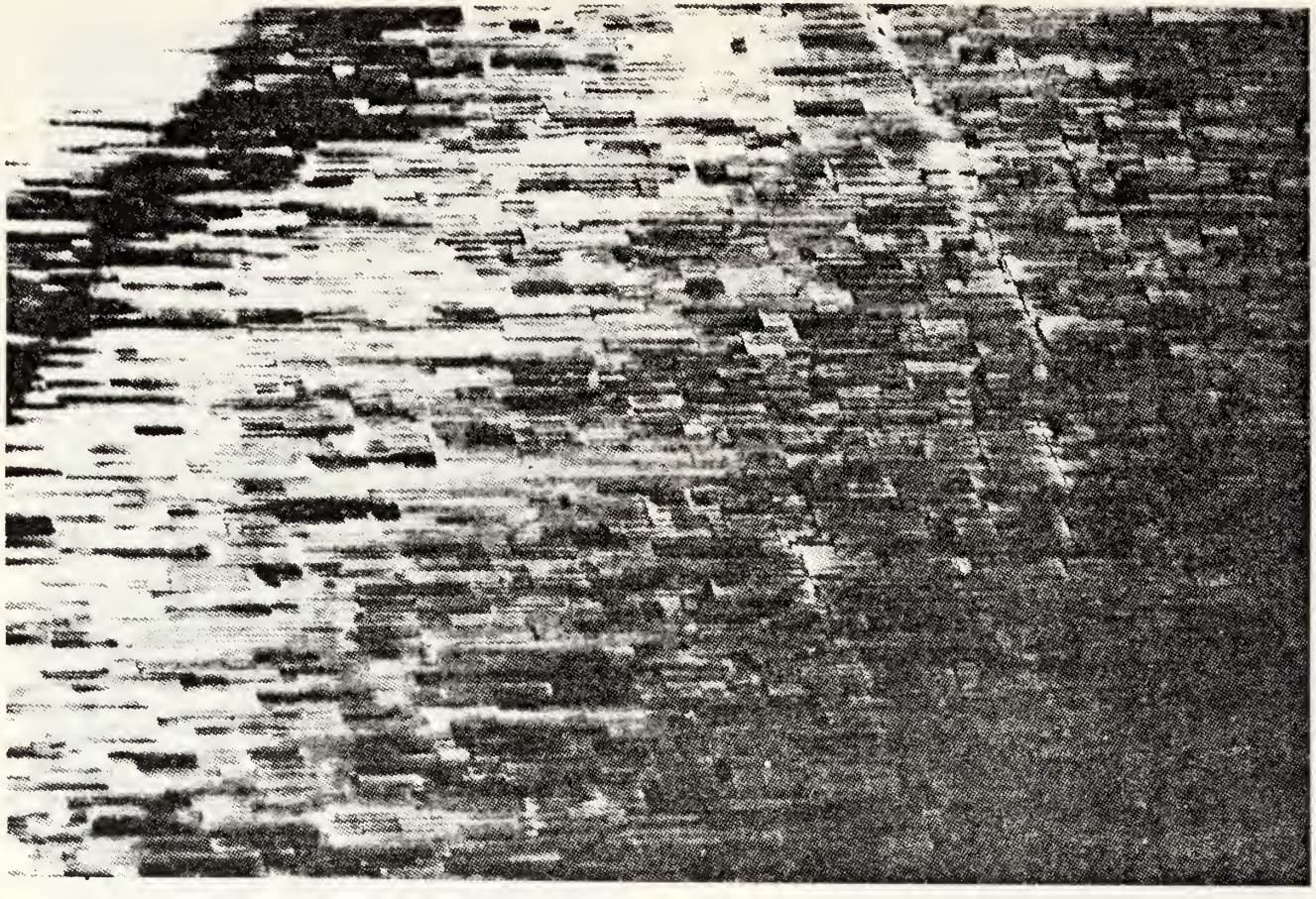

Micrograph 6. As homogenized alloy B. Tilting the TEM specimen reveals a shingle-like matrix which corresponds to stacking faults and partial dislocations. (TEM, 35,640X)

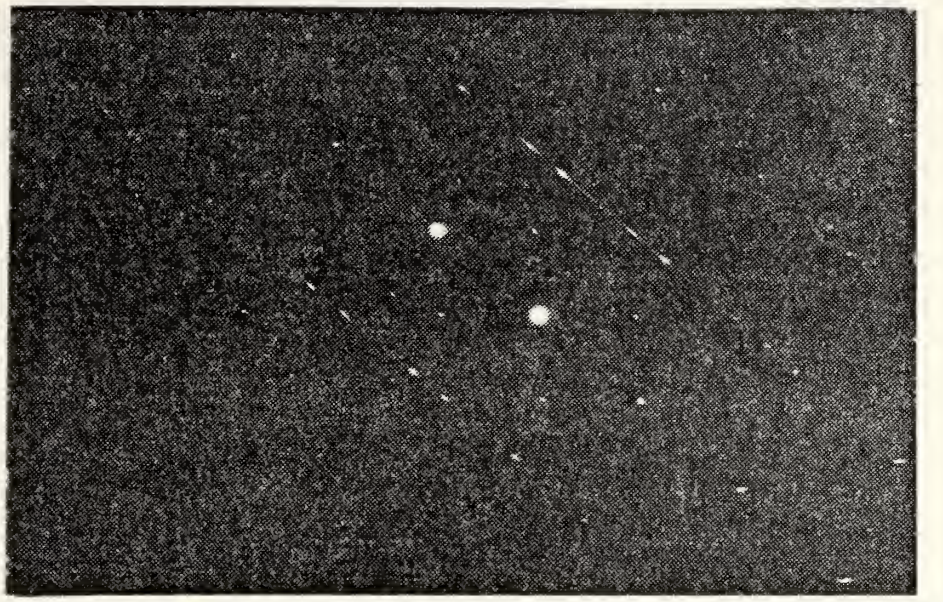

Micrograph 7a. As homogenized alloy B SAD. [010] 18R zone pattern.

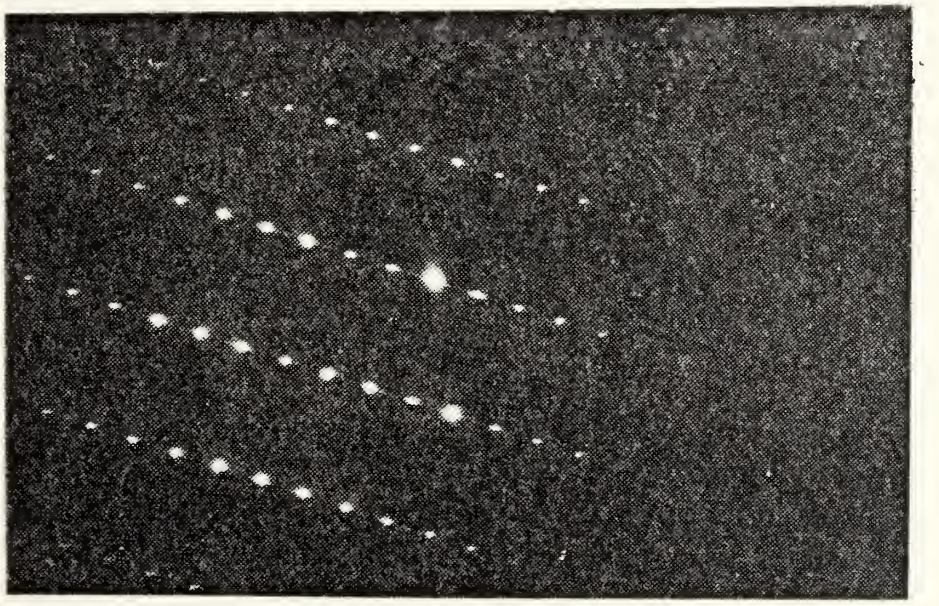

Micrograph 7b. As received alloy B SAD. [$\bar{2}$10] 18R zone pattern.

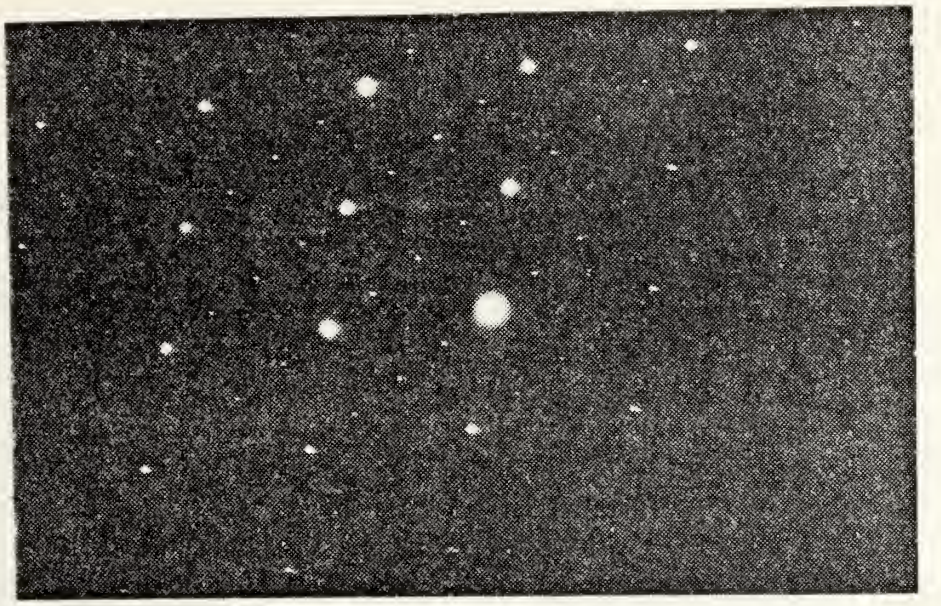

Micrograph 7c. As received alloy B SAD. [831] 18R zone pattern.

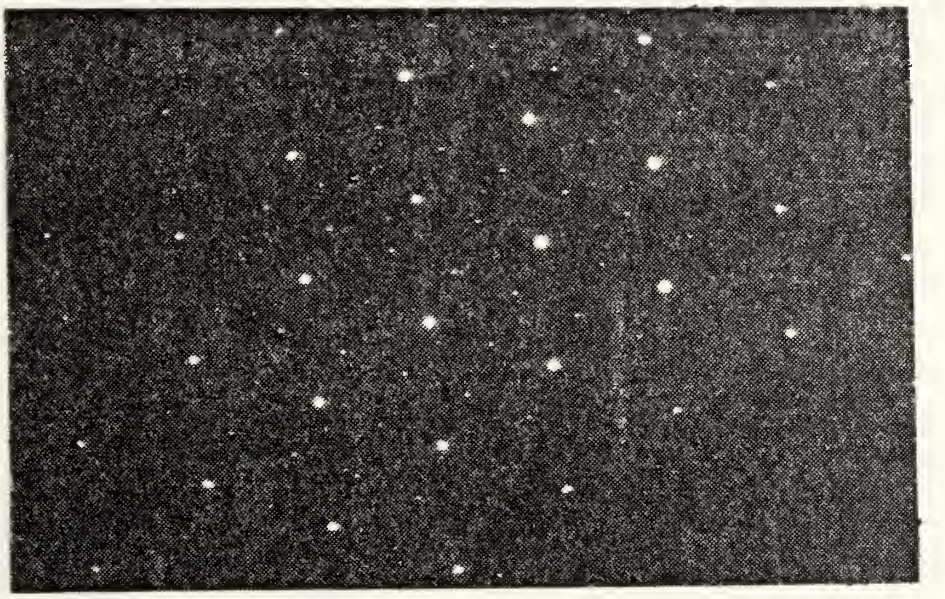

Micrograph 7d. As received alloy B SAD. [$2\bar{3}1$] 18R zone pattern.

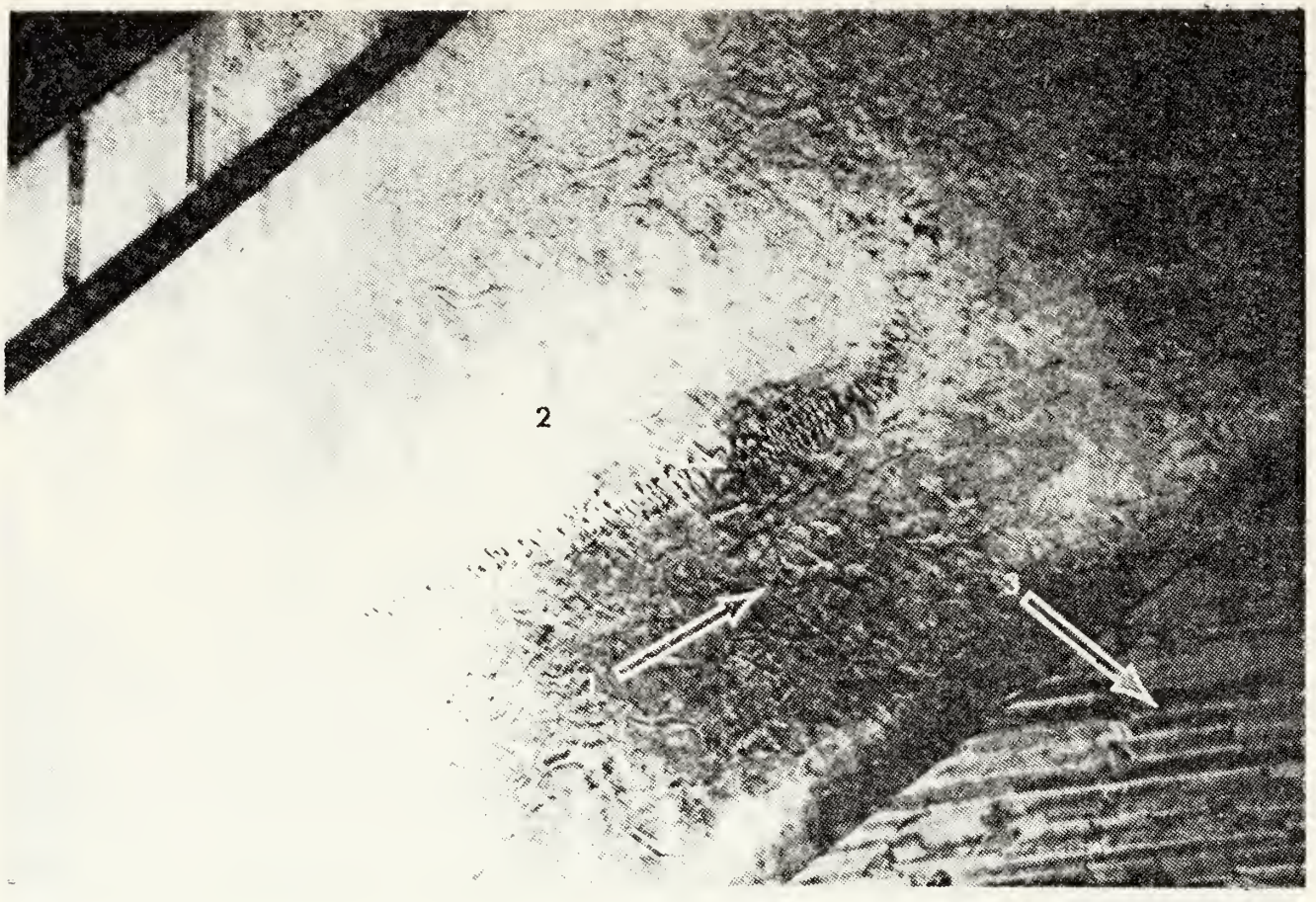

Micrograph 8. As homogenized alloy B. (1) Wormwood-like structures correspond to APBS, (2) partial dislocation array and (3) shingle-like matrix corresponds to stacking faults and partial dislocations. (TEM, 35,640X)

Micrograph 9. As received alloy B. APBs are uninterrupted by martensitic variant boundaries. The character of APBs in the martensite phase is inherited from the DO_3 ordered parent phase. (TEM, 25,000X)

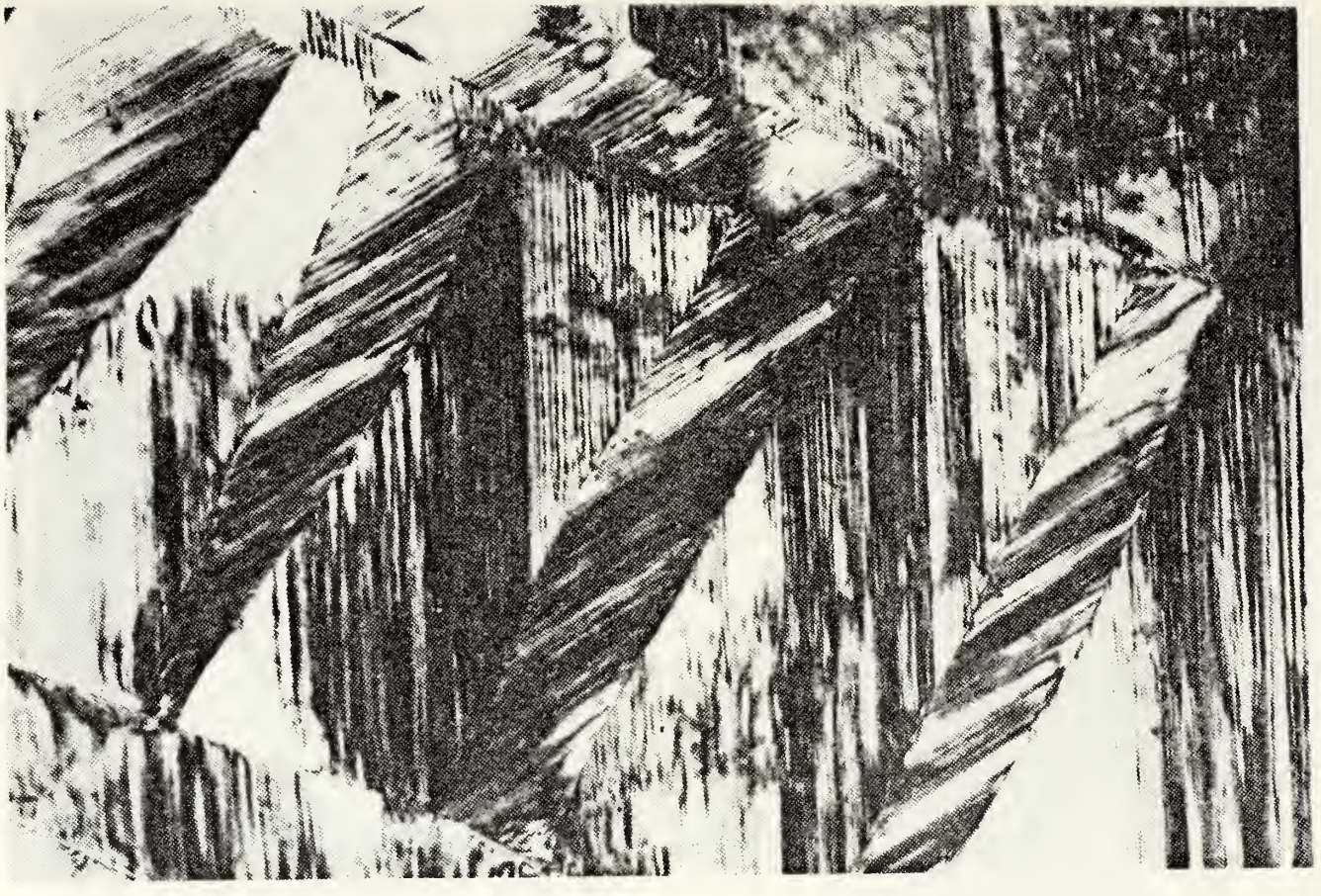

Micrograph 10. As received alloy B. Internally striated plates have formed A/D pairs. (TEM, 47,500X)

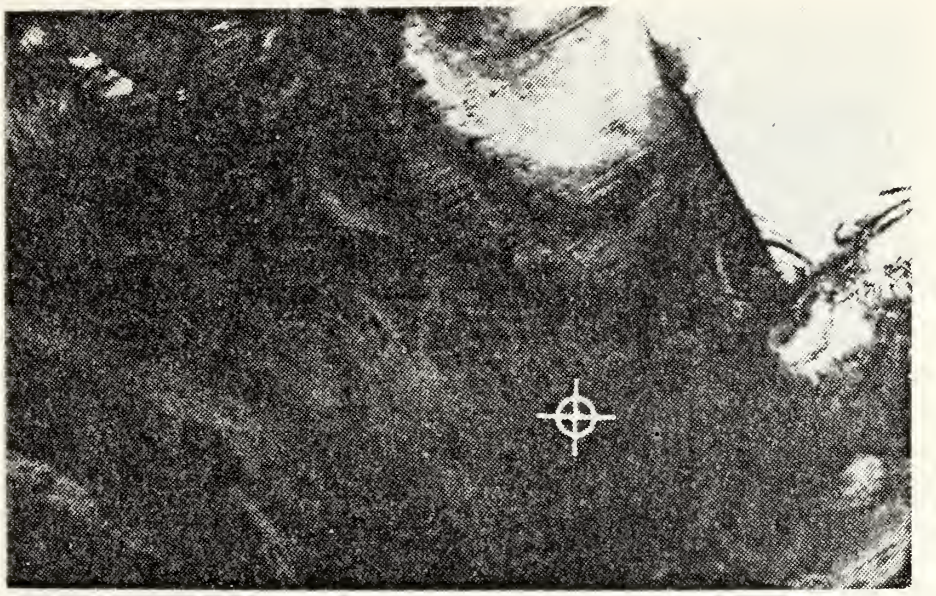

Micrograph 11a. As received alloy B. 2H martensite. Circle delineates region from which SAD was taken (micrograph 11b). (TEM, 39,840X)

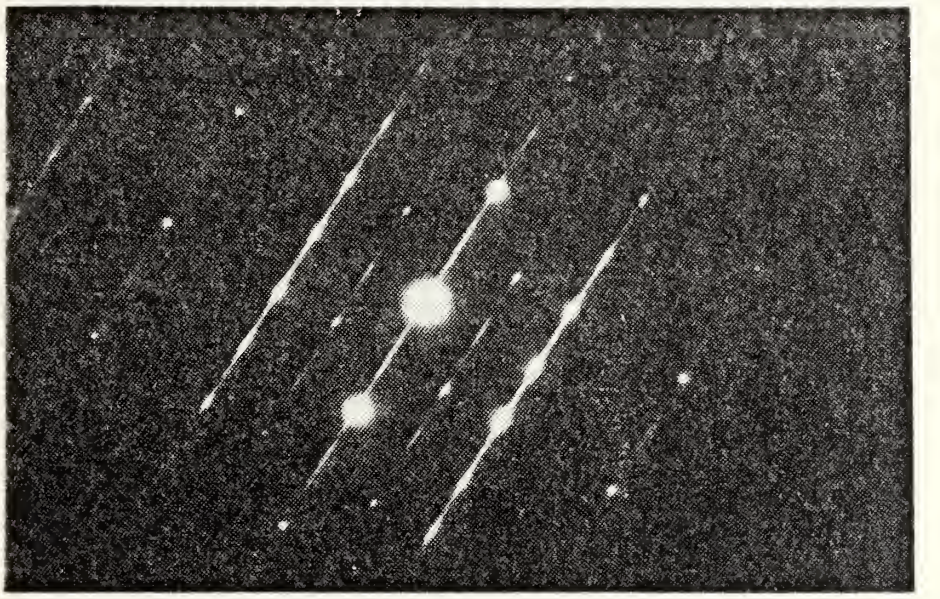

Micrograph 11b. SAD associated with circled region (Micrograph 11a). [010] 2H zone pattern. (TEM, 79,680X)

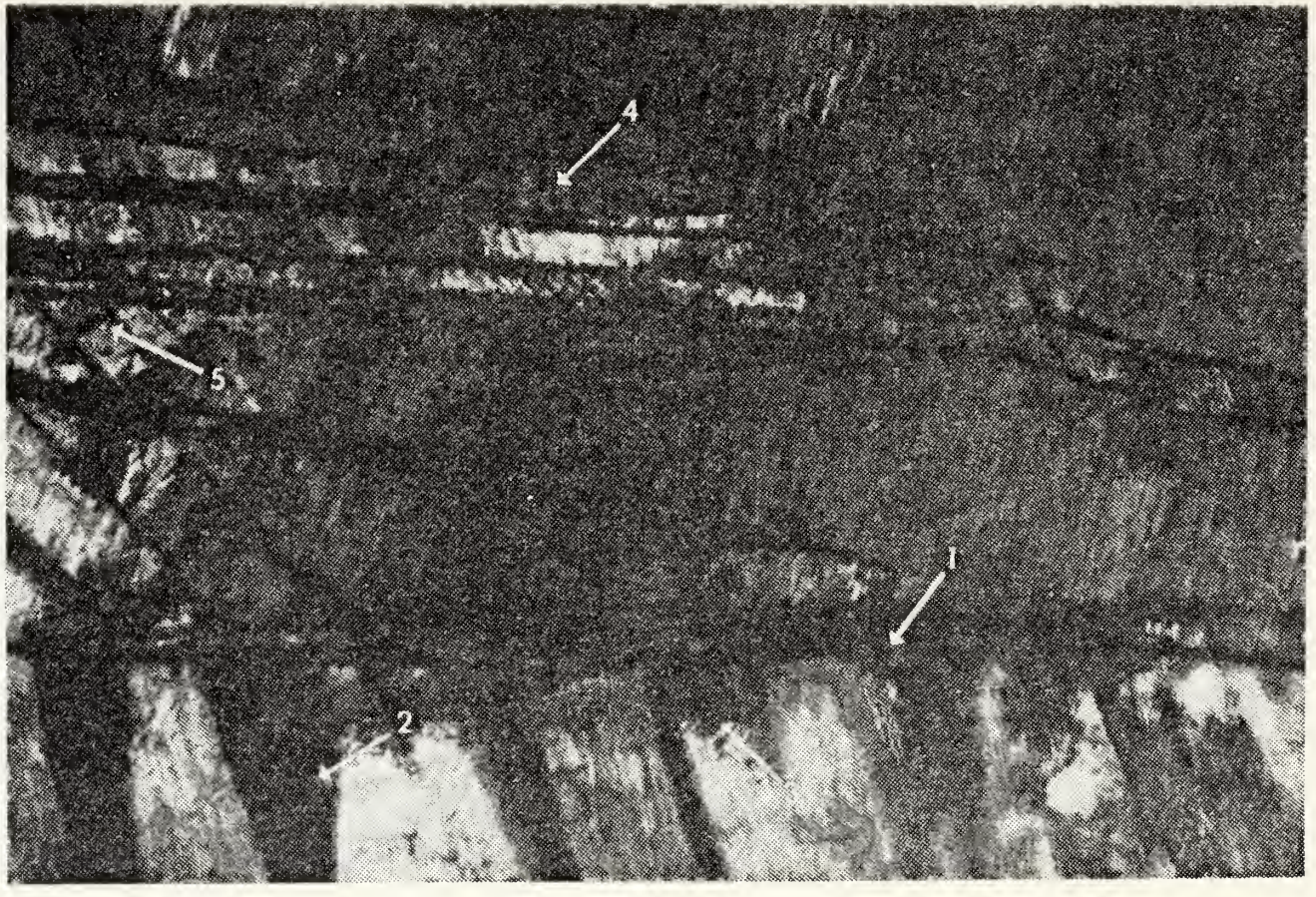

Micrograph 12. As received alloy B (4.20% cold work). (1) Deformed intervariant boundaries, (2) banded substructure, (3) dislocation constrast within banded plates, (4) spear-like structures penetrating the large plates, and (5) herringbone morphology. (TEM, 26,400X)

Micrograph 13. High magnification of typical banded region in the as received (4.20% cold work) alloy (Micrograph 12) showing dislocation tangles concentrated at variant boundaries. (TEM, 66,000X)

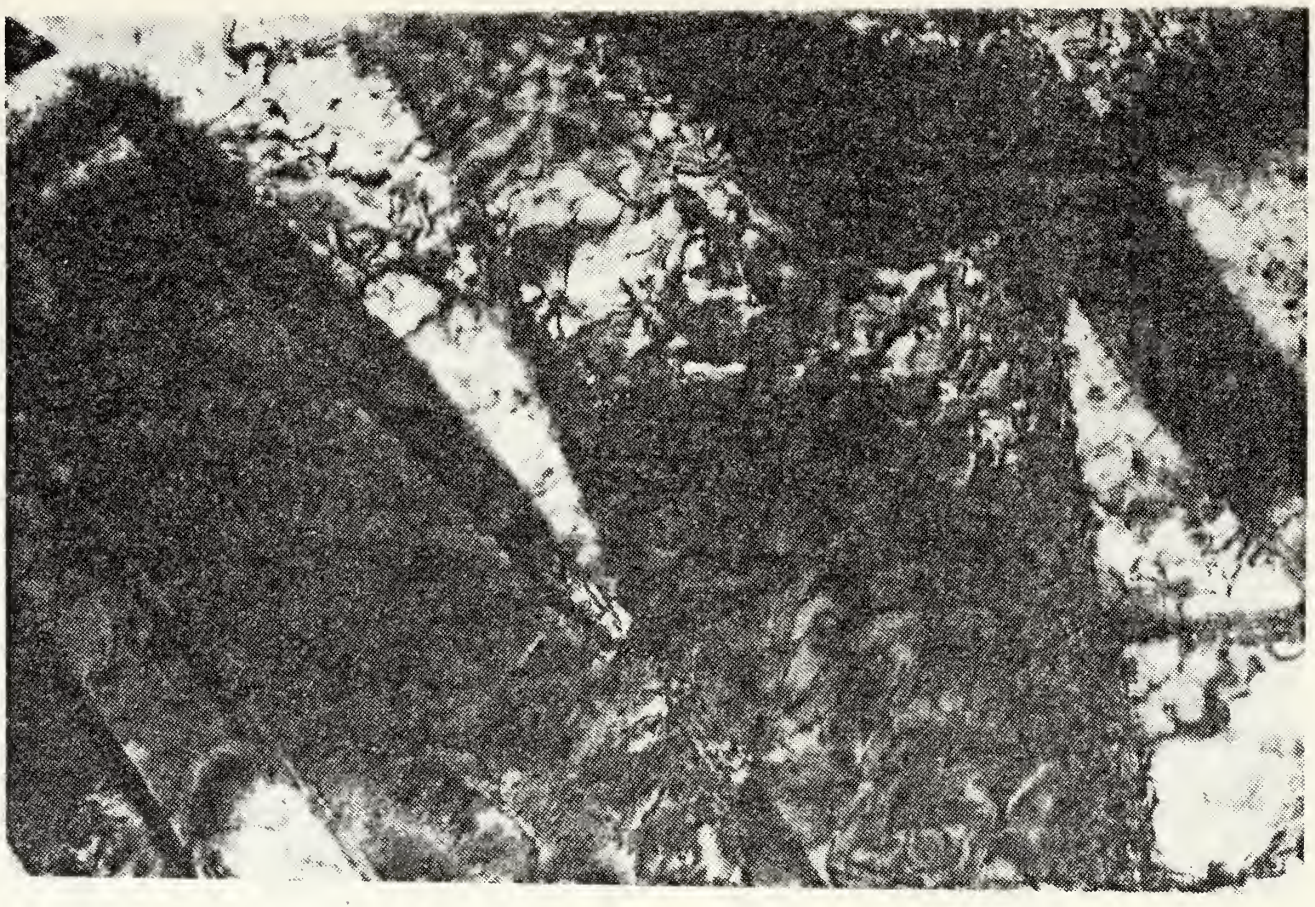

Micrograph 14. As received alloy B. Another view of randomly distributed dislocations located within the internally striated, banded plates of the deformed (4.20% cold work) alloy. (TEM, 66,000X)

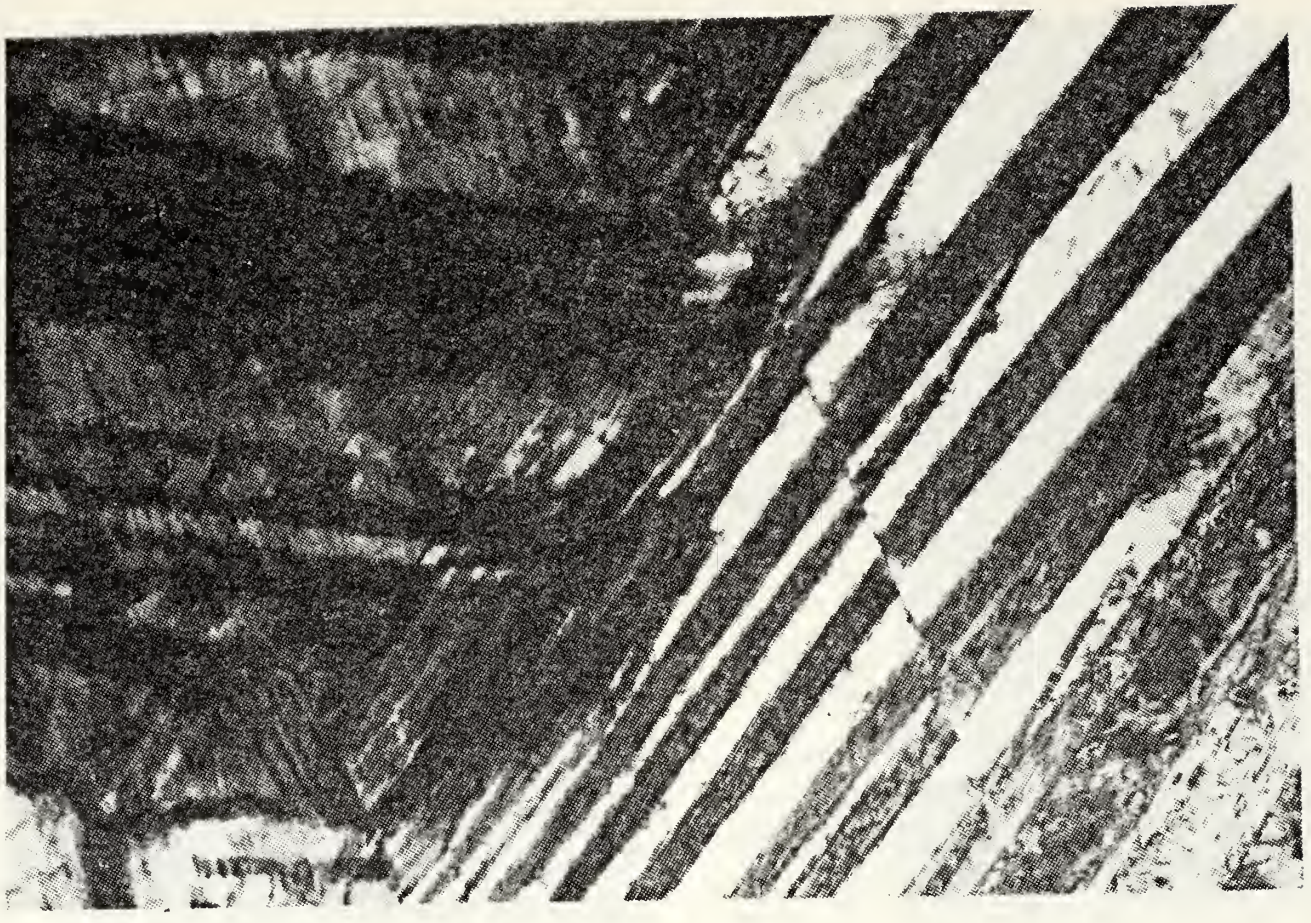

Micrograph 15. Slip has occured on basal planes of the as received alloy (4.20% cold work). (TEM, 26,400X)

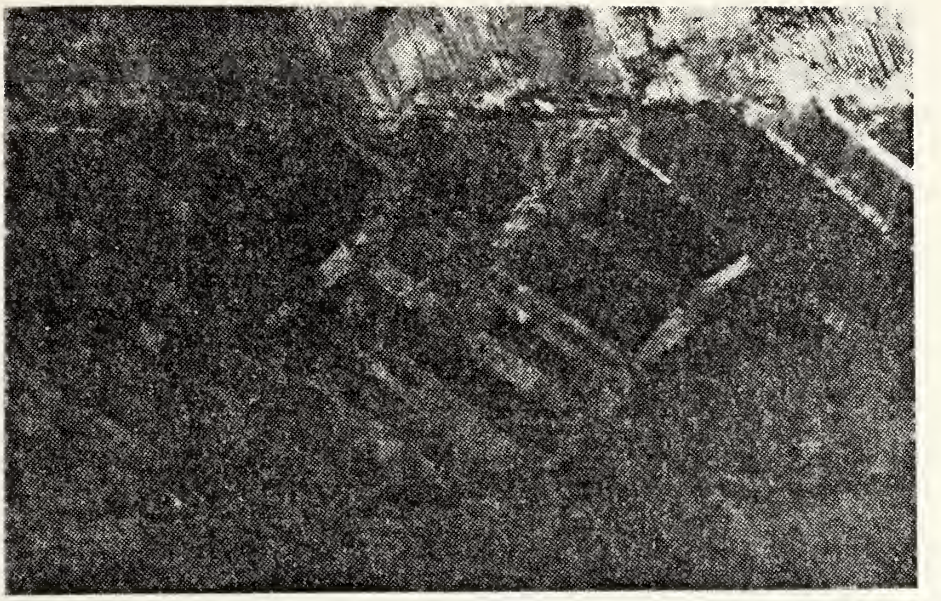

Micrograph 16a. High magnification of herringbone region (Micrograph 12) in the heavily deformed (4.20% cold work), as received alloy. 2H structure confirmed by SAD (Micrograph 16b). (TEM, 22,410X)

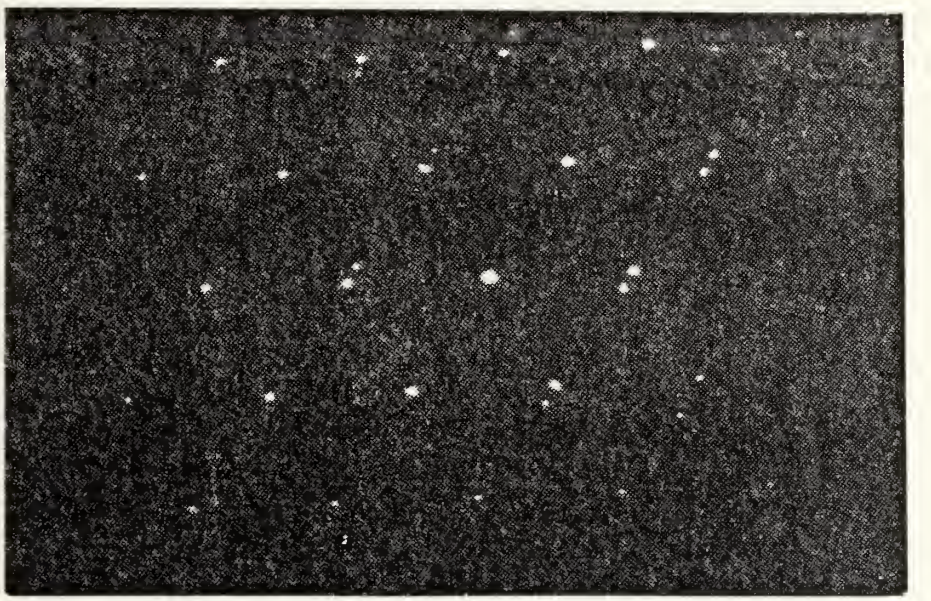

Micrograph 16b. SAD from herringbone region of crossing martensites (Micrograph 16a). [010] 2H zone pattern.

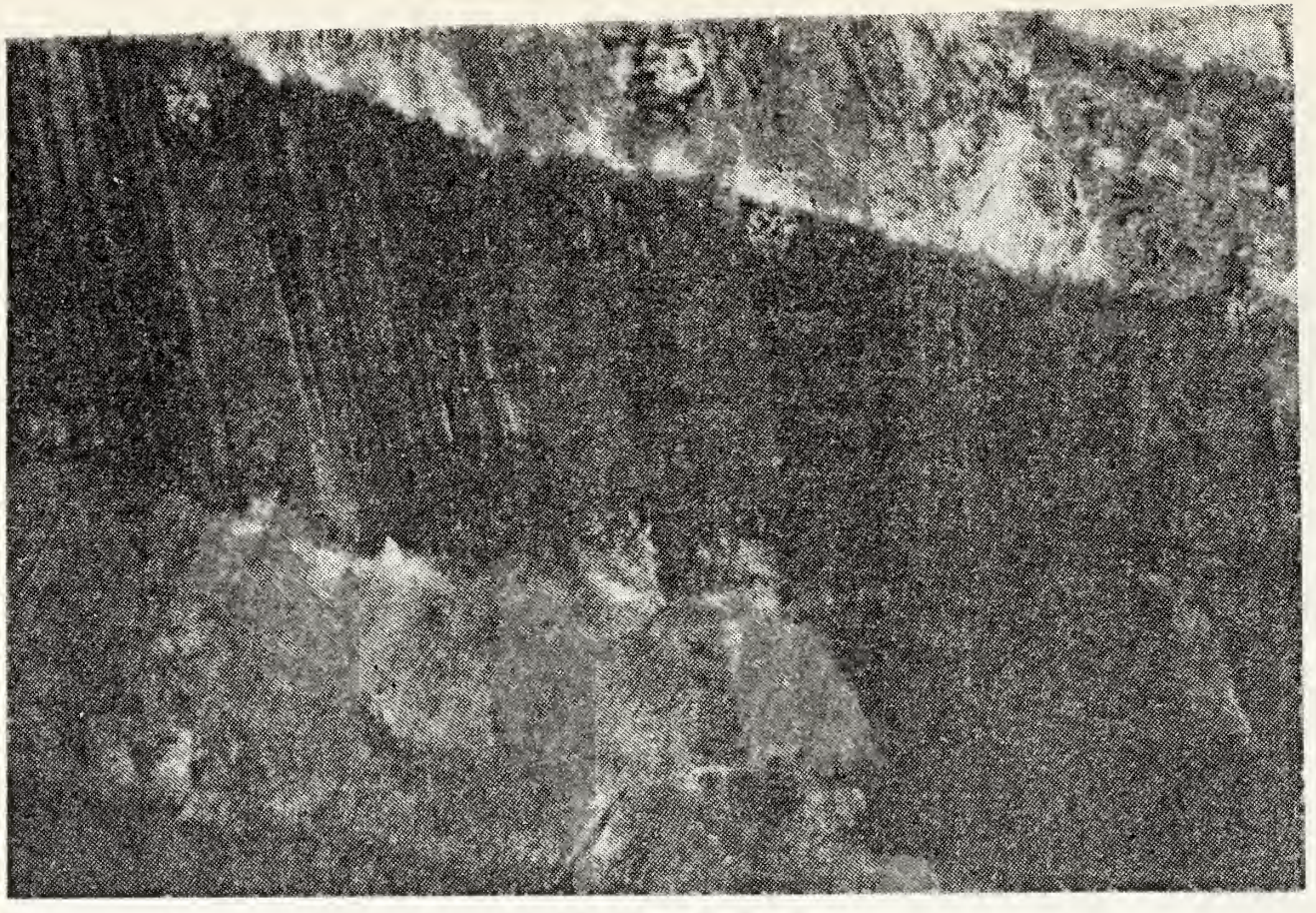

Micrograph 17a. Appearance of possible single crystals within the large, internally striated central plate of the as received alloy (4.20% cold work). (TEM, 66,000X)

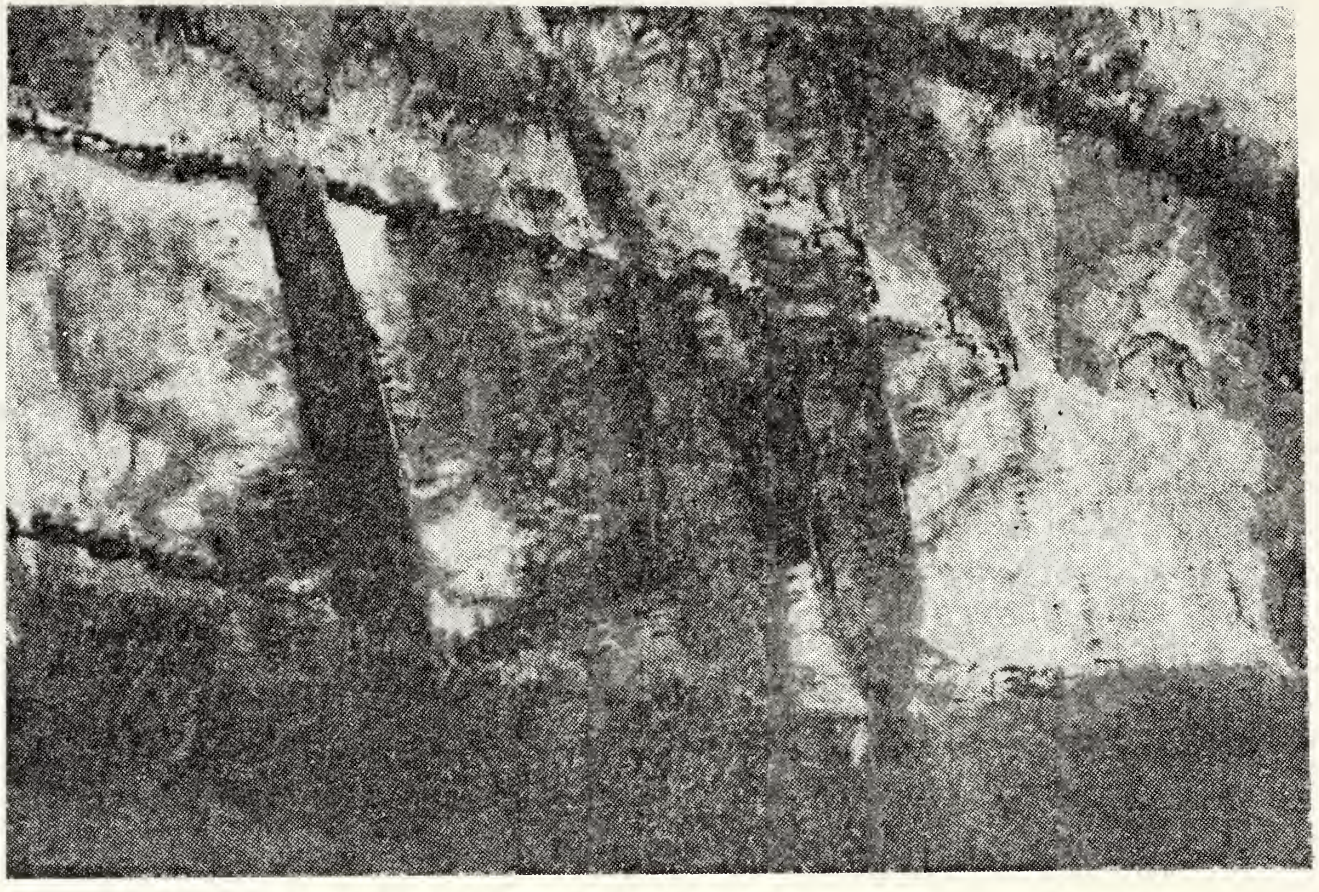

Micrograph 17b. Same specimen as Micrograph 17a at different tilt. No striations observed in prospective single crystal regions. (TEM, 66,000X)

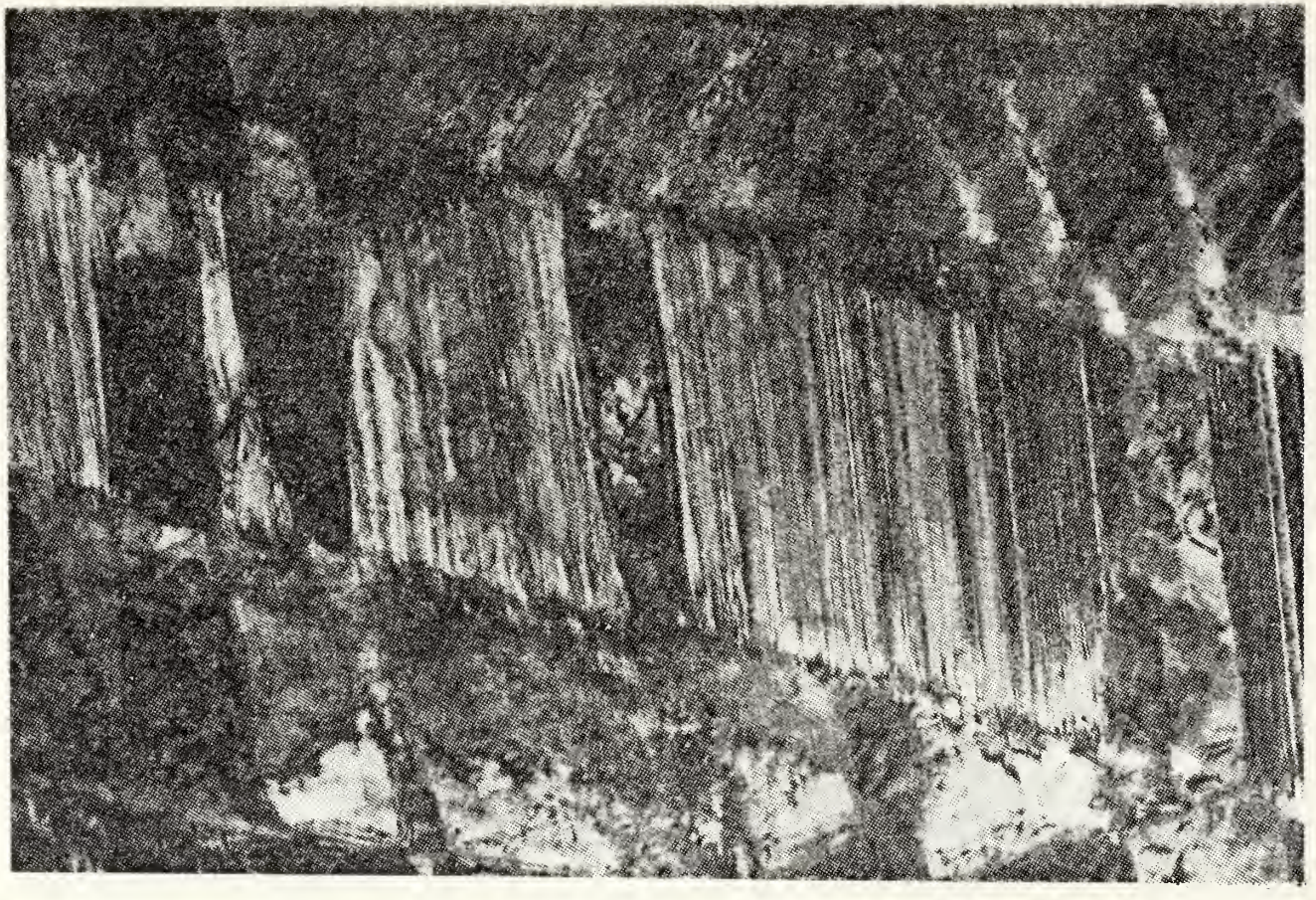

Micrograph 17c. Same specimen as Micrograph 17b at different tilt. Absence of internal striations in finger-like structures as specimen is tilted in the TEM confirms structures as single crystals. (TEM, 66,000X)

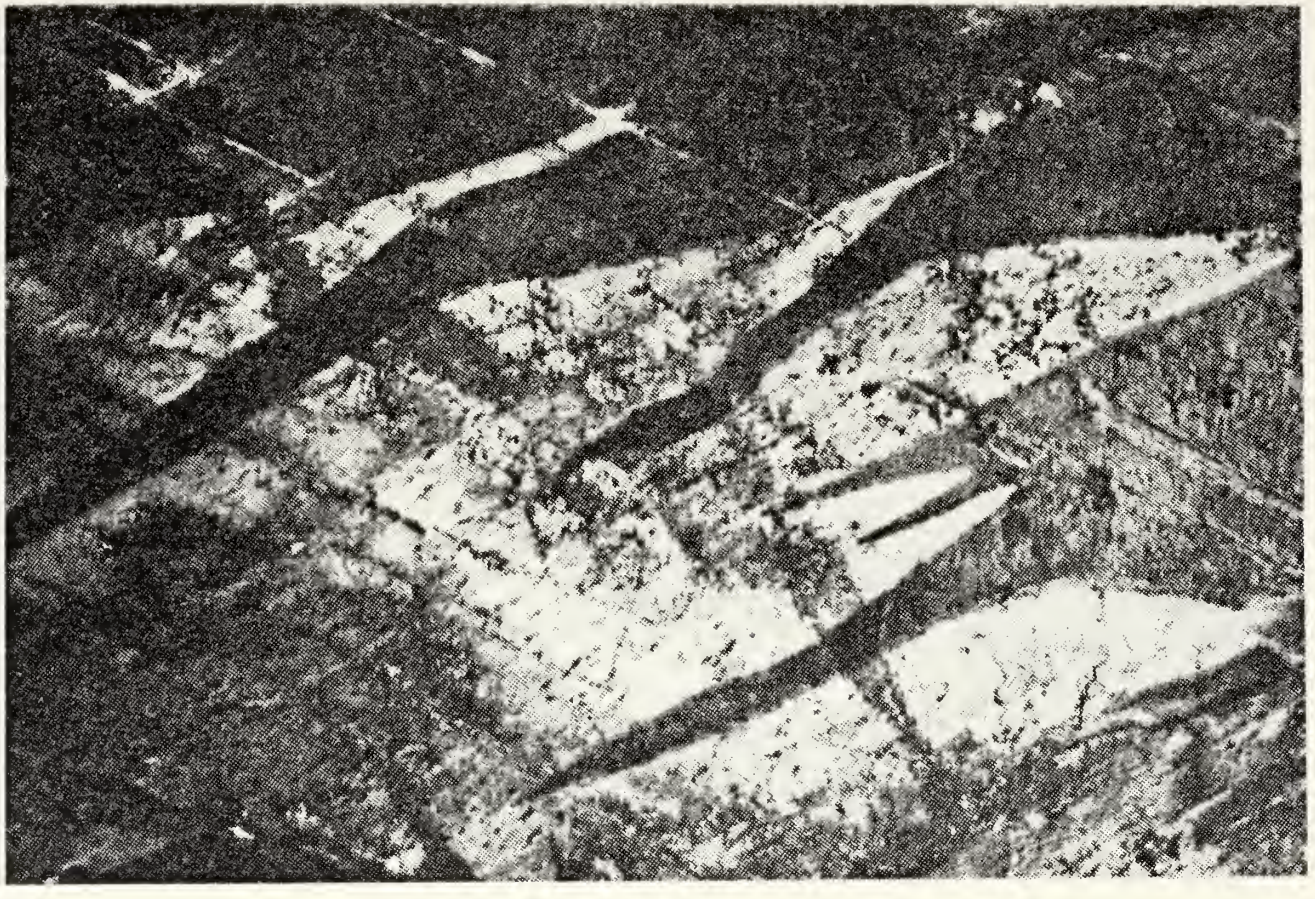

Micrograph 18. As received alloy B (12.30% cold work). White forked structures appear to have grown into the darker surrounding matrix.
(TEM, 13,200X)

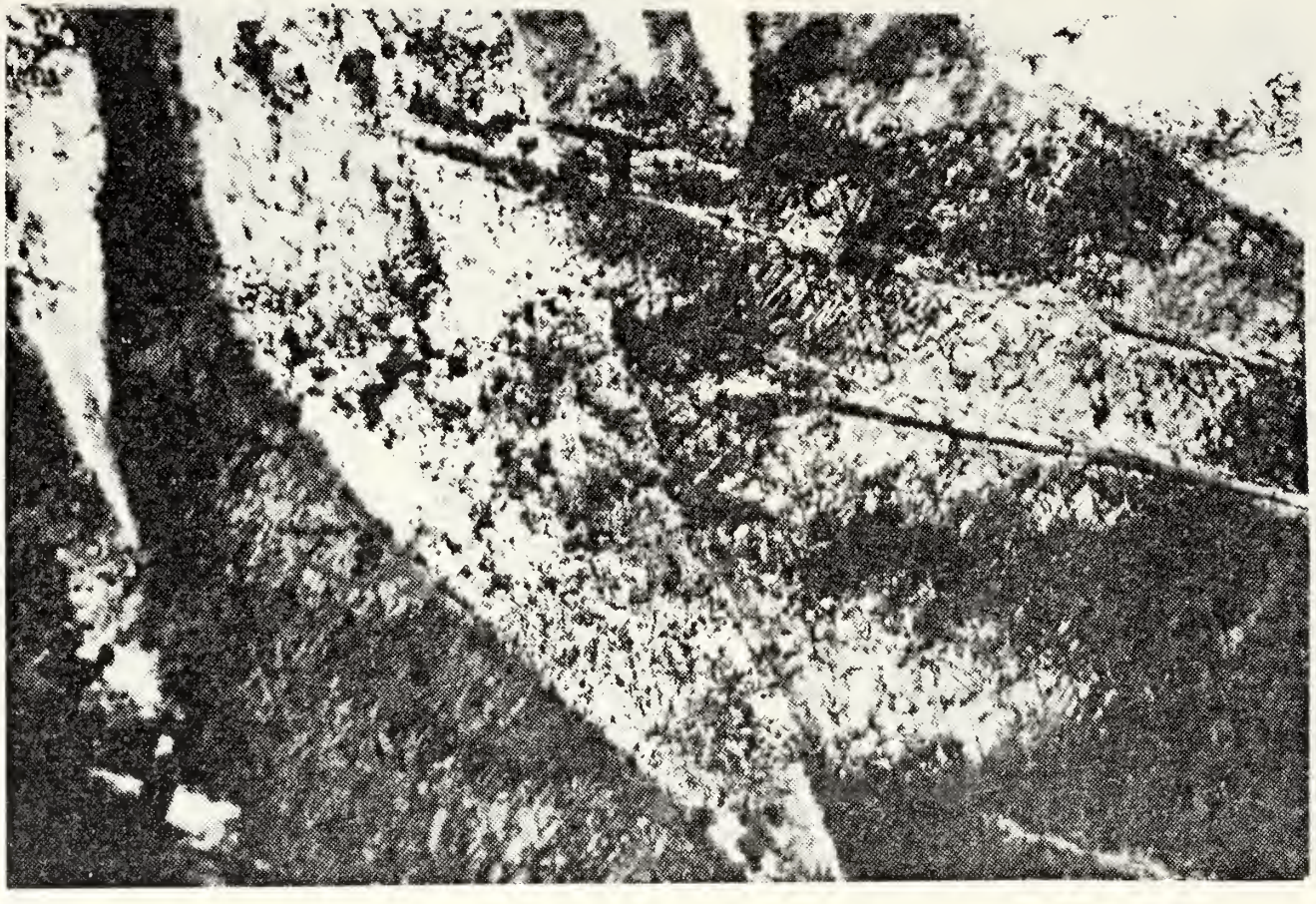

Micrograph 19. As received alloy B (12.30% cold work). High magnification showing the wavy, forked morphology of the deformed alloy. (TEM, 35,640X)

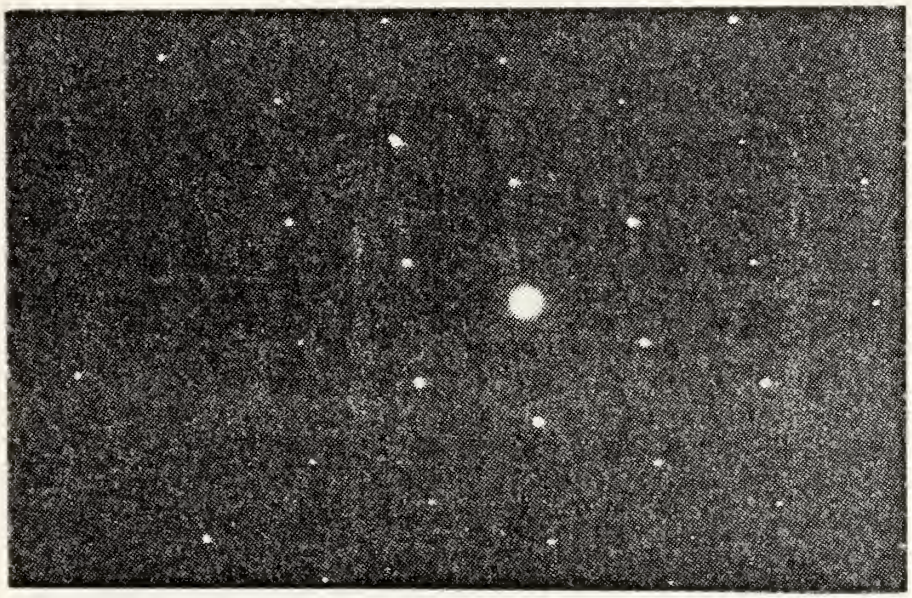

Micrograph 20a. SAD from dark matrix region (Micrograph 18). [40$\bar{1}$] 18R zone pattern.

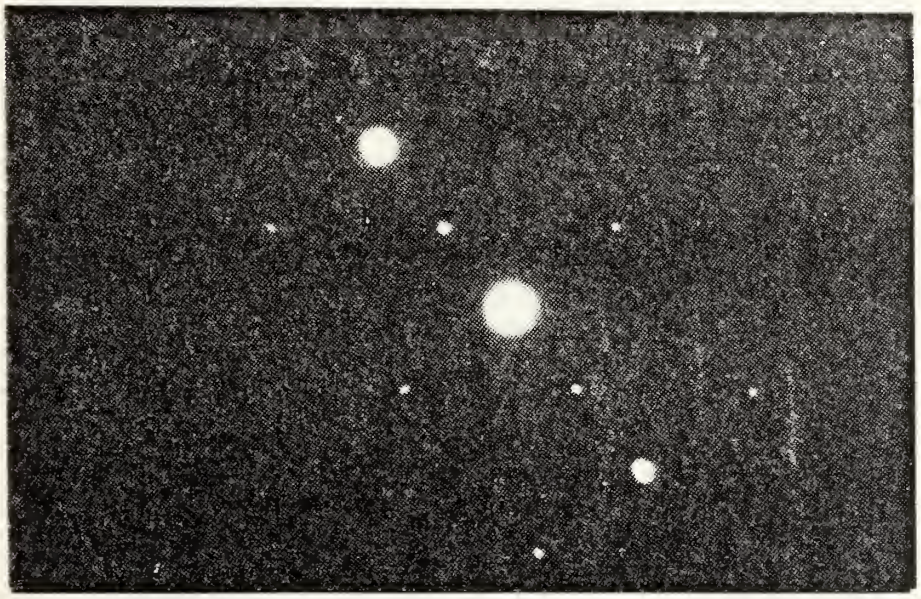

Micrograph 20b. SAD from white forked region (Micrograph 18). [10$\bar{1}$] 6R zone pattern.

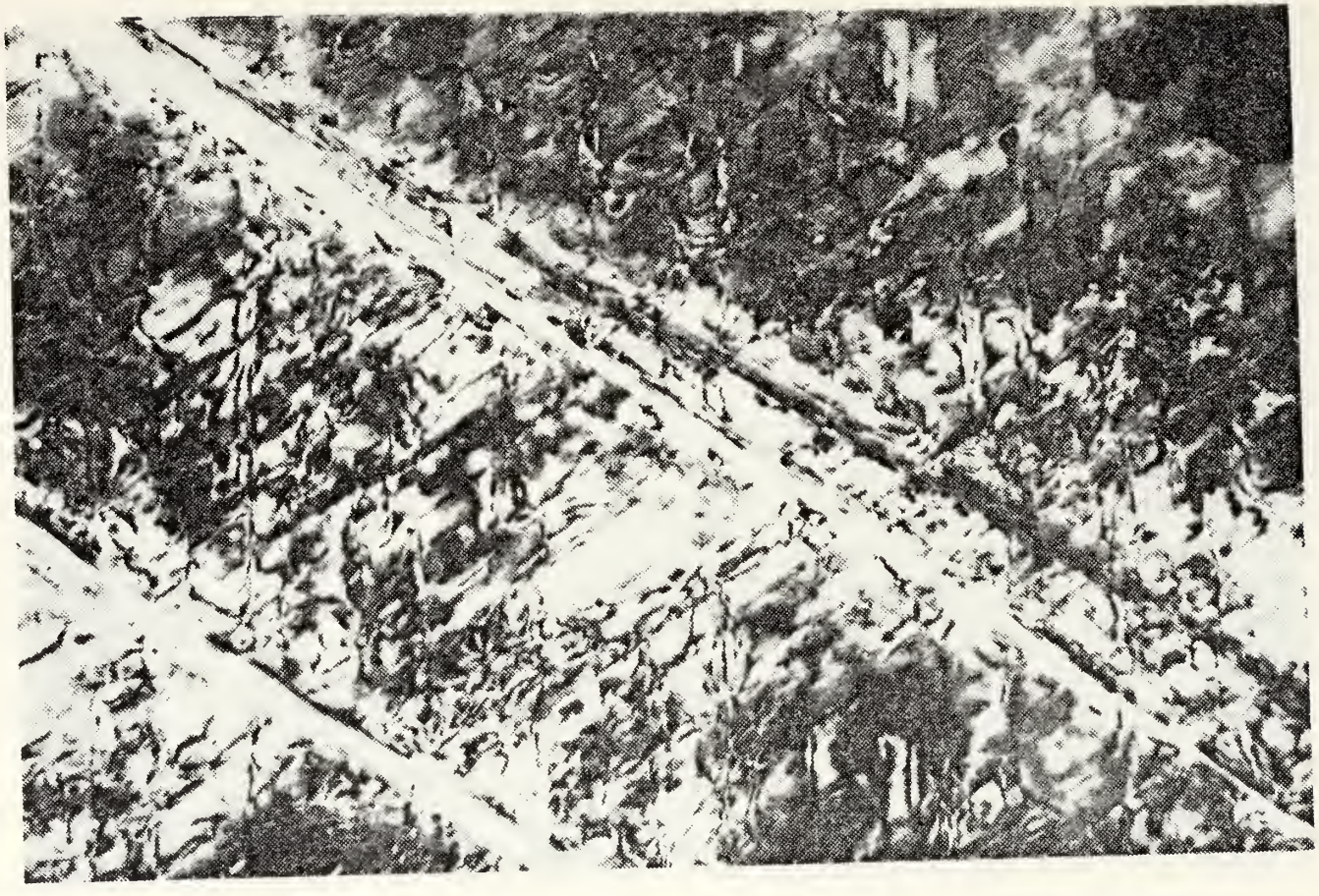

Micrograph 21. Moire patterns are evident in the heavily deformed (12.30% cold work) alloy. (TEM, 83,000X)

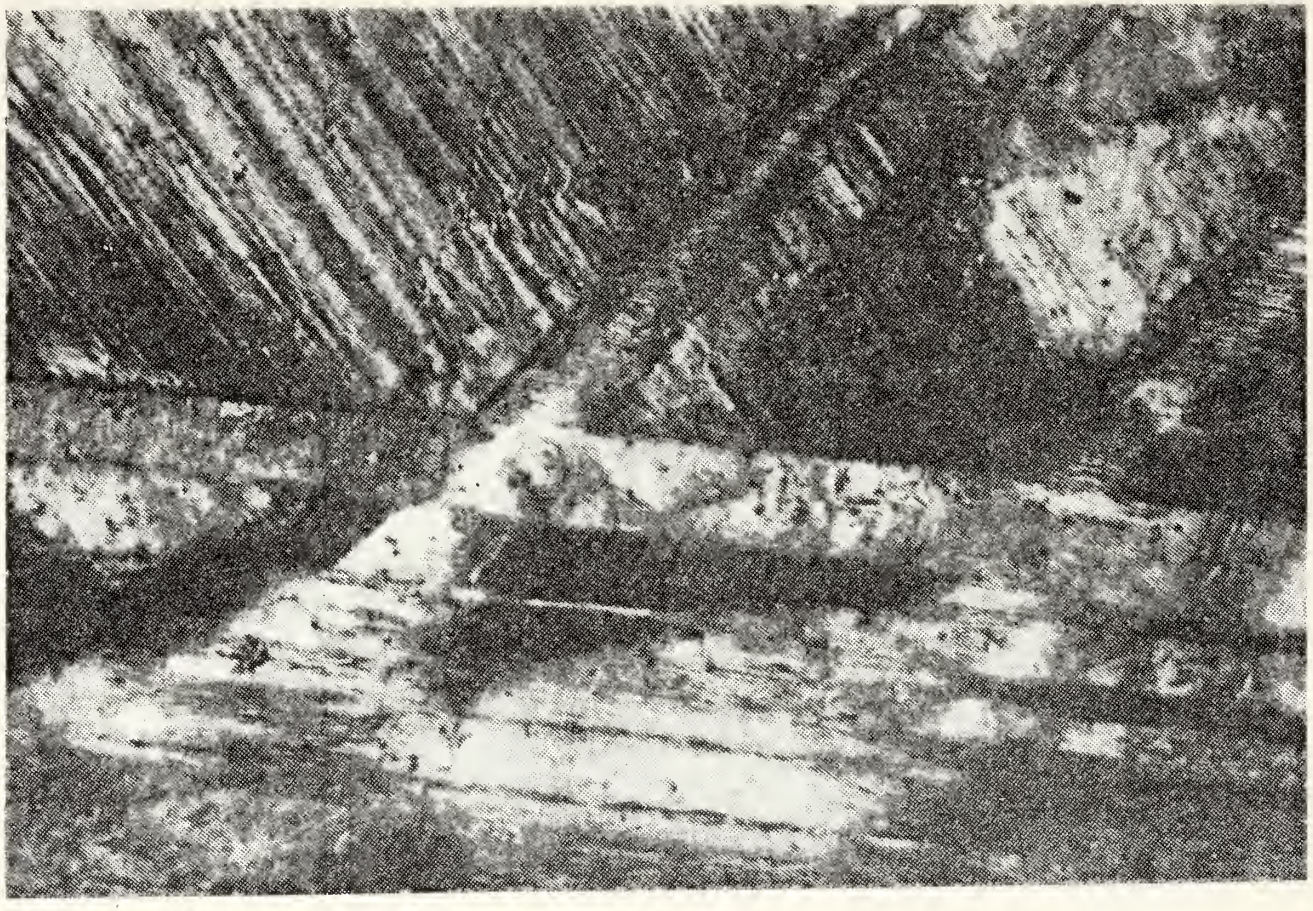

Micrograph 22. As homogenized alloy B (5 thermal cycles). Cycling has produced some variant crossings. (TEM, 35,640X)

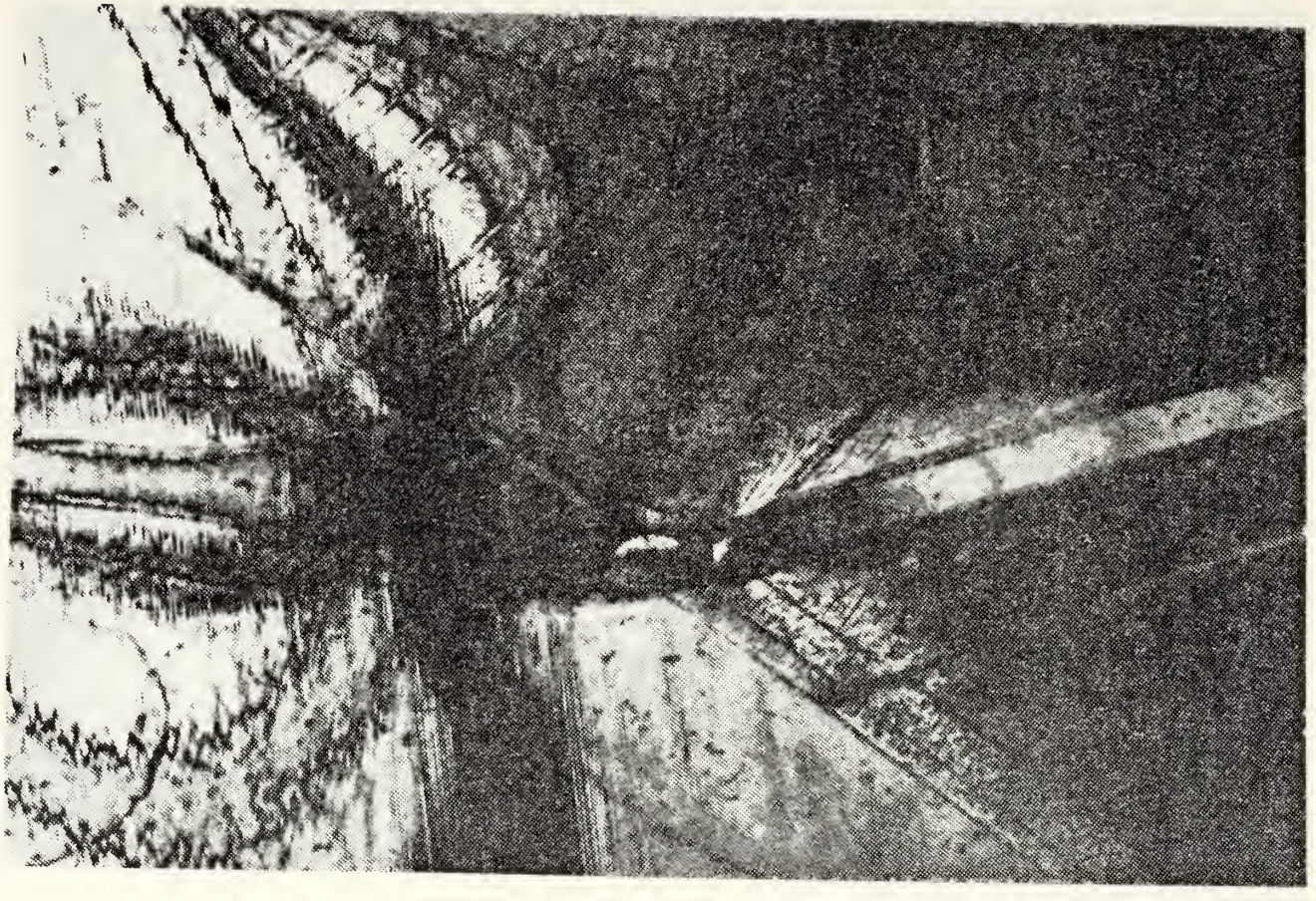

Micrograph 23. As homogenized alloy B (5 thermal cycles). Mixing and crossing of variants has introduced dislocations. (TEM, 26,400X)

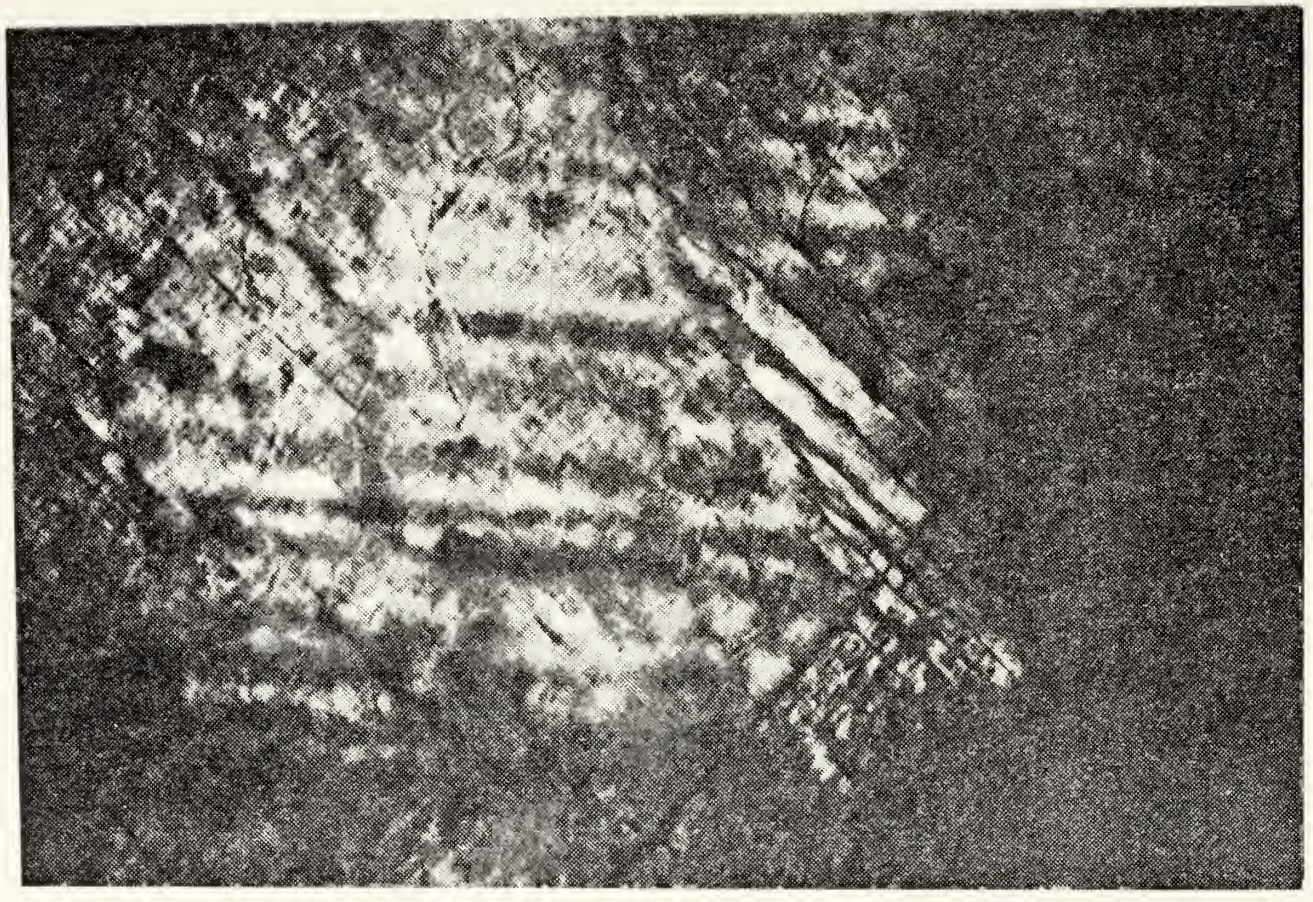

Micrograph 24. As homogenized alloy B (204 thermal cycles). The wormwood-like structures correspond to APBs. (TEM, 63,360X)

IV. DISCUSSION

The format for the interpretation and discussion of experimental results, including correlation of optical micrographs, TEM images and SADs, and calorimetry data follows: 1.) brief review and summary of the structural and substructural conditions prevailing in the as received and as homogenized alloy based, upon analysis of optical micrographs, TEM images, and TEM SADs; 2.) analysis of the effect of cold work upon as received alloy morphology, including a review of optical and TEM results characterizing the stress induced wavy morphology prevailing in the heavily deformed as received alloy; 3.) analysis of the effect of cold work upon the M $\rightarrow$ P and P $\rightarrow$ M transformation kinetics of thermally cycled shape memory alloy B, specifically, correlation of DSC third cycle endotherms and exotherms with corresponding alloy morphology; 4.) analysis of the anomalous behavior of the as received and as homogenized shape memory alloy B during the first DSC heating half cycle; and finally, 5.) speculation upon the principle factors responsible for the significant disparity between DSC profiles for the thermally cycled as received and as homogenized alloy.

1.) Examination of the as received shape memory alloy at the optical level confirmed that the alloy chosen for this

investigation (76.0 wt. % Cu, 16.5 wt. % Zn, and 7.5 wt. % Al) existed entirely as martensite at room temperature (Micrograph 1a). Optical examination of the martensitic alloy revealed well defined twin-like plates with straight regular boundaries confined within the original retained parent phase grain boundaries. The average grain size of the as received alloy was approximately 400 micrometers (Table I), although, individual grains varied greatly in size.

Most beta phase noble metal alloys (Cu-Zn-Al alloys belong to this category) are b.c.c., and the crystal structures of their transformation products are close packed layered structures transformed from a {110} b.c.c. shear plane. When shear occurs in the same direction on every plane or every alternate plane parallel to (110) the resulting structure is f.c.c. or h.c.p. respectively. When shear occurs randomly, stacking faults are introduced in either the f.c.c. or h.c.p. structure. When a product phase, inherits through transformation, the atomic ordering of its parent phase, the close packed product structures have superlattices (Fe_3Al-type (DO_3) superlattices or CsCl-type (B2) superlattice) [Ref. 24].

Analysis of SAD patterns (Micrographs 7a-7d) from representative structures/TEM foil regions of the as received and as homogenized alloy revealed diffraction conditions which are associated with 18R martensite.

Therefore, the presumption is that the as received and as homogenized alloys exist as predominently 18R martensite at room temperature, having been formed from a DO_3 ordered parent. The occurance of 2H martensite in the as received alloy (image, Micrograph 11a; SAD, Micrograph 11b) could be the result of forming (hot-rolling produced a deformation induced variant), or local inhomogeneity in composition, or possibly the so called "thin foil effect" (relaxation of constraint in the thin section).

A concise description of morphology at the microstructural level of undeformed, as received and as homogenized alloy B was presented previously under Results (Micrographs 5-11). Generally, the as received and as homogenized martensitic alloy exhibited regular, alternating, internally striated plate morphology (Micrograph 5). The existence of stacking faults and partial dislocations within the internally striated plates is confirmed by Micrographs 6 and 8.

Micrographs 8-9 are bright field images of APBs occuring in both the as received and as homogenized alloy. Alloys with DO_3-type superlattice exhibit complicated APB structures. Since the unit cell is composed of four interpenetrating f.c.c. sublattices, and its lattice parameter is twice that of the equivalent B2 structure, two different types of antiphase displacement vectors can occur: $\underline{P}_1=a/4\langle 111\rangle$ and $\underline{P}_2=a/2\langle 100\rangle$. The character of APBs is a

function of the specific alloy system. APBs due to $\underline{P}_2$ or $\underline{P}_1$ antiphase vectors may be curved randomly or may be parallel to certain crystallographic planes [Ref. 25]. B2-type APBs can be imaged using a superlattice spot associated with the $\underline{P}_1$-type antiphase vector and DO_3-type APBs can be imaged using a superlattice spot associated with the $\underline{P}_2$-type antiphase vector. Micrographs 8-9 (randomly curved APBs appearing in the as received and as homogenized alloy) are correlated with the $\underline{P}_2=a/2\langle 100\rangle$ (DO_3-type) antiphase vector. Since the APBs of the b.c.c. parent structure are transfered into APBs of the martensitic structure, a correlation may exist between the APB energy, the domain structure and the transformation mechanism. However, since the occurance, distribution, and size of APBs was the same for both the as received and as homogenized alloy B, the effect of APB energy is not a factor when accounting for the disparity between the as received and as homogenized alloys' DSC transformation profiles.

In summary, the martensite morphology of the as received and as homogenized alloys was determined to be essentially identical. However, the as homogenized alloys' average grain size is approximately twice that of the as received alloys' average grain size, and 2H martensite was found in the as received alloy.

2.) The effect of cold work upon as received alloy B morphology, at the optical level, can be appreciated by

viewing Micrographs 1a-1i in series. At low deformation (1.09% cold work), structural changes are very subtle. Plate/variant traces observed under polarized light exhibit slight curvature and intervariant boundaries appear less straight and regular than corresponding structures in the undeformed alloy. As the amount of cold work increases, the martensite plates exhibit greater deformation, and the orientation of variants becomes less organized, as if the plates have been sheared or splintered. At deformation corresponding to 12.30% cold work, wavy morphology dominates. The same structural trend is observed at the microstructural level as evidenced by TEM images and SADs (Micrographs 5-21). Micrographs 5-11b characterize the structural conditions of the as received and as homogenized alloy B, and were addressed previously. Micrographs 12-17c correspond to heavily deformed, as received alloy B (4.20% cold work), and Micrographs 18-21 show the effects of advanced deformation (12.30% cold work) upon alloy morphology.

At deformation corresponding to 4.20% cold work, dramatic morphological changes have occured in the as received alloy. The regular, planer, plate-like structures observed in the undeformed alloy (Micrographs 5,10), now exhibit internally banded substructure; the intervariant boundaries have suffered severe deformation, appearing contorted and thickened; and stress induced spear shaped,

2H martensites penetrate the originally undeformed 18R matrix (Micrograph 12). Heavy deformation has produced a large defect population within the plates as evidenced by massive dislocation tangles of random orientation appearing concentrated in the banded regions adjacent to variant boundaries (Micrographs 13-14). Further evidence of stress induced martensitic transformation is found in Micrographs 17a-17c, where stress induced single crystals have formed within existing 18R plates. Evidence of concentrated stress conditions, in the heavily deformed (4.20% cold work), as received alloy is provided by Micrograph 15, where basal slip is observed to have occured in the deformed alloy.

Micrographs 18-21 illustrate the onset of "advanced" deformation in the as received alloy. Working with Cu-Zn and Cu-Sn alloys, Wayman reported that deformation below M_f results in preferential growth of certain martensite variants including single crystal formation, and that continued deformation causes these new structures to form bands which do not easily revert to parent phase upon heating (in single crystals, 6R$\rightarrow$ 18R$\rightarrow$$DO_3$ or 3R$\rightarrow$ 9R$\rightarrow$B2 reversion occurs, but 6R or 3R variants are often "trapped" by the matrix phase and retained above A_f) [Ref. 17]. Micrographs 18-20b demonstrate that "advanced" deformation (12.30% cold work) may have resulted in 18R to 6R martensitic transformation in the as received alloy. Jagged, wavy fingers of 6R martensite are observed penetrating an 18R

matrix in Micrograph 18. Further evidence of advanced deformation and concentrated stress states is manifested in the Moire patterns shown in Micrograph 21.

3.) The correlation of DSC results characterizing the M→P and P→M transformations of selectively deformed and thermally cycled as received alloy B with associated alloy morphology as characterized by optical and TEM micrographs follows; a.) undeformed as received alloy B (Micrographs 1a, 2a-2c, 5-7a, 8, 24; Figures 2-3; Table II); b.) as received alloy B, 4.20% cold work (Micrographs 1d, 2f-2g, 12-17c; Figures 8-9; Table V); and c.) as received alloy B, 12.30% cold work (Micrographs 1g, 2h-2i, 18-21).

a.) Focusing upon third cycle DSC transformation endotherms and exotherms for the as received alloy (Figures 10-11, Table VI), only minor fluctuations in kinetic parameters for the M→P and P→M transformations were observed to occur for samples 1, 2 and 3 (as received alloy B; 0.00%, 1.09%, and 2.57% cold work). These minor excursions from baseline (undeformed, as received alloy B) kinetic parameters are consistent with optical and TEM results, in that only subtle changes in alloy morphology were observed for the modestly deformed alloy. Small fluctuations about the as received alloys' baseline parameters, for modestly deformed alloy B, may be accounted for in terms of slight increases in defect population and local variant/variant transformations.

If martensite to martensite transformations have occured in samples 1, 2 and 3; DSC evidence suggests that these new martensites, which differ in configurational energy from the 18R matrix from which they were formed, are recovered during thermal cycling and impose no significant impediment to the transformation processes.

b.) When the as received alloy was further deformed (4.20% cold work), dramatic changes were observed in both alloy morphology and transformation kinetics. Comparison of third cycle DSC transformation endotherms and associated kinetic parameters for samples 1-4 (Figure 10, Table V) indicate: 1.) that the M $\rightarrow$ P transformation started at approximately the same temperature (A_s) for all samples; 2.) that the temperature at which the maximum transformation rate occured (A_{max}) remained constant as deformation increased but that the rate of transformation at A_{max} was significantly slower for the 4.20% cold worked alloy; 3.) that the transformation from product to parent phase for sample 4 required additional thermal energy for completion (higher A_f); and 4.) that a significant proportion of the as received alloy (4.20% cold work) was retained as martensite during the third heating half cycle.

As discussed previously, the morphology of the heavily deformed alloy (4.20% cold work) is very complicated (Micrographs 12-17c). It is likely that the structural and substructural environment in the heavily deformed alloy as

manifested by stress induced, wavy morphology (contorted intervariant boundaries, banded substructure, herringbone patterns of 2H martensite, massive dislocation tangles, concentrated stress fields as evidenced by basal slip, and single crystal formation) acts synergistically to stablize martensite variants and impede the thermoelastic transformation from product to parent.

The sample 4, as received alloy (4.20% cold work) P $\longrightarrow$ M third cycle reversion transformation (Figure 11, Table V) is consistent in character with its associated M $\longrightarrow$ P transformation, in that at deformation corresponding to 4.20% cold work the P $\longrightarrow$ M transformation kinetics differ radically from those of the undeformed and modestly deformed (1.09% and 2.57% cold work) as received alloy. M_s, M_f, and M_{max} were shifted toward lower temperatures, the rate of transformation at M_{max} was severly depressed, and the amount of parent phase transforming to product was significantly smaller for the 4.20% cold worked alloy.

4.) As reported previously in the section addressing DSC results, for all samples tested, endotherm 1, corresponding to the first heating half cycle, was displaced significantly toward higher temperatures relative to endotherms 2 and 3 (Figures 2,4,6,8,12,14). The rate of transformation during the first heating half cycle was slower and the temperature range over which the transformation process occured was larger.

A possible explanation of this peculiar transformation behavior is that during the first heating half cycle burst-type martensite is reverted to parent phase and upon subsequent cooling, thermoelastic martensite is produced predominently by the continuous growth mode. Therefore, the disparity between endotherms could reflect differences in energy barriers for reversion of continuously grown and burst-type martensite. Micrographs 3a-3d correspond to the as homogenized alloy after successive thermal cycles. The splintered morphology observed after the first thermal cycle (Micrograph 3b), supports the interpretation of DSC data in that significant structural changes (splintering, growth, disappearance, and reorganization of variants) have occured during the first complete thermal cycle, and that subsequent thermal cycling has had a less dramatic effect upon overall structure. Micrographs 4a-4b correspond to the as homogenized alloy after five and forty termal cycles. The new variant introduced into the alloy structure after five cycles (Micrograph 4a), may be the result of either thermally/stress induced martensite to martensite transformation. Micrographs 22-23 demonstrate that thermal cycling can result in variant crossings and that the crossing of variants have introduced lattice defects (dislocations). Micrograph 24 corresponds to the as received alloy after five thermal cycles. The size and distribution of APBs in the cycled alloy is the same as in the uncycled alloy (Micrograph 9).

5.) The following factors were considered in interpreting the disparity between as received and as homogenized alloy B third cycle endotherms and exotherms (Figures 16-17, Table IX): a.) vacancy concentration, b.) degree of ordering in parent and consequently product phases, c.) grain size, d.) alloy morphology, and e.) defect (dislocation) concentration and distribution.

At the microstructural level, the morphology of the as received and as homogenized alloy was basically the same (Micrographs 5-11), both alloys exist predominently as 18R martensite at room temperature. Comparing the size and distribution of APBs observed in both alloys, suggests that the degree of ordering in each DO_3 parent phase was the same. Also, any initial difference in vacancy concentration between the as received and as homogenized alloy should have disappeared after the first thermal cycle. Consequently, any plausible explanation of calorimetry results must be made in terms of grain size and dislocation concentrations. The average grain size of the as homogenized alloy is approximately twice that of the as received alloy (Table I).

It is also reasonable to speculate that the homogenization process both reduced the magnitude of the stress fields surrounding dislocations in the as received alloy by allowing these dislocations to assume less energetic configurations and reduced the overall defect population in the alloy. Therefore, the as homogenized alloy suffered a compositional

defect loss relative to the as received alloy, in that fewer defects were dispersed across larger grains. If this were the case, it could be predicted that the diminuation of nucleation sites in the as homogenized alloy would retard the transformation process from parent to product phase. This would explain the difference in third cycle DSC profiles between the as received and as homogenized alloy.

V. CONCLUSIONS

1.) The effect of cold work upon 18R martensitic Cu-Zn-Al shape memory alloy B is manifested by discrete changes in alloy morphology and product to parent and parent to product phase transformation behavior.

2.) Three deformation regimes can be identified for the cold worked alloy: Modest; less than approximately 4% cold work; heavy, approximately 4-6% cold work; and advanced, greater than 7% cold work.

3.) Modest deformations produce only small changes in alloy morphology and minor fluctuations about baseline, undeformed alloy, transformation parameters.

4.) Heavy deformation of the Cu-Zn-Al shape memory alloy results in dramatic morphological changes whose synergistic effect is to impede thermal martensitic transformation and reversion.

5.) Advanced deformation is characterized by predominently "wavy" morphology, high alloy stress states, and stress induced martensite to martensite transformations. The onset of advanced deformation corresponds to a threshold stress state/structural environment where transformations can no longer be induced through moderate (280 K - 430 K) thermal cycling.

6.) There is no significant microstructural difference between the as received and as homogenized alloys,

therefore, disparities in the transformation kinetics between these alloys are likely the result of a compositional defect loss produced by the homogenization process.

7.) A plausible explanation of anomalous alloy behavior during the first DSC heating half cycle can be cauched in terms of the energetics of burst-type/continuous growth-type martensite.

APPENDIX

Perkin-Elmer (DSC-2) Differential Scanning Calorimeter Machine Parameters

	DSC
delta T balance	331
Slope onset	260
Temperature calibration	
1.) Zero	030
2.) Range	890
Zero	030
Slope	691
Range	0.5 mcal/sec
Heating rate	10 K/min
Cooling rate	10 K/min
Lower limit	280 K
Upper limit	430 K

	CHART RECORDER
Chart speed	20
Range	20

LIST OF REFERENCES

1. Kelly, E. W., Effects of Thermomechanical Processing on Damping Characteristics of Martensitic Cu - 13.5 w/o Al Alloy, Master's Thesis, Naval Postgraduate School, 1977.

2. Wayman, C. M., J. Met., v. 9, pp. 129-137, 1980.

3. Chang, L. C. and Read, T. A., "Plastic Deformation and Diffusionless Phase Changes in Metals - The GoldCadmium Beta Phase," Trans. AIME, v. 191, p. 47, 1951.

4. Beuhler, W. J., Gilfrich, J. V. and Wiley, R. C., "Effect of Low-Temperature Phase Changes of Mechanical Properties of Alloys near Composition TiNi," J. Appl. Phys., v. 34, p. 1475, 1963.

5. Wayman, C. M., "On Memory Effects Related to Martensitic Transformations and Observations in B - Brass and Fe_3Pt," Scripta Met., v. 5, p. 489, 1971.

6. Shimizu, K., Okumura, Y. and Kubo, H., "Crystallographic and Morphological Studies on the FCC to FCT Transformation in Mn-Cu Alloys," Trans. Japan Inst. Met., v. 23, No. 2, pp. 53-59, 1982.

7. Basinski, Z. S. and Christian, J. W., "Crystallography of Deformation by Twin Boundry Movements in In-Tl Alloys," Acta Met., v. 2, p. 101, 1953.

8. Pops, H., "Stress Induced Pseudoelasticity in Ternary Cu-Zn based Beta Prime Alloys," Met. Trans., v. 1, p. 251, 1970.

9. Eisenwasser, J. D. and Brown, L. C., "Pseudoelasticity and Strain Memory Effect in Cu-Zn-Sn Alloys," Met. Trans., v. 3, p. 1359, 1972.

10. Otsuka, K. and Shimizu, S., "Memory Effects and Thermoelastic Martensite Transformation in Cu-Al-Ni Alloys," Scripta Met., v. 4, p. 169, 1970.

11. Perkins, J. and Meusing, W. E., "Martensitic Transformation Cycling in Cu-Zn-Al Shape Memory Alloys," Met. Trans., v. 14A, pp. 33-36, 1983.

12. Perkins, J., "Shape Memory Behavior and Thermoelastic Martensitic Transformations," Mat. Sci. and Eng., v. 51, pp. 181-192, 1981.

13. Schroeder, T. A., Cornelis, I. and Wayman, C. M., "The Shape Memory Effect and Pseudoelasticity in Polycrystalline Cu-Zn Alloys," Met. Trans., v. 7A, pp. 535-553, 1976.

14. Perkins, J., "Lattice Transformations Related to Unique Mechanical Effects," Met. Trans., v. 4, pp. 2709-2721, 1973.

15. Wayman, C. M. and Shimizu, K., "The Shape Memory ('Marmem') Effect in Alloys," Met. Sci. J., v. 6, pp. 175-183, 1972.

16. Cohen, M. and Wayman, C. M., "Fundamentals of Martensitic Reactions," reprint: Met. Treat., pp. 445-446, 1980.

17. Wayman, C. M. and Cornelis, I., "Deformation Behavior of Cu-Zn Martensites," Scripta Met., v. 9, pp. 437-438, 1975.

18. Schroeder, T. A. and Wayman, C. M., "Martensite to Martensite Transformations in Deformed Cu-Zn Monocrystals," Scripta Met., v. 10, pp. 241-246, 1976.

19. Schroeder, T. A., and Wayman, C. M., "Martensite to Martensite Transformations in Cu-Zn Alloys," Acta Met., v. 26, pp. 1745-1757, 1978.

20. Delay, L., Van Humbeeck, J. and Deruytters, A., "Shape Memory Effect and Internal Damping in Copper-Aluminum and Copper-Zinc based Alloys," INCRA Project No. 238, Semi-annual Report, 1976.

21. Guy, A. G., Elements of Physical Metallurgy, p. 432, Addison-Wesley Publishing Company, 1960.

22. Thompson, H., Microscopic Techniques in Metallurgy, pp. 78-105, Sir Issac Pitman & Sons, 1954.

23. Perkin Elmer Corporation, Model DSC-2 Differiential Scanning Calorimeter, pp. 2-1 - 2-6, Perkin Elmer Corporation, 1978.

24. Nishsyama, Z., Martensite Transformation, Academic Press, 1978.

25. Warlimont, H. and Delaey, L., "Martensitic Transformation in Copper-Silver-and Gold-Based Alloys," Progress in Materials Science, v. 18, 1974.

BIBLIOGRAPHY

Cornelis, I. and Wayman, C. M., "Phase Transformations in Metastable Beta Prime CuZn Alloys - I. Martensitic Transformations," Acta Met., v. 22, 1974.

Dvorak, J. R. and Rostoker, W., Interpretation of Metallographic Structures, Academic Press, 1965.

Graves, R. H. and Wrighton, H., Practical Microscopical Metallography, 4th ed., Chapman & Hall, Ltd., 1967.

Schroeder, T. A. and Wayman, C. M., "The Two-Way Shape Memory Effect and Other Training Phenomenea in Cu-Zn Single Crystals," Scripta Met., v. 11, pp. 225-230, 1977.

Schroeder, T. A. and Wayman, C. M., "The Formation of Martensite and the Mechanism of the Shape Memory Effect in Single Crystals," Acta Met., v. 25, pp. 1375-1391, 1976.

Schroeder, T. A. and Wayman, C. M., "Pseudoelastic Effects in Cu-Zn Single Crystals," Acta Met., v. 27, pp. 405-417, 1978.

Shewman, P. G., Transformations in Metals, McGraw-Hill Book Company, 1969.

Weinberg, F., Tools and Techniques in Physical Metallurgy, V. 1, Dekker, Inc., 1970.

INITIAL DISTRIBUTION LIST

		No. Copies
1.	Defense Technical Information Center Cameron Station Alexandria, Virginia 22314	2
2.	Library, Code 0142 Naval Postgraduate School Monterey, California 93943	2
3.	Department Chairman, Code 69 Department of Mechanical Engineering Naval Postgraduate School Monterey, California 93943	1
4.	Associate Professor Jeff Perkins, Code 69Ps Department of Mechanical Engineering Naval Postgraduate School Monterey, California 93943	5
5.	Lt Stephen M. Sullivan 406 Broadview Avenue Altamonte Springs, Florida 32701	1

Thesis
S8616 Sullivan
c.1 The effect of cold
work on martensitic
transformation in Cu-Zn-
Al Shape memory alloys.